UNIVERSITAT POLITÈCNICA DE CATALUNYA

DOCTORAL THESIS

Ship propeller induced scour of non-cohesive sediment in low bed-clearance conditions

---

Author:
Toni Llull Marroig

Supervisors:
Dr. F. Xavier Gironella i Cobos
Dr. Anna Mujal i Colilles

A thesis submitted in fulfillment of the requirements
for the degree of Doctor of Philosophy

in the

Laboratori d'Enginyeria Marítima
Departament de Ciència i Enginyeria Nàutiques
Departament d'Enginyeria Civil i Ambiental

October 17, 2021

Declaration of Authorship

I, Toni Llull Marroig, declare that this thesis titled, "Ship propeller induced scour of non-cohesive sediment in low bed-clearance conditions" and the work presented in it are my own. I confirm that:

- This work was done wholly or mainly while in candidature for a research degree at this University.
- Where any part of this thesis has previously been submitted for a degree or any other qualification at this University or any other institution, this has been clearly stated.
- Where I have consulted the published work of others, this is always clearly attributed.
- Where I have quoted from the work of others, the source is always given. With the exception of such quotations, this thesis is entirely my own work.
- I have acknowledged all main sources of help.
- Where the thesis is based on work done by myself jointly with others, I have made clear exactly what was done by others and what I have contributed myself.

Abstract

Ships maneuvering in low bed clearance conditions induce sediment scour due to the high speed jet generated by a rotating propeller. Sediment scour is known to cause instability to quay structures, damage to the bed protection and may create huge accretion areas reaching extremely low depths, preventing the free passage of large ships. This on-going problem is linked to the constant increase in commercial ship sizes and is widely recognized in current harbor management guidelines.

This thesis presents in the first place the experimental work carried out to study the effects of two common propeller systems over the sediment bed: single and twin propellers. Next, the analysis of a case study is used to evaluate the impact of ship maneuvers over the seabed in a particular harbor basin.

The first part of the thesis presents a set of experiments in propeller jet velocity and bed shear stresses. By measurements performed in a point-by-point grid, with a Pitot-static tube coupled to differential pressure sensors, the axial velocity distribution at the so-called *efflux plane* is characterized. After that, direct measurements of bed shear stress are performed at several speeds of rotation and two bed-clearance distances with a shear plate. Velocity and bed shear stress measurements are related by an empirical friction coefficient, which is dependent on the bed clearance. A new empirical model is presented to estimate the mean shear stress in case of unconfined ship propeller jets in low bed clearance conditions.

The second part of this work shows the results of a new set of experiments in local scour due to confined twin propeller jets. The maximum scour depth is studied as a function of the bed clearance, the wall clearance and the efflux velocity of the jet. Aiming to reproduce more realistic maneuvers, scour due to forward and backward rotation of the propellers is analyzed, showing a different behavior compared to the traditional experiments with only forward rotation. The obtained results are compared to the existing formulae and later used to propose two different empirical models, one for each regime of rotation. A new non-dimensional parameter obtained from the Buckingham π analysis, proposed as Wall Froude number, is used to find a threshold triggering the scouring mechanism. The experimental results show that the distance to the vertical wall is the main contributor to the higher scour depths rather than the bed clearance.

The last part of the thesis presents a case study that is used to relate the maneuvers of the ship with the scour observed in an inner basin of the port. The study ship characteristics are obtained from the port statistics. The morphological evolution of the seabed is analyzed through hydrographic surveys of the last decade, which allows characterizing the erosion pattern. Through AIS data, the maneuver of the study ship is analyzed and used as an input maneuver in a simulator. The maneuver is reproduced to obtain the behavior of the main engines and bow thrusters. The maneuvering pattern and the behavior of the engines are used to assess the most damaging maneuvering sections, which turns out to be the ship's lateral approach to the berth, during the arrival maneuver, and the early stages of the departure maneuver.

Resum

Els vaixells que maniobren en condicions de calat reduït poden provocar erosió local del llit de sediments a causa del raig d'aigua d'alta velocitat generat per les hèlix. L'erosió causa inestabilitat en les estructures dels molls, danys a la protecció del llit i pot crear grans àrees d'acreció, posant en risc la seguretat en la navegació. Aquest fenòmen està relacionat en gran mesura amb l'augment de les dimensions dels vaixells comercials en les darreres dècades i és àmpliament reconegut en les guies actuals de gestió portuària.

Aquesta tesi presenta, en primer lloc, el treball experimental realitzat per estudiar els efectes erosius provocats per dos dels sistemes de propulsió més comuns: hèlix convencional i sistema de doble hèlix. A continuació, s'utilitza l'anàlisi d'un cas pràctic per avaluar l'impacte de les maniobres dels vaixells sobre el fons marí en una dàrsena portuària concreta.

A la primera part de la tesi es presenten i s'analitzen un conjunt de mesures experimentals de velocitat del flux d'aigua a la sortida de l'hèlix i de tensions de tall sobre un llit horitzontal. La distribució de velocitats axials es caracteritza a partir de mesures puntuals preses amb un sistema de tub de Pitot-estàtic acoblat a sensors de pressió diferencial. Posteriorment es realitzen mesures directes de les tensions de tall al llit amb una placa de tensions (*shear plate*) a tres velocitats de rotació de l'hèlix i dues distàncies verticals sobre el llit. Les mesures de la velocitat i la tensió de tall es relacionen amb un coeficient de fricció empíric que és dependent de la distància al llit.

A la segona part d'aquest treball es presenta un nou conjunt d'experiments en erosió local per sistemes de doble hèlix confinats. La profunditat màxima d'erosió s'estudia en funció de la distància al sòl, la distància a la paret i la velocitat de sortida del raig d'aigua. Amb l'objectiu de reproduir maniobres de vaixells en entorns portuaris, s'analitza l'erosió generada pels sistemes de doble hèlix en règim combinat, és a dir, avant i invertit. Els resultats mostren diferències respecte els experiments tradicionals en què només es considera la rotació avant. Per estimar l'evolució temporal de la màxima profunditat d'erosió es proposen dos models empírics, un per a cada règim de rotació. De l'anàlisi de π de Buckingham s'obté un nou paràmetre adimensional que, proposat com a nombre de Froude del mur, permet establir un llindar d'erosió. Els resultats experimentals també mostren que la distància al mur

vertical està més relacionada amb les majors profunditats d'erosió que amb la distancia al sòl.

La darrera part de la tesi presenta un cas d'estudi en què les maniobres del vaixell es relacionen amb els canvis en la morfologia portuària observada al llarg del temps. El vaixell d'estudi s'obté a partir de les estadístiques d'ús de les dàrsenes portuàries. L'evolució morfològica del fons marí s'analitza mitjançant estudis hidrogràfics de la darrera dècada, que permet caracteritzar el patró d'erosió. A través de dades AIS, s'analitza la maniobra del vaixell d'estudi i s'utilitza com a model de maniobra en un simulador. La maniobra es reprodueix al simulador, d'on se n'extreu el comportament dels motors principals i de les hèlix de maniobra. El patró de maniobra i el comportament dels motors s'utilitzen per avaluar les seccions de maniobra més perjudicials, que resulten ser l'aproximació lateral del vaixell al moll d'atrac, durant la maniobra d'arribada, i les primeres etapes de la maniobra de sortida.

Contents

Acknowledgements

The work presented in this thesis has been carried out during the last three years in three different research groups. For this reason, several professors, colleagues and friends left their footprint on it.

First of all, I want to thank my supervisors, Anna and Xavi, for the work and guidance they provided. At any time, they were ready to propose new ideas, debate and correct the work I was doing.

I also want to thank the rest of the colleagues and professors who collaborated in the different parts of this research. All the colleagues and professors with whom I worked in the Maritime Engineering Laboratory of the UPC, the Department of Nautical Sciences and Engineering of the FNB, and the Hydraulic Engineering and Fluvial Morphology research group of the LWI, contributed to concluding this work. I want to especially thank Dr. Marcel·la Castells and Dr. Francisco Nuñez for their good guidance. Even though they weren't my thesis supervisors, they have always been available to discuss any part of the work I was doing, providing good feedback and recommendations.

I want to thank those who contributed to individual parts of the thesis presented here: Dr. Jordi Fonollosa, for the work he carried out on the set-up of the AIS data acquisition system installed at the FNB; Capt. Jordi Moncunill, for the time he spent with the students in the simulator; the LIM technical staff, Quim Sospedra, Ricardo Torres and Òscar Galego, for the work they did before and during the experiments presented in this thesis; and the LWI research and technical team, Dipl-Ing. Stephan Niewerth, Dipl.-Ing. Uwe Ecklebe, Holger Kroker and Christian David, for their contribution to the work carried out during my time in Braunschweig and afterwards.

Also, I want to mention here all those friends and good people I met while working on this thesis. Thanks to those who were with me during the months I spent in Braunschweig and a special thank you to my LIM office mates, who have become unforgettable friends.

Finally, I want to thank my friends from Catalunya and Mallorca, my partner Laura and my family for the support they gave me in the past and during the time I

dedicated to this work. I am grateful to all of you.

Preface

The research reported in this dissertation was carried out at different universities and in collaboration with three different research groups:

Firstly, the work presented in Chapter 2 was developed at the Leichtweiß - Institut für Wasserbau (LWI), at the TU-Braunschweig (Germany) in two time periods. The first, during the stage carried out in the frame of the Ph.D. program, between June 2019 and December 2019. Later, and as a continuation of the work performed during the stage, new experimental work was performed. Data from both periods are included in this dissertation. All the experiments referred in Chapter 2 were part of two different Master Thesis (Dömer, 2019; Lempa, 2020). Both of the thesis were planned to obtain sets of experimental data on propeller induced velocity and shear stress to be used in this dissertation. The conceptualization of the experiments was performed by Dr. Francisco Nuñez-González and myself. The experimental set-up was prepared by Dr. Francisco Nuñez-González, Dipl-Ing. Stephan Niewerth, the technical staff in the LWI: Dipl.-Ing. Uwe Ecklebe, Holger Kroker and Christian David, and myself between June 2019 and December 2019, and later as a continuation of the work performed. The authors of the two Master Thesis, MSc. Tanita Dömer and MSc. Sebastian Lempa, performed the measurements at the laboratory as part of the objectives of the Master Thesis program. The experimental data were collected, treated and analyzed together in the present work.

Secondly, the research presented in Chapter 3 was performed as a continuation of previous work in local scour at physical model performed at the Laboratori d'Enginyeria Marítima (LIM). The conceptualization of the experiments was performed Dr. Anna Mujal i Colilles, Dr. Xavier Gironella i Cobos and myself. The experimental work was performed by myself, with great support of the technical staff at LIM: Ricardo Torres, Oscar Galego and Joaquim Sospedra. All the experiments have been analyzed by myself under the supervision of the thesis directors.

Finally, the research presented in Chapter 4 was designed by myself, in collaboration with the Dept. of Nautical Sciences and Engineering, at the Barcelona School of Nautical Studies. Dr. Marcel·la Castells i Sanabra and Capt. Jordi Moncunill provided advice in the maneuver analysis and the design of the maneuver at the simulator. The simulator maneuvers included in this Chapter were performed by supervised undergraduate students (Sebastià Amengual and Guillem Roma) in the

frame of two different Bachelor's Thesis (Amengual, 2019; Valls, 2021). The authors were under the supervision of Capt. Jordi Moncunill, Ph.D. Marcel·la Castells and myself.

List of Publications

This section summarizes the conference proceedings and journal articles published during the realization of the present dissertation:

Journal Articles:

Llull, T., Mujal-Colilles, A., & Gironella, X. (2021). Twin propeller time-dependent scouring processes. Physical experiments. *Ocean Engineering*, 236, 109461.

Llull, T., Mujal-Colilles, A., & Gironella, X. (2020). Composite methodology to prevent ship propeller erosion. *Ocean Engineering*, 195, 106751.

Mujal-Colilles, A., Castells, M., Llull, T., Gironella, X., & Martínez de Osés, X. (2018). Stern twin-propeller effects on harbor infrastructures. Experimental analysis. *Water*, 10(11), 1571.

Castells-Sanabra, M., Mujal-Colilles, A., LLull, T., Moncunill, J., de Osés, F. M., & Gironella, X. (2021). Alternative manoeuvres to reduce ship scour. *The Journal of Navigation*, 74(1), 125-142.

Conference Proceedings:

Llull, T., Mujal-Colilles, A., Castells, M., & Gironella, X. (2020). SHIP PROPELLER EFFECTS ON HARBOURS. *Coastal Engineering Proceedings*, (36v), 15-15.

Llull, T., Mujal-Colilles, A., Castells, M., Gironella, X. (2020). Manoeuvre analysis and simulation to prevent seabed scour due to ship propellers. *In Maritime Transport VIII: proceedings of the 8th International Conference on Maritime Transport: Technology, Innovation and Research: Maritime Transport'20* (pp. 169-179). Universitat Politècnica de Catalunya. Departament de Ciència i Enginyeria Nàutiques.

Llull, T., Mujal Colilles, A., Gironella Cobos, X., Castells Sanabra, M., Martínez de Osés, F. X., Martín Mallofré, A., & Sánchez-Arcilla Conejo, A. (2018). Ship manoeuvre analysis and simulation to obtain scouring related propeller variables. In *Annual General Assembly (AGA) of the International Association of Maritime Universities (IAMU): proceedings* (pp. 296-304). International Centre for Numerical Methods in

Engineering (CIMNE).

Llull, T., Mujal-Colilles, A., Castells, M., Gironella, X., Martínez de Osés, X., Martín, A., & Sánchez Arcilla, A. (2018). Hybrid Tool to Prevent Ship Propeller Erosion. In *ASME 2018 37th International Conference on Ocean, Offshore and Arctic Engineering*. American Society of Mechanical Engineers Digital Collection.

Mujal Colilles, A., Llull, T., Castells Sanabra, M., Gironella Cobos, X., Martínez de Osés, F. X., & Sánchez-Arcilla Conejo, A. (2018). Ship manoeuvring effects on propeller induced erosion. *Proceedings of the 7th International Conference on the Application of Physical Modelling in Coastal and Port Engineering and Science (Coastlab18)*.

Castells, M., Mujal-Colilles, A., Llull, T., Gironella, X., Martínez de Osés, F. X., Martín, A., & Sánchez-Arcilla, A. (2018). Ship manoeuvre patterns to prevent propeller scouring effects. In *34th PIANC World Congress, Panama 2018 May 7 to 11: Connecting Maritime Hubs Globally: Book of Abstracts* (Pp. 238-1). World Association for Waterborne Transport Infrastructure (PIANC).

List of Figures

List of Tables

List of Abbreviations

B & F	Back and Forth
B.A.R	Propeller's Blade Area Ratio
BSS	Bed Shear Stress
CV	Coefficient of Variation
DCZ	Down-Crossing Zero
DEM	Digital Elevation Model
EV	Efflux velocity
FWD	Forward
FWA	Front Wall Area
FWH	Front Wall Hole
GT	Gross Tonnage
HBA	Harbor Basin Area
HBH	Harbor Basin Hole in Forward experiments
HBH$_{FWD}$	Harbor Basin Hole due to Forward rotation in Back & Forth experiments
HBH$_{BWD}$	Harbor Basin Hole due to Backward rotation in Back & Forth experiments
HDG	Ship Heading
MS1A	Maneuver Section 1 Arrival
MS2A	Maneuver Section 2 Arrival
MS3A	Maneuver Section 3 Arrival
MS1D	Maneuver Section 1 Departure
MS2D	Maneuver Section 2 Departure
MS3D	Maneuver Section 3 Departure
RMSE	Root Mean Squared Error
SG	Strain Gauge
SOG	Ship Speed Over Ground
SSS	Shear Stress Sensor
TIN	Triangulated Irregular Network
UCZ	Up-Crossing Zero
UKC	Under Keel Clearance
ZFE	Zone of Flow Establishment
ZEF	Zone of Established Flow

List of Symbols

$\mathbf{a}$	horizontal distance (m)
$\mathbf{a}_p$	horizontal distance between twin-propellers axis(m)
$\mathbf{A}_{plate}$	Area of the shear plate (m^2)
$\mathbf{C}_h$	Clearance distance of the propeller axis/hub (m)
$\mathbf{C}_f$	Friction coefficient (-)
$\mathbf{C}_{fr}$	Friction coefficient over rough bed(-)
$\mathbf{C}_{fs}$	Friction coefficient over hydraulically smooth bed (-)
$\mathbf{D}_h$	Propeller's hub diameter (m)
$\mathbf{D}_0$	Propeller diameter at the contraction plane (*vena contracta*) (m)
$\mathbf{D}_p$	Propeller diameter (m)
$\mathbf{d}_{50}$	Median sediment size (m)
$\mathbf{d}_{85}$	Particle size where 85 % of particles are finer by weight (m)
$\mathbf{d}_{90}$	Particle size where 90 % of particles are finer by weight (m)
$\mathbf{E}$	Young's modulus (Nm^{-2})
$\mathbf{E}_r$	Erosion rate (ms^{-1})
$\mathbf{F}_{plate}$	Horizontal force acting over the shear plate (N)
$\mathbf{Fr}$	Froude number (-)
$\mathbf{Fr}_d$	Densimetrical Froude number (-)
$\mathbf{Fr}_w$	Wall - Froude number (-)
$\mathbf{f}$	Distance between neutral line and outer layer of the steel beam (m)
$\mathbf{f}_{PG}$	Fraction of the pressure gradient force acting on the shear plate (-)
$\mathbf{g}$	Gravitational acceleration (ms^{-2})
$\mathbf{I}$	Inertial moment (m^4)
$\mathbf{K}$	Numerical constant (-)
$\mathbf{K}_T$	Thrust coefficient (-)
$\mathbf{l}$	Energy gradient line (-)
$\mathbf{l}_g$	Length of the gap between the shear plate and the false floor (m)
$\mathbf{L}$	Lever arm (m)
$\mathbf{L}_m$	Characteristic length of the propeller (m)
$\mathbf{M}$	Bending moment acting at the SSS (Nm)
$\mathbf{n}$	Propeller speed of rotation (s^{-1})
$\mathbf{P}_T$	Total pressure (Pa)
$\mathbf{P}_D$	Dynamic pressure (Pa)
$\mathbf{P}_S$	Static pressure (Pa)

P	Engine power (W)
p'	Propeller pitch ratio (-)
Q	Discharge (ls^{-1})
R	Hydraulic radius (m)
$\mathbf{R}_m$	Radial distance from the propeller hub to the position of maximum time-averaged velocitie
$\mathbf{R}^2$	Determination coefficient (-)
Re	Reynolds number (-)
$\mathbf{Re}_d$	Reynolds number based on the Pitot-static inner tube diameter (-)
$\mathbf{Re}_f$	Reynolds number of the flow (-)
$\mathbf{Re}_g+$	Reynolds number of the gap (-)
$\mathbf{Re}_p$	Reynolds number of the propeller (-)
S	Scour Depth (m)
$\mathbf{S}_{conf}$	Scour Depth due to confined jets(m)
$\mathbf{S}_{m,e}$	Maximum scour depth in the equilibrium profile (m)
$\mathbf{S}_{m,t}$	Maximum scour depth at any time (m)
$\mathbf{S}_{unconf}$	Scour Depth due to unconfined jets(m)
T	Propeller Thrust (N)
TI	Turbulence Intensity (ms^{-1})
t	Time (s)
$\mathbf{U}_0$	Efflux velocity (ms^{-1})
$\mathbf{U}_*$	Shear velocity (ms^{-1})
u'	Horizontal velocity fluctuations (ms^{-1})
$\mathbf{u}_{x,r}$	Mean velocity at a position x and distance r from the propeller axis (ms^{-1})
$\mathbf{u}_b$	Horizontal velocity at bottom level (ms^{-1})
$\mathbf{V}_{plate}$	Volume of the shear plate (m^3)
W	Section modulus (m^3)
$\mathbf{X}_m$	Axial distance from the propeller plane to the measuring point (m)
$\mathbf{X}_{mu}$	Axial distance to the maximum velocity at bed (m)
$\mathbf{X}_{plate}$	Horizontal distance to the shear plate (m)
$\mathbf{X}_w$	Horizontal distance from the propeller plane to the Front Wall or Wall clearance (m)
$\mathbf{Y}_m$	Transverse distance from the propeller hub to the measuring point (m)
$\mathbf{Z}_m$	Vertical distance from the propeller hub to the measuring point (m)
β	Blade Area Ratio (-)
ε	Measured elongation by the strain gauges (-)
μ	Dynamic Viscosity of Water (Nsm^{-2})
ν	Kinematic Viscosity of Water (m^2s^{-1})
σ	Standard deviation
σ_b	Bending Stress (Nm^{-2})
ρ_w	Water density (kgm^{-3})
τ_0	Bed shear stress (time-averaged) (Nm^{-2})
τ_{ds}	Bed shear stress (reach-averaged) (Nm^{-2})
Ψ	Shield's parameter (-)

Ψ_{cr}	Critical Shield's parameter of the bottom material (-)
β_{is}	Isbash parameter (-)
$\beta is, cr$	Critical Isbash parameter of the bottom material (-)

Chapter 1

Introduction

1.1 Context of the Thesis

Coastal infrastructures are a focus of growing interest due to the evolution of the shipping industry in recent decades. In particular, the increase of maritime transport leading to a global increment of ship routes, ship size and propulsion systems, is affecting docking infrastructures designed to host smaller and less powerful ships (Hawkswood, Lafeber, and Hawkswood, 2014). This is particularly true in case of ferry ships or cruise ships, equipped with transverse thrusters which allow them to maneuver without the assistance of tug boats. Moreover, these ships use to operate with regular basis at the same ports, meaning that the induced loads during the maneuvers have a cumulative effect over the soil. The use of more powerful propulsion systems causes severe damages to berthing structures regardless of their design (open quays or quay walls). These damages are mainly related to scouring effects due to the stern propellers jets, which create a hole that can reach several meters in depth, especially in case of non-cohesive soils. At the same time, the eroded sediment settles elsewhere in the harbor basin, leading to accretion areas in specific locations. Therefore, two main problems arise from the propeller induced scour near marine structures: on the one hand, the stability may be compromised due to the loss of passive pressure; on the other hand, sedimentation areas may arise reducing the operational draught of any harbor basin due to the resuspended sediment. Proper management of harbors requires up-to-date studies in this topic due to the constant evolution propellers design and increase in ships size.

According to PIANC (2015), ship propeller induced jet flow is the main cause of scour at navigation channels and harbor environments. As a rule of thumb, one can expect flow velocities up to 10 ms^{-1} in case of main propellers and 8 ms^{-1} in case of bow-thrusters. This fact becomes relevant when the bed-clearance is too low that the loads at the bottom level due to the propeller jets overcome the threshold of stability of the bottom material, and therefore induce resuspension and transport. For instance, bottom velocities due to main propellers can be expected to lay between 5 and 8 ms^{-1} (Hawkswood, Lafeber, and Hawkswood, 2014). In case of bow-thrusters, the proximity between the propeller outflow and the berthing quay

when the ship is alongside makes the jet flow to be confined by the structure. In these cases, bottom velocities between 2 and 5 ms^{-1} are common at field (Roubos, Blockland, and Van Der Plas, 2014). In extreme cases, the required diameters of the rock protection may be greater than 1 m (BAW, 2005), which is often impractical and may lead to major cost increases.

Although this problem has been recognized for decades, reliable predictions against scour due to propellers and thrusters remain difficult due to the following factors (Hoffmans and Verheij, 2021):

- The duration of the hydraulic load is short and its location changes during a single maneuver;
- The scour depth increases due to the cumulative effect of several maneuvers at the same location;
- The hydraulic load on the bottom is not the same for all maneuvers, but varies depending on the ship size, draught, water level in tidal areas, wind condition and human factor;
- The engine power actually used is often unknown and needs to be estimated, but it may change significantly depending on the maneuver requirements;
- The amount of cohesion of the bottom material is often not well known;

According to Hawkswood, Lafeber, and Hawkswood (2014), the most significant flow velocities at bed occur when the ship is nearly stationary. From this assumption, the experiments at model or prototype scale have been traditionally performed at zero speed of advance, i.e., at bollard pull conditions. Experiments at physical model have been for decades the only approach to the topic, either focused in local scour experiments or propeller jet flow measurements. Experimental work has provided necessary knowledge in the propeller jet flow characteristics and the interaction with the sediment bed in some of the standard situations that are expected at field. According to BAW (2010), the standard situations are defined by combining the following boundary conditions: jet splitting by a central rudder, lateral limitation of the jet spreading and jet deflection by a quay wall. However, other boundary conditions may be found at field. The propeller characteristics, the number of propellers or the ship stern shape are examples of these boundary conditions. If the ship maneuver is also considered, then the problem becomes even more complex, since the engine power, propellers location, propellers regime and rudder angle changes within a single maneuver. Because of the former, it may be possible that the developed equations at laboratory provide no satisfactory results when applied at field. As an example, Roubos, Blockland, and Van Der Plas (2014) presented measurements of propeller induced scour near a quay wall at prototype scale at the Port of Rotterdam. The most common equations in PIANC (2015) to predict the maximum

scour depth were tested. Significant differences between observed and predicted scour depth were found in their study, showing that sometimes the computed scour is underestimated and in other cases overestimated. Still, experiments at physical model are nowadays one of the best ways to approach the scour problem, and the major part of scientific literature in this topic comes from experimental research.

Aiming to bridge the research at laboratory with the field studies, this thesis applies a methodology to account for the uncertainties due to the ship maneuver and the engines behavior in real scenarios. The methodology was already presented in Llull et al. (2020) and is applied here to a case study. Moreover, the present work includes new experimental studies on single and twin propellers, presenting new findings in the topic that are later applied to the case study.

1.2 Objectives and scope of the Thesis

Single and twin propellers are two of the most common types of propulsion systems in both maritime and inland ships. These propeller systems have been, therefore, focus of the main research performed traditionally in propeller induced scour, but some knowledge gaps are still present in literature. This thesis aims at providing new insights in the study of the propeller jet and the induced scour both for single and twin propellers through experimental work related to both systems.

The fundamental parameter needed in both single and twin propeller systems is the propeller outflow velocity. This parameter needs to be experimentally determined to avoid uncertainty due to the use of literature formulation. The first objective of the experimental work is, therefore, to obtain reliable measurements on the propeller jet velocity field nearby the propeller plane.

In case of single propellers, a common standard situation (free propeller over horizontal bed) is used to address a fundamental topic in sediment scour: the bed shear stress. The bed shear stress is the most important parameter to determine the incipient motion and the bottom stabiliy. It has been used traditionally as input to the bottom stability equations (Shields criterium) and transport equations (Paintal, 1971). However, no systematic research has been focused on direct or indirect measurements of bed shear stress in case of propeller jets so far. Through direct measurements with a self-constructed shear plate, this issue is addressed in the present work aiming to provide new insights in this topic.

According to Gijt and Broeken (2005), an accurate estimation of the maximum expected scour depth near quay walls is needed to set a proper design depth or to account for the added costs of toe protection. In this regard, new experimental work in local scour induced by twin-propeller systems in a confined scenario is presented

herein. In this work, special attention is paid to the evolution of the maximum depth of scour. The experiments address a common situation in the case of Ferry and RO-RO ships that until now have hardly been studied at model scale.

Finally, regarding port management, PIANC (2015) and Hoffmans and Verheij (2021) consider ship maneuvers to be of special relevance to adequately address the scour problem in any specific case. The use of the existing equations is recommended according to the judgment of experts and considering all the boundary conditions (motion of the boat, identification of most damaging situations, consideration of mean or severe meteorological conditions, etc.). This thesis includes a case study, aiming at providing new evidence on the need to take into account the ship behavior as the main driving force behind the scour phenomenon. The behavior of propellers and engines during a real maneuver and the relationship between the maneuver pattern and the induced scour are topics discussed in this part of the thesis.

The following specific objectives are therefore defined to achieve the overall goal:

- Characterization of the induced velocity field by the propeller models to be used through the dissertation.
- Direct measurements on bed shear stress by propeller jets at model scale.
- Adjustment of empirical relations between the time-averaged bed shear stresses and the propeller induced velocity.
- Analysis of the local scour due to twin-propeller confined jets, including time evolution of the maximum scour depth near the front wall.
- Analysis of the local scour due to backward rotating twin-propellers.
- Maneuver analysis of a real ship to detect the most harmful situations, i.e., when a specific ship is expected to induce higher loads to the sediment bed.

1.3 Layout of the Thesis

This dissertation is divided into five different Chapters, focused on the propeller induced sediment scour over non-cohesive sediment in low bed clearance conditions.

Chapter 1, i.e., the present Chapter, starts with the context and motivation of the subject. The purpose of the work, the objectives and the layout of the thesis are also provided in this Chapter.

Chapter 2 is focused on the effects of single propeller jets over the bed sediment. Experimental work in propeller jet velocity and bed shear stress is presented. Measurements of the jet velocity at the so-called *efflux plane* are related with the directly

measured bed shear stress by an empirically obtained coefficient. The bed clearance, i.e., the vertical distance between the propeller and the bottom, and the propeller speed of rotation are included as experimental variables in the analysis.

Chapter 3 is focused on twin-propeller systems in a confined situation. Although very common in a wide range of ships (e.g., Ferry, RO-Pax, Cruise ships), few studies are found in literature in this topic. The velocity measurements performed in Chapter 2 are used in this Chapter to relate the previously measured efflux velocity of propeller jet velocity with the maximum measured scour depth.

Chapter 4 presents a case study in which the ship maneuver is related to the scour pattern combining three elements: bathymetric surveys in a specific harbor basin, AIS data of the study ship during the maneuvers in the specific basin, and maneuver simulation to obtain the engine behavior during the maneuver. As in Chapter 3, this is a twin-propeller ship in a low bed-clearance environment. After the maneuver simulation, the engine regime (i.e., ahead and astern regime) and the use of the bow-thrusters are obtained and related with the observed scour pattern in the harbor basin.

Finally, Chapter 5 summarizes the main findings of the present work and proposes recommendations for further research.

Chapter 2

Experiments on propeller jet velocity distribution and induced bed shear stress

2.1 Introduction

Propeller jets in unconfined conditions, i.e., without any boundary or disturbing element conditioning its development, have been studied for decades by naval architects and civil engineers. The former aimed at improving the propeller design, therefore the research performed in this field is focused on the flow characteristics at the vicinity of the propeller, either upstream or downstream. The latter focused their concerns into the jet flow development, that may have effects over sea or river beds, harbor environments, hydraulic structures, etc., which is the scope of the present research. In this chapter, the experimental work performed at the Leichtweiß - Institut für Wasserbau (LWI), at the TU-Braunschweig (Germany), is presented. This work is focused on the velocity field induced by a ship propeller at model scale and the induced bed shear stresses over a rough bed.

The velocity field induced by a propeller jet has been traditionally studied as an analogy to the diffusion of the jet from a submerged orifice, following the pioneer research of Albertson et al. (1950), and based on Froude's axial momentum theory. According to the work in Albertson et al. (1950), the plain water jet can be divided into two distinct zones: the Zone of Flow Establishment (ZFE) and the Zone of Established Flow (ZEF). In the ZFE, at closer distance from the jet origin, the maximum flow velocity in the central core was assumed constant. In this zone, the boundary between the jet slipstream and the ambient water causes turbulent mixing both inwards and outwards the jet. With the increasing distance in the ZFE, the velocity at the central core gradually decreases until the mixing region eventually reaches the central line. At this point, the ZEF begins. In the ZEF, the maximum axial velocity occurs at the centerline and decays with the axial distance.

The next generation of researchers focused on the propeller jet (e.g. Blaauw and Kaa (1978), Verheij (1983), Fuehrer and Romisch (1977), and Hamill (1987)) based their work on Albertson's research line and also divided the propeller slipstream into ZFE and ZEF. In the ZFE, immediately downstream the propeller plane, a low velocity core is found due to the presence of the propeller hub, which makes the location of the maximum velocity, i.e., the *efflux velocity*, to be at a certain distance from the propeller axis. The efflux velocity in case of propeller jets was first investigated by Blaauw and Kaa (1978) and Fuehrer and Romisch (1977) by means of momentum theory and under the assumption of an ideal actuator disc. The derived expression (see Section 2.3.1, Eq. 2.13) was widely used to obtain the efflux velocity of non-ducted ship propellers since then (the derivation can be found in Blaauw and Kaa (1978)). Further work in Fuehrer, Pohl, and Römish (1987) stated that the prediction of the efflux velocity according to the equation derived from the momentum theory yielded errors up to $\pm$ 20%. Since then, more experimental research have been done and new adjustments have been proposed to fit all the experimental results. Recent reviews by Lam et al. (2011) and Wei, Chiew, and Cheng (2020b) made an excellent work to summarize all the proposed expressions to analytically obtain the efflux velocity of a propeller jet, but no general consensus is found regarding this parameter yet. For practical use in propeller jet velocity characterization, PIANC (2015) recommends the use of the axial momentum theory derived equation. In case not all the propeller parameters are known, the empirical expression derived by Blaauw and Kaa (1978), based on the relationship between the propeller thrust and the installed power previously proposed by Schneiders and Pronk (1975), is recommended (see Section 4.3.3, Eq. 4.1). When velocity measurements are available, the efflux velocity can be obtained, according to Ryan (2002), as the maximum velocity downstream the propeller plane, taken from the mean velocity distribution. Due to the difficulty in measuring immediately downstream the propeller plane, a distance of $X = 0.5D_p$ is recommended by the author. The same distance is recommended in BAW (2010) and Hsieh et al. (2013).

When the propeller is rotating in a fluid, the rotating blades of the propeller accelerate the water upstream of the propeller face, which passes between the propeller blades and is discharged downstream, increasing the rearward momentum of the fluid and inducing forward thrust. Due to the propeller rotation, the discharged water downstream the propeller plane is converted into a swirling jet, that spreads and eventually reaches the seabed. After the impingement, the spreading jet is converted to a wall bounded jet, thus inducing shear stresses to the boundary.

The bed shear stress have been traditionally estimated from indirect measurements by different methods, namely the reach-averaged method, the logarithmic law, the quadratic stress law, Reynolds stress method and the turbulent kinetic energy (TKE) method. A description and comparison of these methods is found in

Biron et al. (2004). Some of these methods have been also applied to propeller jets. For instance, the shear stress due to propeller jets was first studied by Blaauw and Kaa (1978), who proposed an empirical friction coefficient, between 0.06 and 0.11, by fitting their experimental results to the quadratic stress law. In their experiments, they used pebble gravel of $d_{50} = 5.45$ mm with a colored pattern and determined the number of particles passing the perpendicular sections. From the number of bottom particles counted during the tests, they could determine a transport parameter. According to Paintal (1971), the transport parameter is related to the Shields parameter in case of very low bed-load transport. This relation was used to determine the Shields parameter and, later, compute the shear stress and the friction coefficient. Blokland and Smedes (1996) used the same relationship between the transport parameter and the Shields parameter to obtain a similar friction coefficient, using the scouring rate measured at erosion tests to calculate the transport intensity. Different materials were tested as bottom protection with d_{50} ranging from 36 to 71 mm. It is remarkable that these tests were performed in situ at the port of Rotterdam. The friction coefficient and the stability condition in case of finer sediment was studied by (Hamill, 1988), from Reynolds stresses computed close to the sediment bed after velocity measurements within an equilibrium scour hole. A more direct method was used in Maynord (2000) and Rodríguez et al. (2002), who measured bottom shear stresses of a passing ship by using hot film wall shear stress sensors flush mounted at the bottom of a channel. In Maynord (2000) a friction coefficient to obtain peak shear stresses due to propeller jets is proposed, and has been more recently implemented in a numerical tool to simulate the transport and deposition of sediment plumes due to the propeller wash (Wang et al., 2016). More recently, in Wei, Chiew, and Cheng (2020a) a PIV system has been used to obtain measurements of the velocity gradient within the viscous sublayer, allowing computation of both the streamwise and transverse component of the bed shear stress.

Direct measurements of bed shear stresses over a horizontal area can also be obtained using a *shear plate*. In the present work, a shear plate has been developed to measure the propeller jet induced bed shear stress over a sediment bed aiming to validate results from previous studies and provide further insight in the topic. Preliminary results of the experiments have already been presented in Niewerth, Núñez-González, and Llull (2021). Shear plates have been used widely in hydraulic and coastal engineering to directly measure bottom shear stresses (Park et al., 2016; Pujara and Liu, 2014; Barnes et al., 2009; Tinoco and Cowen, 2013; Riedel and Kamphuis, 1973) under different flow conditions and with different measurers, including strain gauges, eddy-current proximity probes, and others. A review of the different sensor types used in shear stress measurers is found in Kolitawong, Giacomin, and Johnson (2010). However, shear plates have not been used in case of propeller jet flow over horizontal boundaries so far.

In summary, the current Chapter aims to characterize the axial velocity field downstream the propeller face and the bed shear stress caused by the propeller jet over a horizontal rough bed, thus obtaining empirical evidence of the relation between the experimental conditions (propeller speed of rotation and bed clearance distance) and the induced shear stresses. The validation of the shear plate to be used in further research is of main interest and new proposals to improve the prototype are derived from the experimental results. Therefore, this chapter is organized as follows: In section 2.2, the description of the instrumentation used to perform the experimental work, their validation and the experimental setup are provided. In section 2.3, the obtained results are shown, focusing on the propeller jet velocity distribution near the propeller plane and the propeller induced bed shear stresses. The mentioned results are discussed in section 2.4. The final remarks from the present chapter are summarized in section 2.5.

2.2 Experimental design and data acquisition

Two different data sets are used in this chapter to analyze the relationship between the propeller speed of rotation and the induced bed shear stress. The experiments performed and the obtained data sets are named as follows: experiments/data on Efflux Velocity (EV) and experiments/data on Bed Shear Stress (BSS).

The first data set (EV data) consists on measurements of the propeller jet free-stream velocity distribution. Punctual velocity measurements were performed along a vertical measuring grid parallel to the propeller plane, at a distance X=0.5D_p, to obtain the time-averaged velocity distribution at the so-called efflux plane. These experiments were carried out in a medium-size water tank of dimensions 4x2x0.6 m with a ship propeller model in bollard pull conditions. Measurements of axial velocity were obtained from 2 different propellers (*Prop1* and *Prop2*) at 2 speeds of rotation (n). The propeller models have the same characteristics but different pitch ratio (p'). The main characteristics are included in Table 2.1.

The second data set (BSS data) is obtained from measurements of the induced bed shear stress by the propeller jet. A false bottom roughened with glued sand of $d_{50} = 0.8$ mm, with a flush mounted shear plate, was used to obtain direct measurements of bed shear stress over a 0.1 squared meters area. The false bottom was built in wooden modules of dimensions 1x0.6x0.2 m next to each other. In this case, the measurements were performed in a larger water tank of dimensions 15x5x2 m, to better fit the objectives of the experimental work. Bed shear stress time-series were obtained from experiments performed with 1 propeller (*Prop1*) at 5 different speeds of rotation (n), 2 different propeller bed clearances (C_h) and 2 different horizontal distances to the shear plate (X_{plate}).

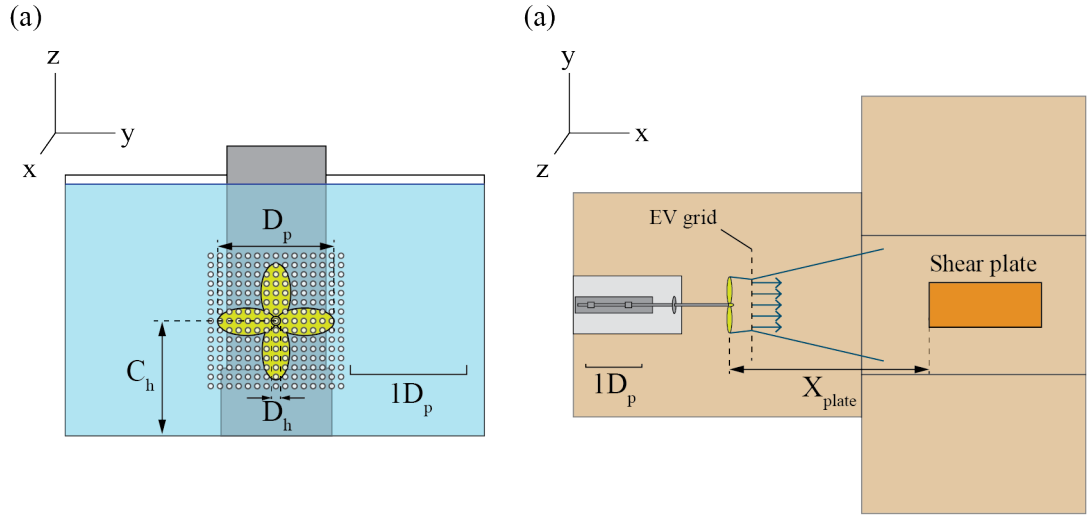

FIGURE 2.1: Sketch of the experimental setup in (a) EV experiments, and (b) BSS experiments. In (b), the vertical dashed line parallel to the propeller plane shows the location of the measuring grid during EV expeirments.

TABLE 2.1: Propeller 1 and Propeller 2 main characteristics.

Name	D_p	D_h	**B.A.R**	p'	**material**	**N**
Prop1	0.25	0.025	0.75	0.8	Cu-Al-Ni alloy	4
Prop2	0.25	0.025	0.75	1.0	Cu-Al-Ni alloy	4

Sketches of the experimental setup of the EV and BSS experiments are shown in Figure 2.1 (a) and (b), respectively. The origin of Cartesian coordinates system adopted in this work is located at the propeller hub, while the x, y, and z axes are taken in the axial, transverse and vertical directions. The summary of all the experiments presented in this chapter, along with the name and the experimental conditions, is provided in Table 2.2.

In the following sections (2.2.1 and 2.2.2) the description of the measurement equipment, calibration measurements, validation tests and performed experiments is provided.

2.2.1 Velocity measurements with pitot-static tube and pressure transducers

The EV experiments were performed by point-by-point velocity measurements along the measuring grid with a Pitot-static tube, also called Prandtl tube, coupled to a differential pressure transducer. The dimensions of the probe and a picture taken during the validation tests are shown in Figure 2.2 (a) and (b).

TABLE 2.2: Experimental setup during EV and BSS experiments. The variables X_m, Y_m, and Z_m states for the range of axial, transverse and vertical distance within the measuring area.

exp #	Propeller	C_h	X_m	Y_m	Z_m	n(rpm)
EV1	*Prop1*	$1D_p$	$0.5D_p$	$-1D_p$-$1D_p$	$-1D_p$-$1D_p$	250,300
EV2	*Prop2*					
BSS1	*Prop1*	$1D_p$	$2.9D_p$-$4.9D_p$	$-0.4D_p$-$0.4D_p$	-	150,225,300, 375,450
BSS2		$0.7D_p$				
BSS3		$1D_p$	$3.7D_p$-$5.7D_p$			
BSS4		$0.7D_p$				

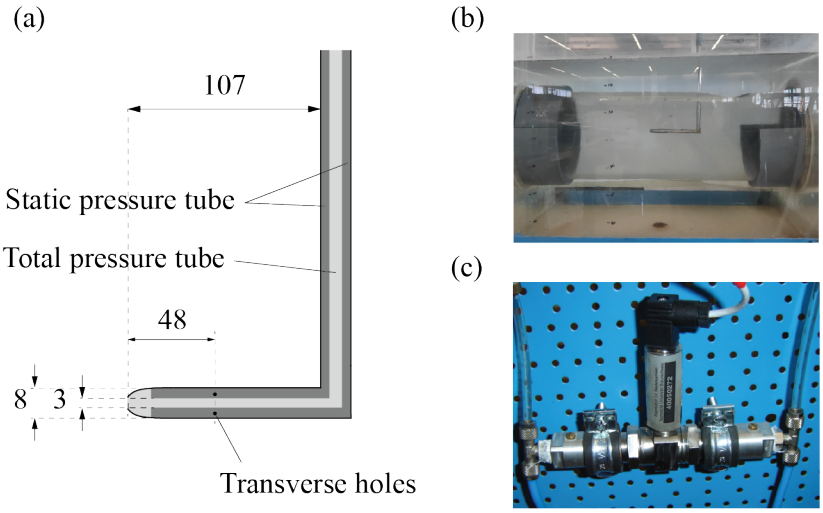

FIGURE 2.2: (a) Sketch of the Pitot-static tube. All the distances in the sketch are shown in mm. (b) Picture of the tube during a calibration test. (c) Picture of the pressure transducer used in the experiments.

During the experiments, the probe was aligned to the main flow direction, thus the inner tube measured the total pressure at the stagnation point, as a sum of the static and dynamic pressure of the water flow. The outer tube has four smaller holes in the side wall. Due to the alignment of the probe, the small holes were perpendicular to the main flow direction, then just static pressure was measured in the pipe connected to the outer tube. Both of the pipes coming out of the probe were connected to each side of a differential pressure transducer, thus measuring the pressure difference between the pipes. By applying Bernoulli's principle to the jet flow in the pipes, Eq. 2.1 and Eq. 2.2, the difference between the total pressure and the static pressure is the dynamic pressure, which is a direct measure of the magnitude of the axial component of the flow velocity.

$$P_T = P_S + P_D \tag{2.1}$$

$$P_D = \frac{1}{2}\rho_w u^2 \tag{2.2}$$

where:

P_T = Total Pressure (Pa)
P_S = Static Pressure (Pa)
P_D = Dynamic Pressure (Pa)
ρ_w = Water density (kgm^{-3})
u = Flow velocity (ms^{-1})

The differential pressure measurements were performed with bidirectional pressure transducers (Omega Engineering ^{TM}), Figure 2.2 (c), able to measure pressure differences up to $\pm$ 25 HPa, while the specified accuracy is 5%. The sampling frequency during the velocity measurements was set to 100Hz. The connection between the pressure probe and the pressure transducer was made by tightly fixed silicone tubes. The transparency of the tubes allowed to check that no air was inside the pipes to ensure hydraulic connection between the probe opening and the pressure transducer chamber. The same circuit was also connected to the water tank through a water level cylinder to adjust the water level and to drain the system after every experimental run. The connection between the water level cylinder and the pressure transducer was closed after the draining and previous to the beginning of the experiment by two different valves, one for each chamber. Figure 2.3 (a) and (b) shows a sketch of the circuit and a picture of the sensors panel to the good guidance of the reader. The measurements considered in the present chapter are obtained by one of the four pressure transducers in the picture.

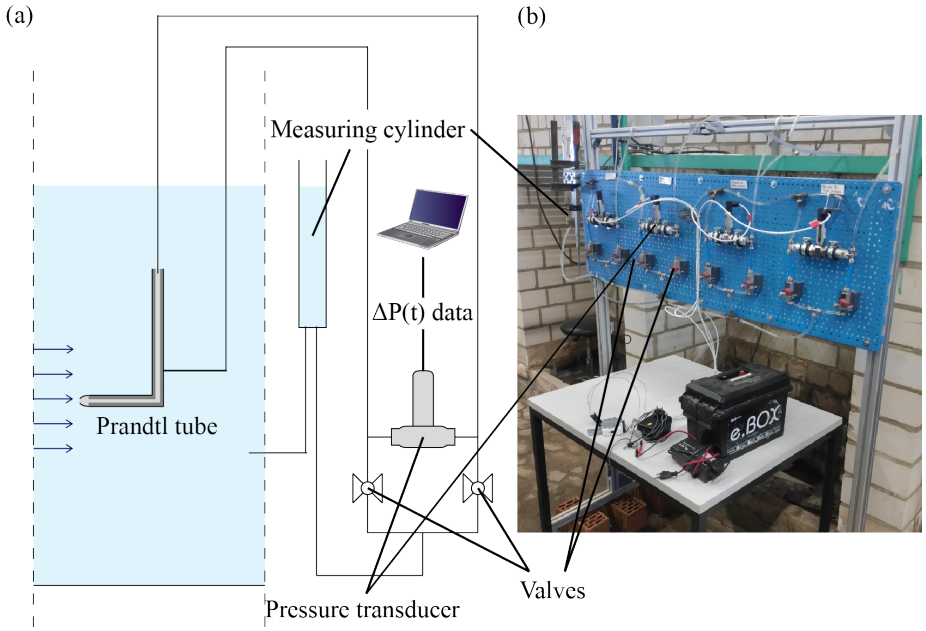

FIGURE 2.3: (a) Sketch of the measurement system at the tank. (b) Picture of the pressure sensors panel.

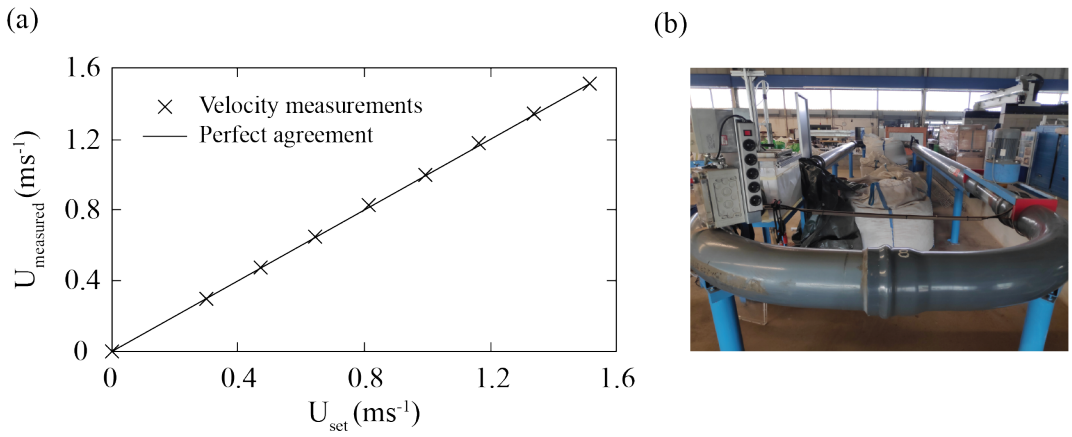

FIGURE 2.4: (a) Results of the validation tests of the Pitot-static probe and pressure transducer measurements. (b) Picture of the calibration flume.

The validation of the instrument was performed in a closed circuit flume, where different flow velocities ranging from 0.3 to 1.5 ms^{-1} were set. Figure 2.4 shows a picture of the validation flume, together with the validation tests results. Almost perfect agreement between the set velocity and measured velocity with the pitot-static probe measurements was obtained. Besides, the repeatability of the time-averaged velocity measurements in the propeller jet was tested by performing 3 repetitions of measurements over 4 different vertical profiles with *Prop2* at 300 rpm. A maximum absolute error of a 6% was found, while the relative standard error for the maximum velocity at each profile was lower than the 2% in all cases.

During the EV experiments, the squared-grid of $1D_p$x$1D_p$ shown in Figure 2.1 (a) was centered at the propeller hub. The vertical and horizontal distance between points was $0.08D_p$ (2 cm). A total of 4 grids of 225 measuring points, measuring the flow field of *Prop1* and *Prop2* at two different speeds of rotation, were performed. The time duration of every velocity measurement was set to 80s after a set of preliminary measurements over a 12-points grid to obtain the error of the cumulative time-average to the long-term average (3 minutes time-series). Measurements of 80s were enough to obtain time-average velocity values with an accuracy of $\pm$5% within the free jet. In Figure A.1, in the Appendix A of this work, the cumulative average of the time-series are plotted to show the mean value stabilization in the free jet measurements. The test measurements were performed at a distance of X=$1D_p$ from the propeller plane and the chosen measuring time was kept the same in all the velocity measurements.

Uncertainty and sources of error during jet velocity measurements

Pitot tubes are designed to work under steady linear flow to accomplish with Bernoulli's theorem constraints (Eqs. 2.1 and 2.2). Therefore, several assumptions are needed

when considering that each instantaneous pressure difference measured in the transducer corresponds to a measure of the instantaneous velocity of the jet flow. First, Eq. 2.1 and Eq. 2.2 are not applicable to turbulent jet flows, yielding a certain degree of uncertainty in the results. Nevertheless, the validity in measurements with Pitot tubes in turbulent flow fields is proven in literature (Becker and Brown, 1974; Bailey et al., 2013; McKeon et al., 2003). Moreover, this particular Pitot-static tube has already been used under propeller jet flow conditions, with adequate results in terms of time-averaged measurements at the *efflux plane* (Núñez-González, Koll, and Spitzer, 2018). On the other hand, it is well known that Pitot tubes' performance is affected by viscosity when measuring at low water flow velocities. In Spelay et al. (2015) the authors recommend not to use Pitot tubes in case of Reynolds numbers (Re_d) under 35. Note that the Re_d is calculated in this case with the inner tube diameter. In the present experiments, time-average flow velocities below 0.5 ms^{-1} are not expected within the propeller jet, meaning $Re_d > 1500$, thus the error due to viscosity is neglected. Finally, the propeller jet is known to be a turbulent 3D jet where not only axial, but also tangential and radial components of the velocity are important. This is especially true at close distance from the propeller plane. Therefore, since the present measurements are performed with a Pitot-static tube, important information on the propeller jet velocity distribution -the radial and tangential components- is lost. Moreover, the alignment of the probe with the flow cannot be ensured in case of three dimensional velocity field. Still, since the main purpose of the measurements is to obtain the time-averaged distribution of the axial velocity component in the jet, the measured velocities by the pitot tube are considered to fit in the scope of the experiments.

2.2.2 Shear stress measurements with shear plate

The measurements of propeller induced bed shear stress were performed by a self-made shear plate, flush mounted in a false bottom and coupled to a load cell with strain gauges below. The gap between the shear plate and the false bottom was 3 mm, allowing the plate to move in the mean flow direction during the experiments. This displacement was measured by the strain gauges. In Figure 2.5, a sketch of the load cell coupled to the shear plate is shown. The strain gauges used in this work have been satisfactorily used as drag force sensors in several previous studies at the LWI, to measure drag force over individual plants and solid elements under several flow conditions with high accuracy (Schoneboom et al., 2008; Niewerth, Aberle, and Folke, 2019; Niewerth et al., 2016; Siniscalchi, Nikora, and Aberle, 2012). Since the instrument was used to measure shear stresses in the reported experiments in this work, it will be named Shear Stress Sensor (SSS) for the sake of simplicity.

The force acting on the shear plate in the streamwise direction can be expressed as a sum of the shear forces over the plate's surface and the pressure gradient force, acting at the upstream edge, due to the difference in pressure at each side of the

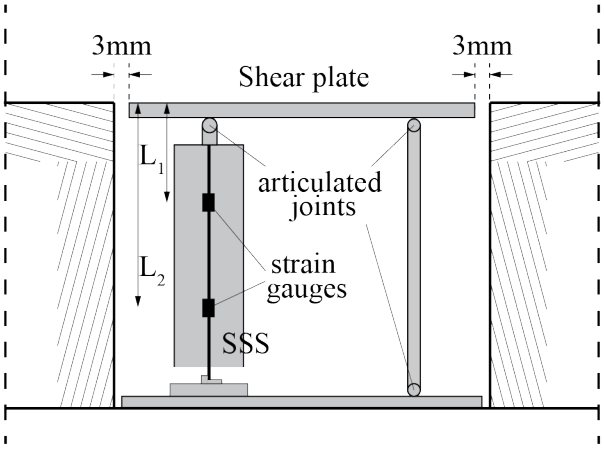

FIGURE 2.5: Sketch of the Shear Stress Sensor (SSS) coupled to the shear plate.

plate (Eq. 2.3). The effective fraction of the pressure gradient force acting over the plate (f_{PG}) is usually assumed to be 0.5, since linear decay between the top and the bottom of the shear plate cross-section at the upstream edge is assumed (Pujara and Liu, 2014). The pressure gradient could not be measured during the experiments presented here. The uncertainty derived from neglecting this term is addressed in Section 2.2.2: *Uncertainty and sources of error during bed shear stress measurements*. In the present work, the total force over the shear plate is assumed to be due the shear stress acting at the top surface of the plate. This force is measured with the SSS.

$$F_{plate} = \tau_0 A_{plate} + f_{PG} \frac{\partial P}{\partial x} V_{plate} \tag{2.3}$$

where:

F_{plate} = Total force acting on the shear plate (N)
τ_0 = Mean bed shear stress (Nm^{-2})
A_{plate} = Total Area of the plate (m^2)
V_{plate} = Total Volume of the plate (m^3)
$\partial P/\partial x$ = Horizontal pressure gradient (Nm^{-3})
f_{PG} = Fraction of the pressure gradient acting on the shear plate (-)

The SSS consists on a 20 mm wide and 3 mm thick stainless-steel beam with eight strain gauges composed as 2 Wheatstone full bridge circuits located at different vertical positions. The vertical separation between the strain gauges is approximately 8 cm. The steel beam is covered by a plastic tube, perfectly sealed at the top, preventing water intrusion when located underwater and allowing the strain gauges (SG) to operate in dry conditions. The lower part of the beam is fixed to an aluminum plate that, in turn, is fixed to the bottom. The upper part of the beam is fixed to an aluminum head that is coupled to the shear plate with an articulated joint, thus allowing a friction-free horizontal movement of the plate. Due to the horizontal force

acting over the plate, it is displaced inducing a bending moment over the steel beam, that is deflected. The deflection is measured as output voltage at the 2 Wheatstone bridge circuits.

Considering the steel beam as a rectangular cross-section, fixed at the bottom and subjected to an external forcing, F (N), normal to the cross-section and at its top, the bending moment, M (Nm), at a distance L (m) is obtained by the moment equation, Eq. 2.4. The bending stress (σ_b) at the surface of the bending beam, i.e. at the external layer, is calculated with Eq. 2.5. The bending stress is also linearly related to the measured elongation (ε) by Eq. 2.6, where the proportionality is given by the Young's Modulus of the material.

$$M = F_{plate} L \tag{2.4}$$

$$\sigma_b = M J^{-1} f = F_{plate} L W^{-1} \tag{2.5}$$

$$\sigma_b = E\varepsilon \tag{2.6}$$

where:

J = intertial moment of the transversal section (m^4)
f = distance from the neutral line to the outer layer (m)
W = Section modulus (m^3)
E = Young's Modulus or Modulus of Elasticity (Nm^{-2})

Substituting in the previous equations, the expression to calculate the lever-arm (L_1 and L_2 in Figure 2.5) acting at each measuring position of the strain gauges when the beam is deflected is obtained (Eq.2.7).

$$F_{plate} L_n = EW\varepsilon \tag{2.7}$$

Substituting Eq. 2.7 in Eq. 2.3 and neglecting the pressure gradient, the mean shear stress (τ_0) is obtained as:

$$\tau_0 = \frac{EW\varepsilon}{A_{plate} L_n} \tag{2.8}$$

In order to relate the shear stress acting along the plate with the measured deflection at the strain gauges position, the Eq. 2.7 is calibrated with known forces. The calibration is performed at dry conditions, with a pulley system and hanging weights. Low weights are attached to the pulley, placed at the same height as the shear plate, and fixed to it with a small screw. The results obtained during the calibration tests are summarized in Table 2.3.

The validation of the shear plate under water flow was performed in a horizontal flume of dimensions 25x0.7x0.6 m, where different discharges up to 120 ls^{-1}

TABLE 2.3: Results of the calibration tests of the of the SSS.

Strain Gauge (SG)	E	W (m^3)	L (mm)	Repetitions	Absolute error (mm)
SG1	$2x10^5$	30	$L_1 = 62.71$	2	3.83
SG2	$2x10^5$	30	$L_2 = 144.97$	2	3.79

were set. The false floor modulus containing the shear plate was perfectly fitted to the flume width to prove the functionality of the prototype. During the trial tests, the energy slope (S_f) was obtained with the linear regression of the total hydraulic head calculated at 5 different channel sections over the false floor. The last was obtained a sum of the elevation head and the velocity head (pressure is assumed hydrostatically distributed). To calculate both parameters, the free surface elevation was measured with point gauges at each section, with a precision of 0.5 mm in the measurement. The reach-averaged shear stress (τ_{ds}) was later obtained with Eq. 2.9, assuming normal flow conditions due to the small angle between the horizontal bed and the water free surface. The time-averaged bed shear stress obtained from the shear plate (τ_0) was later compared to the reach-averaged bed shear stress (τ_{ds}). In Figure 2.6, an sketch of the validation experiments and a picture of the shear plate in the validation flume are shown.

$$\tau_{ds} = \rho_w g R S_f \tag{2.9}$$

where:

τ = mean bed shear stress (Nm^2)
g = gravitational acceleration (ms^{-2})
R = hydraulic radius (m)
S_f = energy slope (-)

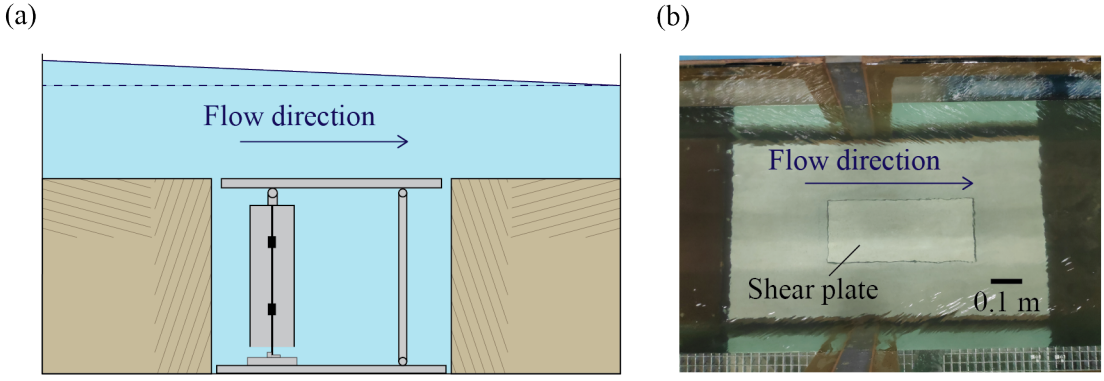

FIGURE 2.6: (a) Sketch of the shear plate flush mounted on the false floor modulus and located in the validation flume; (b) picture of the tests at the validation flume.

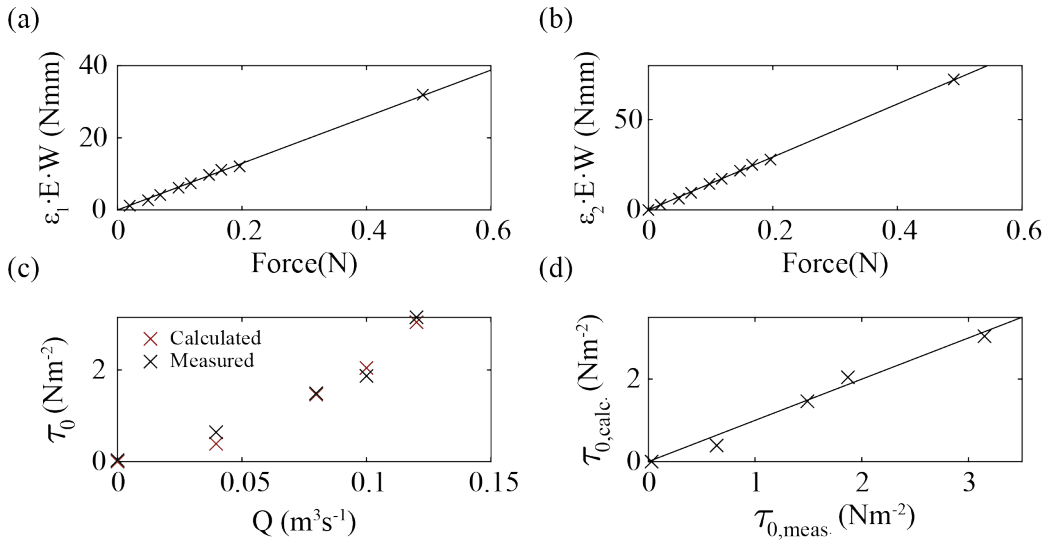

FIGURE 2.7: (a), (b) calibration of the shear plate (SG1 and SG2); (c), (d) results of the tests in the validation flume.

The calibration line and the results obtained at the validation tests are shown in Figure 2.7. A fairly good behavior of the shear plate is obtained under steady normal flow, with RMSE = 0.15 Nm^2 in the present tests.

Uncertainty and sources of error during bed shear stress measurements

The use of the shear plate and the measurement of shear stress with strain gauges has been proven to be well-working, although subjected to intrinsic uncertainties that need to be considered. The main source of uncertainty may come from the spatial integration of a punctual measurement over a 0.1 m^2 area. However, a compromise between the uncertainty and the sensibility of the instrument is needed to allow confident results. In this case, low shear stresses of 1 Nm^{-2} correspond to forces of 0.1N over the plate area, within the sensors optimal measuring range.

Since the direct measurement of time-averaged bed shear stress is the main objective of the present experiments, the duration of each experiment is indeed a source of uncertainty. The time-averaged shear stress changes with time, although reaching a certain stabilization. The duration of the measurements is analyzed by comparing the average and the dispersion of 6 repetitions of short (80 seconds) measurements with the same measurement over a long time (20 minutes), to obtain an estimation of the error and proceed with the short-term measurements. This matter is explained in detail in Appendix B.

The friction losses due to the plastic supports and joints have an effect on the resistance to the displacement of the plate. However, these are not considered as a

source of uncertainty since they are already measured during the calibration process.

The pressure distribution along the plate was not measured during the experiments, thus the pressure difference between the upstream and downstream boundary of the plate is neglected. In case of turbulent flow over horizontal bottoms, experience in literature shows that the effect of the pressure gradient is not of main relevance in shear plate measurements. An uncertainty lower than a 10% is assumed, for instance, in (Park et al., 2016). However, due to the specific characteristics of the wall bounded swirling jets, such as the propeller jets, we cannot assume the exact same conditions as in an open channel flow. The assessment of the uncertainty due to the pressure gradient is therefore left for future work.

Some considerations on the gap size are also needed. Since there is no velocity inside the chamber below the plate, it is known that secondary forces may exist due to the exchange of momentum between the external flow and the fluid in the chamber. Defining the Reynolds number based on the gap size as $Re_{g+} = \frac{U_* l_g}{\nu}$, Dhawan (1953) provides a general rule that the velocity profile is unaltered by the presence of gaps up to $l_{g+} < 100$ (Pujara and Liu, 2014). If the shear velocity is obtained from the measurements of bed shear stress in the present work, this threshold is in range with the experimental results in case of low speed of rotation, although it is exceeded in some of the experiments with high speed of rotation, therefore some influence of secondary forces should not be discarded.

2.3 Results

In Sections 2.3.1 and 2.3.2 the obtained experimental results of velocity distribution across the efflux plane and propeller induced bed shear stress, respectively, are presented. In section 2.3.3, the results from EV and BSS experiments are triggered to each other to obtain an empirical fit of the friction coefficient (C_f) over the shear plate as a function of the experimental conditions.

2.3.1 Axial velocity distribution at the propeller face

The results presented in this section are obtained from time-averaged measurements of the axial velocity distribution at a plane parallel to the propeller face, at a distance X=0.5D_p, as introduced in Section 2.2.1. Following the abbreviations used in previous sections, these experiments are called EV experiments, so the obtained data is named as EV data. According to literature, EV measurements are assumed to be obtained at the efflux plane (Ryan, 2002; Wei, Chiew, and Cheng, 2020b), therefore, the maximum time-averaged velocity across the efflux plane, will be known as the efflux velocity (U_0). This parameter is presented in the first place since it will be used throughout this work. Also, since most of the analytic expressions in literature

to characterize the propeller jet depend on U_0 as scaling variable, it is considered highly relevant to the present research.

As stated in section 2.2.1, a total of 225 measurements over a $1D_p$x$1D_p$ grid were performed to measure the differential pressure at each point with the pitot-static tube. Each instantaneous pressure difference was converted to an instantaneous velocity measurement using Eq. 2.2. After that, the mean velocity ($\overline{u}$) and the horizontal turbulence intensity (TI) for each time-series at each position were obtained with Eqs. 2.10 and 2.11, respectively.

$$\overline{u} = \frac{1}{N}\sum_{i=1}^{N} u_i \tag{2.10}$$

$$TI = \sqrt{\overline{u'^2}} = \sqrt{\frac{\sum_{i=1}^{N}(u_i - \overline{u})^2}{N}} \tag{2.11}$$

To obtain U_0 from the measured velocities, two symmetric Gaussian functions are adjusted to the velocity profile at each experiment. The adjustment is performed by optimizing U_0, R_m and σ in Eq. 2.12 by means of least squares fitting. After obtaining U_0, an experimental coefficient of thrust (K_T) is found by applying Eq. 2.13, derived from the axial momentum theory, to every experiment.

$$\frac{U_r}{U_0} = e^{-\frac{1}{2}\frac{r-R_m}{\sigma^2}} \tag{2.12}$$

$$U_0 = 1.59 n D_p \sqrt{K_T} \tag{2.13}$$

In Table 2.4, the obtained values of U_0, R_m, σ and K_T are summarized for each propeller at each speed of rotation. The average value of K_T, from the obtained results at 250 rpm and 300 rpm, is used as unique value of each propeller from this point in the dissertation. The results show that no variation is obtained in the fitted models regarding the radial position of the maximum velocity in any of the experiments.

TABLE 2.4: Summary of the obtained values of efflux velocity (U_0) and thurst coefficient (K_T) in EV experiments.

Propeller	**n (rpm)**	$\boldsymbol{U_0}$	R_m	σ	$\boldsymbol{K_T}$	**RMSE**
Prop1	250	1.15	$0.20D_p$	$0.19D_p$	0.48 ± 0.1	0.096
Prop1	300	1.38	$0.21D_p$	$0.18D_p$	0.48 ± 0.1	0.116
Prop2	250	1.33	$0.20D_p$	$0.19D_p$	0.63 ± 0.3	0.166
Prop2	300	1.55	$0.20D_p$	$0.19D_p$	0.63 ± 0.3	0.234

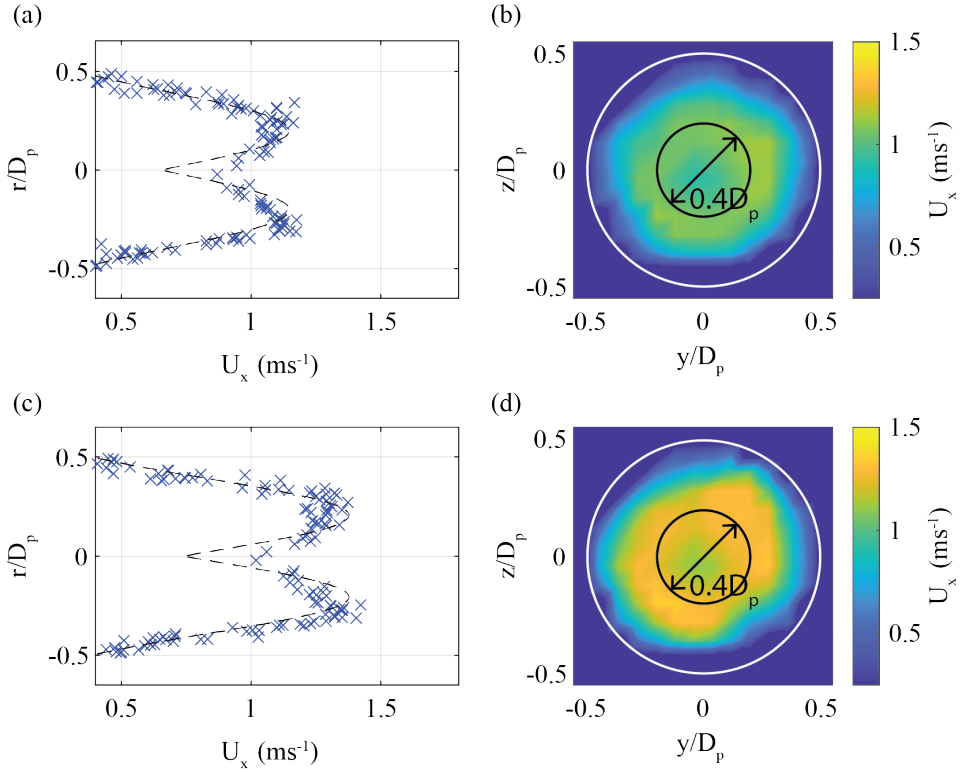

FIGURE 2.8: Velocity distribution at the efflux plane (*Prop1*). (a), (c): Radial distribution of $\overline{u}$ fitted with the double-peak gaussian model at 250 rpm and 300 rpm respectively. (b), (d): 2D colormaps of $\overline{u}$ at 250 rpm and 300 rpm respectively. The black circumference shows the radial location of the maximum velocities, while the white circumference shows the propeller diameter.

The radial distribution of time-averaged velocities fitted with the Gaussian adjustment and colormaps of the axial velocity distribution are show in Figure 2.8, for EV1 experiments. The measurements obtained at radius larger than $0.5D_p$ are excluded, since the expected mean velocity at these points is close to zero. The radial distance locating peak velocities is drawn over the colormap, together with the area of the propeller. The same figure containing the data of EV2 is shown in Figure A.3 of the appendix A. The results obtained in EV2 are presented at this point, but they won't be discussed in the present Chapter since they are used as a part of the analysis in Chapter 3 of this dissertation.

Once the U_0 is characterized, the needed parameters to account for the scaling of the experiment can be obtained. In this work, the adjusted K_T (see Table 2.4) is assumed constant for the range of propeller speeds of rotation covered by the present experiments, in both Sections 2.3.1 and 2.3.2. Therefore U_0 is obtained with Eq. 2.13 as a linear function to the range of propeller speeds of rotation showed in Table 2.2. The Froude number (Fr), Reynolds number of the flow (Re_f) and Reynolds number of the propeller (Re_p) are obtained according to Eqs. 2.14, 2.15 and 2.16, respectively. The range of the mentioned non-dimensional parameters covered by the present

TABLE 2.5: Summary of non-dimensional parameters covered by the experiments in Chapter 2

Propeller	*Fr*	$Re_f \times 10^5$	$Re_p \times 10^5$
Prop1	0.4 - 1.3	1.7 - 5.2	0.5 - 1.3
Prop2	0.8 - 1	3.3 - 3.9	0.8 - 1

experiments is summarized in Table 2.5. During the present experiments, the flow and propeller Reynolds number are greater than 3×10^3 and 7×10^4, respectively, in agreement with the threshold established by Verheij (1983) to avoid scale effects due to viscosity related to the flow along the propeller blades.

$$Fr = \frac{U_0}{\sqrt{gD_p}} \tag{2.14}$$

$$Re_f = \frac{U_0 D_p}{\nu} \tag{2.15}$$

$$Re_p = \frac{nL_m D_p}{\nu} \tag{2.16}$$

$$L_m = \beta D_p \pi [2N(1 - \frac{D_h}{D_p})]^{-1} \tag{2.17}$$

where:

U_0 = Efflux velocity (ms^{-1})
Fr = Froude Number (-)
Re_f = Reynolds Number of the flow (-)
Re_p = Reynolds Number of the propeller (-)
L_m = Characteristic length of the propeller (m)
D_p = Propeller Diameter (m)
D_h = Propeller hub Diameter (m)
N = Number of blades of the propeller (-)
n = Speed of rotation (rps)
β = Blade Area Ratio (-)

The horizontal Turbulence Intensity ($\sqrt{\overline{u'^2}}$), obtained with Eq. 2.11, shows maximum values at the outer jet layer (R = $0.4D_p$), as shown in Figure 2.9 for EV1 experiments. The same relation between $\sqrt{\overline{u'^2}}$ and U_0 is observed, regardless of the speed of rotation. In this area, the boundary between the jet flow and the ambient water is found, and higher values of turbulence intensity may be caused by the increased mixing and higher shear forces in the flow. This results are in good agreement with the expected behavior and literature (Lam et al., 2012), where higher values of TI were found both at the outer and inner jet layers through LDA measurements of the propeller jet velocity distribution.

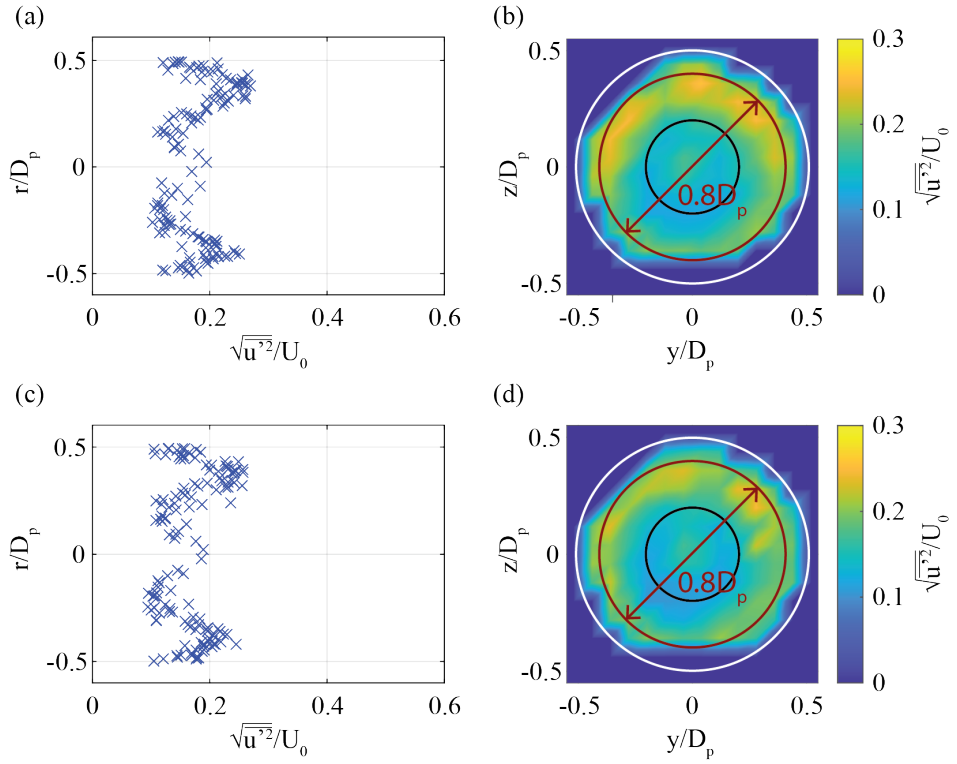

FIGURE 2.9: Horizontal TI distribution at the efflux plane (*Prop1*). (a), (c): Radial distribution of $\sqrt{\overline{u'^2}}/U_0$ at 250 rpm and 300 rpm respectively. (b), (d): 2D colormaps of $\sqrt{\overline{u'^2}}/U_0$ at 250rpm and 300rpm respectively. The red circumference shows the radial location of the maximum TI, while the white and black circumferences show the propeller diameter and the location of maximum mean velocities.

To provide further insight to the punctual velocity measurements, the energy spectra analysis is presented herein, through the Power Spectral Density (PSD) of each measurement within a radial distance in the range of $0.15D_p < R_m < 0.3D_p$. This range is used to include the positions where the maximum time-averaged velocity across the propeller plane is measured. In Figure 2.10 (a) and (b) some examples of the PSD of the signal are shown. In the PSD of both experiments, energy peaks at the blade-passing frequency (16.64 Hz or 20 Hz), the propeller axis frequency (4.16 Hz and 5 Hz) and at its second harmonic (8.32 Hz and 10 Hz) are found in case of 250 rpm or 300 rpm respectively. This behavior is observed mostly in the inner jet measurements, where the jet flow is not influenced by the ambient water, but this is not observed in the outer side of the jet (at radial distance close to $0.4D_p$). In the Appendix A.3, examples of the PSD for the measured flow velocity in the inner jet are plotted, along with the radial position (R_m) where they were measured.

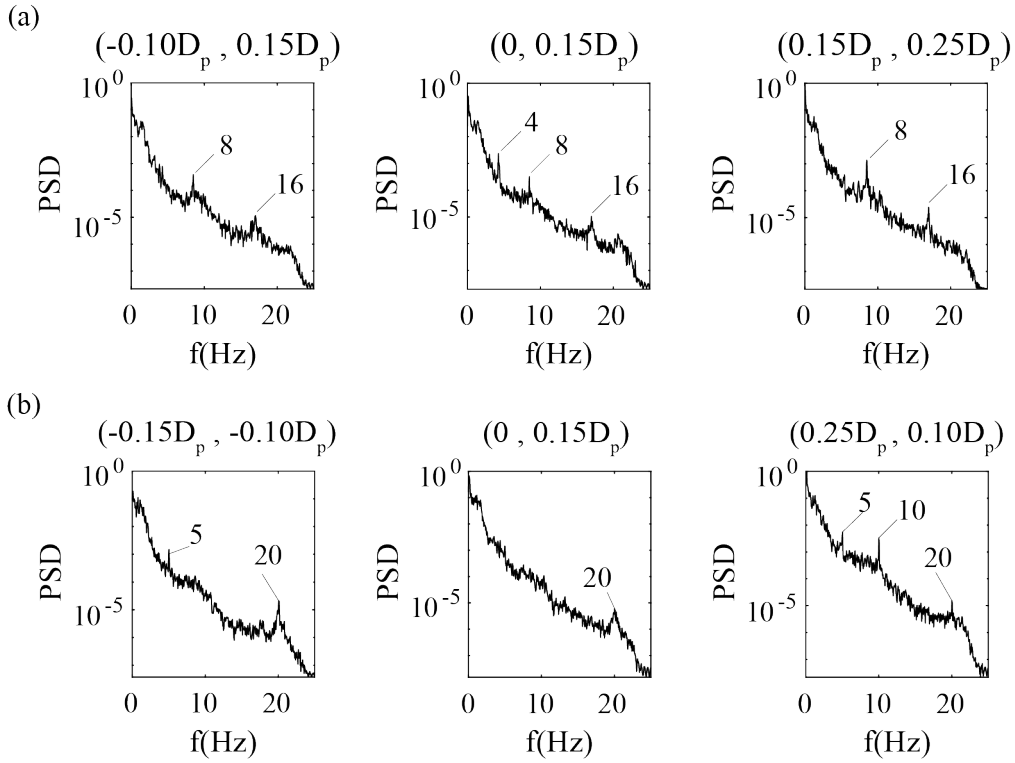

FIGURE 2.10: PSD of 6 measurement points in the inner propeller jet during EV1 experiments. The position (y, z) of the measurement is shown in each case. (a) Measurements at 250rpm; (b) Measurements at 300rpm. Frequencies of interest are indicated in each figure.

2.3.2 Average shear stress over the shear plate

The present section shows the results obtained from direct measurements of bed shear stress with the previously described shear plate in section 2.2.2. All the measurements included in this section were made during 80 seconds time-series, filtered with a Butterworth filter (Butterworth et al., 1930) of order 7 and a cut-off frequency of 15 Hz. The decision to use this filter was taken after the analysis of a long measurement (20 minutes) at 1 of the 4 scenarios considered in the presented experiments. The analysis of the long measurement is shown in the Appendix B.

A total of 4 different situations have been analyzed through experiments (BSS1 to BSS4) on bed shear stress induced by the jet flow of a propeller model (*Prop1*) at 5 different speeds of rotation, as summarized in Table 2.2. Two repetitions of each measurement were performed, except in case of BSS1 experiment, in which 6 repetitions of the measurement at different days were taken. This number of repetitions was chosen to approximate the variability that should be expected in case of 80 seconds time-averaged measurements. During the analysis, some of the time-series were discarded due to the lack of quality in the obtained signal. Unfortunately, in

those cases, repeatability cannot be evaluated, therefore some experiments are presented only with one measurement.

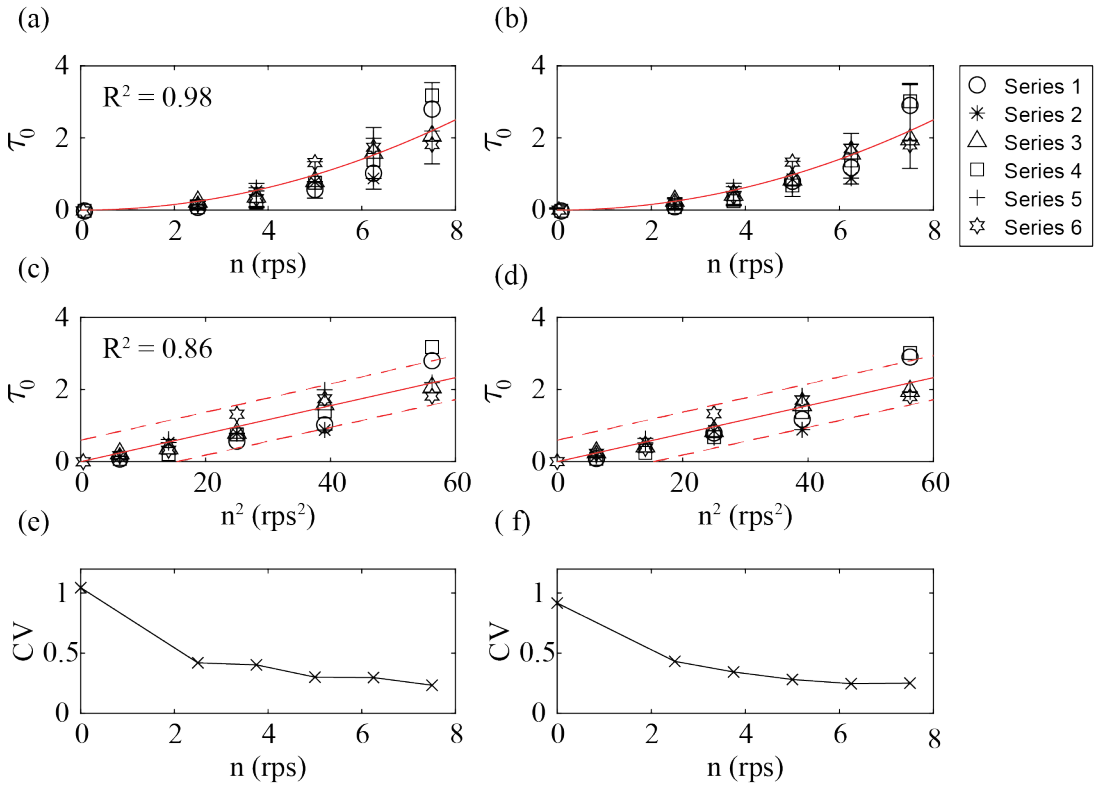

FIGURE 2.11: Figures (a) and (b) show the time-averaged bed shear stress (BSS) over the shear plate, measured 6 times by the strain gauges SG1 and SG2, respectively. The BSS is plotted as a function of the propeller speed of rotation (rps). The error bars represent twice the standard deviation of the time-averaged bed shear stresses, and the red line show the fitted power model. Figures (c) and (d) show the same measurements as a function of the squared of the speed of rotation. The dashed-lines show the 95% prediction interval of the linear model. In figures (e) and (f), the CV at each speed of rotation is shown.

According to the literature (Velzen et al., 2016), and following the assumption when applying Eq. 2.13, the relation between the U_0 of the propeller jet and the speed of rotation is linear for a unique propeller. Also, according to the German and Dutch methods in PIANC (2015), the maximum expected velocity at bed (U_b) in case of low bed clearance is linear with U_0, and therefore with the speed of rotation. Given the latter, the same functional relation must be expected between the maximum flow velocity at bed and the induced shear stress as between the propeller speed of rotation and the induced shear stress. Thus, the time-averaged shear stress is presented in Figure 2.11 as a function of the propeller speed of rotation, in case of experiment BSS1. In Figures 2.11 (a) and (b), a power model ($y = Kx^2$) is fitted to the average shear stress of the 6 repetitions, yielding a value of R^2 = 0.98 and K = 0.0391

≈ 0.04. In Figures 2.11 (c) and (d), a linear model ($y = Kx$) is fitted to the whole set of data yielding an R^2 of 0.86 and K = 0.0389 ≈ 0.04. At low speed of rotation, the dispersion of the data is larger (CV $\approx$ 40%) than at higher speeds of rotation (from 5 rps), where it is kept constant at lower values (CV $\approx$ 20%). The variability within each measurement is not shown in this section, but analyzed together with the long measurement in Appendix B. The variability of the instantaneous shear stress is an important parameter that needs to be considered, especially in case of three dimensional turbulent flows such as the propeller jet, but at the time is out of the scope of the analysis in this section. From the experimental results, one may assume that the variation coefficient (CV) can reach values close to the 100% of the time-averaged bed shear stress (see Figure B.3 (c), (d)). Moreover, the obtained relation between the time-averaged bed shear stress and the standard deviation of the measurement is linear at each experimental condition (see Figures B.3, B.4, B.5, B.6).

The rest of the experiments (BSS2, BSS3 and BSS4) show a fairly similar behavior compared to BSS1. A power model is adjusted to the mean value of the two repetitions (Serie 1 and Serie 2) of each measurement, yielding good results in all cases. In Figure 2.12 (a) to (f) , the data and the adjustments are shown, together with the determination coefficient obtained in each fit. The proportionality coefficients, K, obtained after fitting each model in the data of BSS2, BSS3 and BSS4 experiments are 0.068, 0.051 and 0.069, respectively. A considerable difference is observed between the experiments BSS2 and BSS4 (lower bed clearance and higher coefficients, $K \approx 0.07$) and the experiments BSS1 and BSS3 (higher bed clearance and lower coefficients, $K \approx 0.05$ and $K \approx 0.04$) at any distance to the plate, in agreement with the expected, since the loads induced by propellers with lower bed clearance must be higher. In Figure 2.12 (g), (h), the total error, computed as the difference between the two repetitions, relative to the mean value is plotted for each measurement. Results are in range with the variation coefficients obtained in case of BSS1 for 6 repetitions, also showing that the uncertainty is clearly reduced at higher stresses. Moreover, in BSS3, with the higher clearance and longer distance to the plate, the variation between the measurements is negligible.

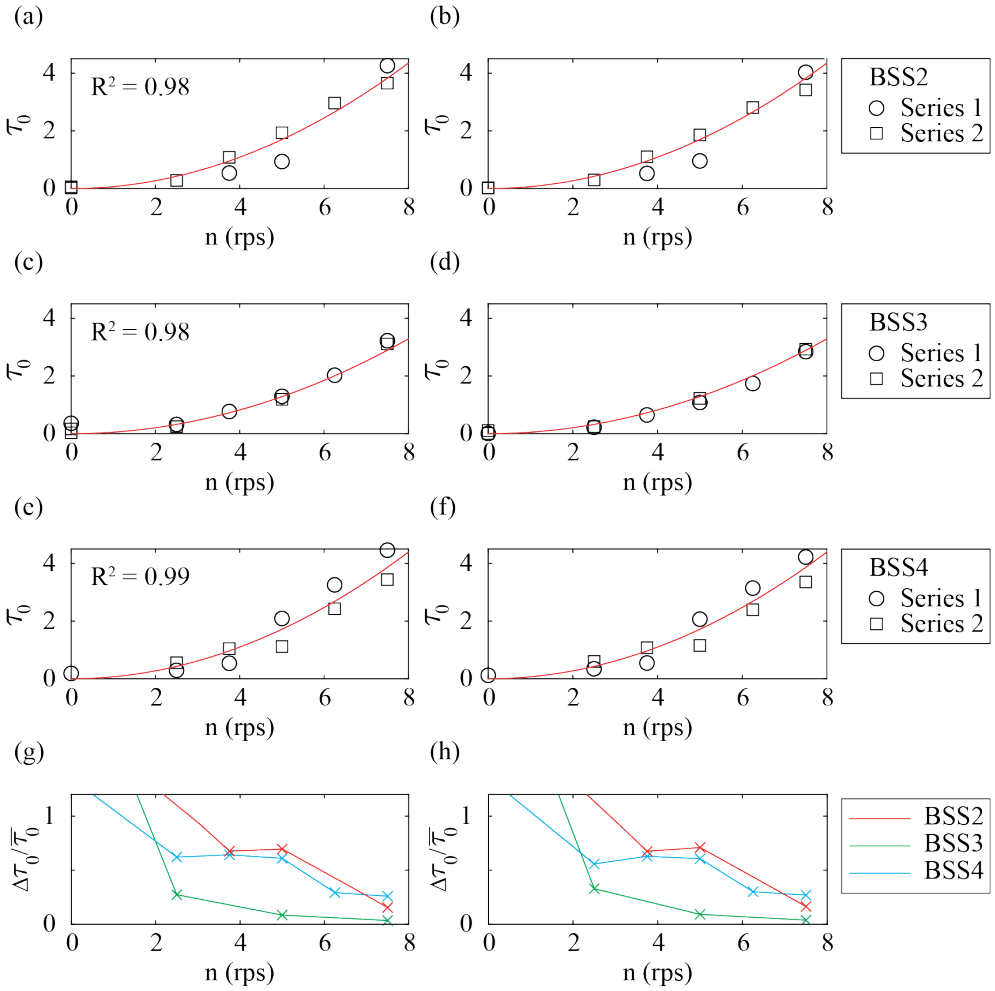

FIGURE 2.12: Figures (a) to (f) show the time-averaged bed shear stress measured by the shear plate at each experimental condition. The power model is adjusted to the mean value of the repetitions. Figures (g) and (h) show the absolute error of the two repetitions relative to the mean value.

2.3.3 Adjustment of a friction coefficient from U_0 and shear stress measurements

Estimating the bed shear stress in a particular scenario is considered to be a benchmark to assess the scour potential of a ship with restricted bed clearance. Once the shear stress is known, the stability of the sediment bed can be assessed by direct comparison of the computed Shields number and the critical Shields number of the bottom material. It is known, however, that the instantaneous force on a bed particle varies through time, as the turbulent velocity component does. Still, for steady flow, the mean bed shear stress is usually related to the square of the free stream velocity, Eq. 2.18, through an empirical friction coefficient (C_f). In Blaauw and Kaa (1978), the authors proposed a friction coefficient between 0.06 and 0.11 to obtain the mean bed shear stress due to propeller jets for the first time, using in this case the velocity at bed, obtained with Eq. 2.20. The measurements analyzed in Section 2.3.2 show

that the time-averaged bed shear stress can be also estimated as a function of the propeller speed of rotation, therefore as a function of the efflux velocity, with different adjustments depending on the experimental conditions. Since the differences in the proportionality coefficients obtained in the experiments depend on the bed clearance, the use of the bottom velocity to adjust Eq. 2.18 may be reasonable, because it is also a function of the bed clearance. Several expressions exist in literature to obtain the maximum velocity at bed due to propeller jets, as a function of the efflux velocity and the bed clearance. Most commonly, the Dutch and German methods (Eq. 2.19), are used to simply estimate this parameter applying different coefficients depending on the boundary conditions (see, for instance, PIANC (2015)). In Maynord (2000), the use of the maximum velocity at bed, calculated with Eq. 2.19 (German method), is recommended to estimate the peak bed shear stress of a passing ship. In his work, a series of experiments are carried out to directly measure the bed shear stress due to propeller jets, after which C_f is proposed as a function of the diameter to bed clearance ratio ($C_f = 0.01(\frac{C_h}{D_p})^{-1}$).

$$\tau = \rho U_* = \frac{1}{2} C_f \rho U_x^2 \tag{2.18}$$

$$U_b = C_1 U_0 (\frac{C_h}{D_p})^{-1} \tag{2.19}$$

$$U_{x,r} = U_0 \frac{1}{2c} \frac{D_o}{x} e^{-\frac{1}{2c^2}\frac{r^2}{x^2}} \tag{2.20}$$

where:

c = 0.19 in case of non-ducted propellers
C_h = Bed clearance (m)
C_1 = 0.216 for Dutch method and 0.42 for German Method
C_f = Friction coefficient (-)
D_p = Propeller diameter (m)
D_o = Propeller diameter at the contraction plane (m)
r = Radial distance from the propeller axis (m)
U_* = Shear velocity (ms^{-1})
U_x = Axial velocity of the jet flow in a field point (ms^{-1})
U_b = Maximum velocity at bed (ms^{-1})
U_0 = Efflux velocity (ms^{-1})
$U_{x,r}$ = Axial velocity at any position across the velocity profile (ms^{-1})
x = Axial distance downstream the propeller plane (m)
τ = Bottom shear stress (Nm^{-2})

Using Eqs. 2.19 and 2.20 with the current experimental conditions, both the maximum value of the velocity at bed and the mean velocity distribution are obtained at several distances from the propeller plane, coinciding with the distances where the shear plate was located during the experiments (see Table 2.2). The theoretical distributions are plotted in Figure 2.13. Note that Eq. 2.20 is only valid for the Zone of

Established Flow (ZEF), which is assumed to begin at $2D_p < X < 3D_p$, according to Stewart (1992), Hamill and Kee (2016), and Hong et al. (2016). The maximum values of the depth velocity distribution at the bottom level ($C_h = 0.7D_p$ and $C_h = 1D_p$) obtained with Eq. 2.20 are coincident with the absolute maximum velocities obtained with Eq. 2.19 at the horizontal distances where the shear plate was located during the experiments. It must be noted that Eq. 2.20 does not take the bottom effects over the mean velocity distribution into consideration. Since the measured bed shear stresses during experimental runs BSS3 and BSS4 (plate located between $3.7D_p$ and $5.7D_p$) are slightly higher than the ones in BSS1 and BSS2, the former are chosen to relate the velocity to the maximum measured shear stresses. The distance to the shear plate in BSS3 and BSS4 is also in well agreement with the expected location of maximum velocity at bed, $0.12 < C_h/x < 0.22$ according to PIANC (2015), after the research performed by Verheij (1983).

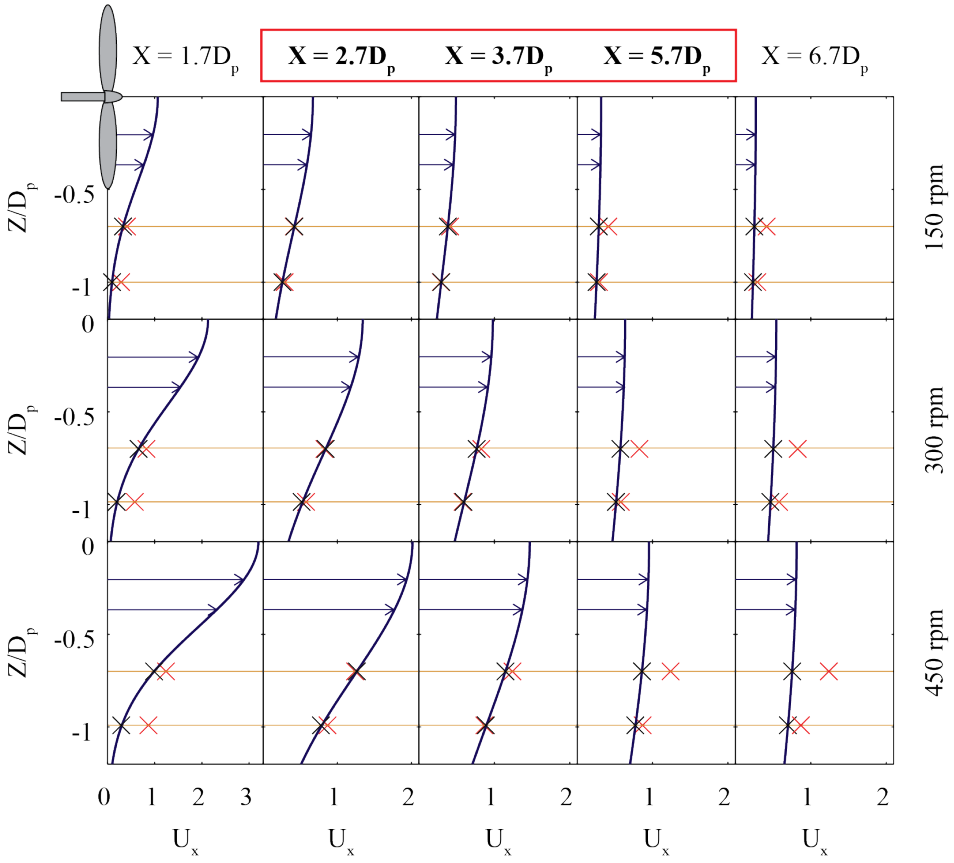

FIGURE 2.13: Theoretical velocity distribution at each distance from the propeller plane in case of 150, 300 and 450 rpm. The distances in bold, within the red box, show the horizontal distances to the shear plate during the experiments. The cross marks over the velocity profile show the velocity magnitude at two depths, coinciding with the experimental bed clearance distances ($C_h = 0.7D_p$ and $C_h = 1D_p$). The red cross marks show the theoretical maximum velocity at the same depths, regardless of the axial distance. The horizontal brown lines show the location of the bottom at each experiment.

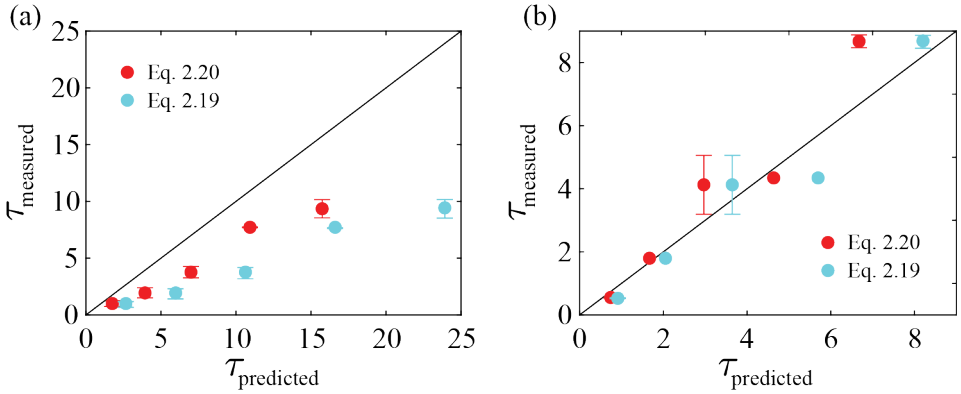

FIGURE 2.14: Predicted against measured shear stress using Maynord's model with both Eqs. 2.20 and 2.19. (a) experiments BSS4; (b) experiments BSS3. The error bars show the absolute error between the two repetitions at each experiment.

In Maynord (2000), it is recommended not to apply the proposed model in very low bed clearance conditions, with a threshold of $D_p/C_h = 1.2$ arguing a much better performance at lower values. In the experiments performed, BSS4 is above that threshold ($D_p/C_h = 1.43$), while BSS3 is in range. In this Section, an effort is made to compare the data obtained in the presented experiments with the proposed model in Maynord (2000). Firstly, the experimental data is filtered with moving average filter with a window length equal to the sampling frequency, thus obtaining filtered data at 1 Hz as in Maynord (2000). Then, the friction coefficient, explicitly proposed for hydraulically smooth beds in Maynord (2000), is adapted to the present experiments over a rough bed according to the expression proposed by the author ($C_{fr}/C_{fs} = 7.87 d_{50}^{0.18}$). To obtain the peak bed shear stress (τ_{peak}) from the experiments in this work, the time-averaged shear stress plus 3 standard deviations is used. The model is therefore applied to the experimental data to prove the agreement with the obtained results, as shown in Figure 2.14. Good agreement is found between the predicted and measured results in case of experiment BSS3, especially if Eq. 2.19 is used to obtain the bottom velocity. However, the predicted shear stress in case of BSS4 yields remarkable disagreements with the experimental results, being the latter largely overestimated. Note that the measured bed shear stress is computed as the mean value of the two repetitions performed at each experiment (Series 1 and Series 2 in 2.3.2).

Willing to fill the gap yielded by Maynord (2000) to estimate the propeller induced bottom shear stress in low bed clearance scenarios (less than $1D_p$), the shear stress is proposed as a function of $\frac{C_h}{D_p}$, U_0 and C_f. In this case, time-averaged bed shear stress values are used, since the validation of the instrument has been only performed for time-averaged values so far. The use of the velocity at the bottom is avoided, due to the existence of several formulations, each one yielding different results. However, reliable measurements on near bed velocity would be desirable to

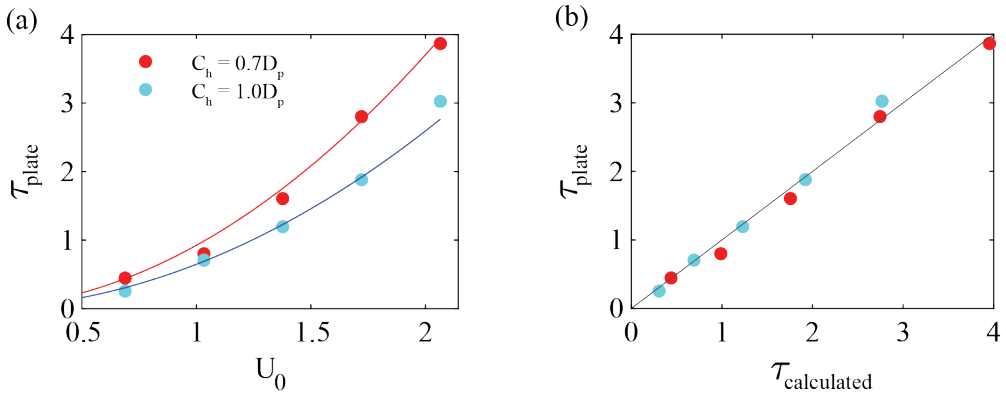

FIGURE 2.15: (a) Fitted model to the experimental data of bed shear stress; (b) Agreement between predicted and measured bed shear stress.

relate the measured bed shear stress with the local flow conditions above the sediment bed. Still, since linearity is expected between U_0 and time-averaged values of U_b, the adjustment must exist for any of them, although difference between the coefficients.

The model is fitted by means of a least squares regression, by optimizing the coefficients C_f and a in Eq. 2.21. U_0 is obtained with Eq. 2.13 at the speeds of rotation of the experiments BSS3 and BSS4, with the K_T previously obtained in section 2.2.1.

$$\tau = \frac{1}{2}\rho C_f (\frac{C_h}{D_p})^a U_0^2 \tag{2.21}$$

Although the best fit results in $C_f = 0.0014$, $a = -0.81$ and $R^2 = 0.992$, the adjustment is still in high agreement to the experimental data if the power coefficient a is set to -1 and C_f is expressed as a function of $(\frac{C_h}{D_p})^{-1}$, as shown in Eq. 2.22, where $C_f = 0.0013(\frac{C_h}{D_p})^{-1}$.

$$\tau = \frac{1}{2}\rho C_f U_0^2 \tag{2.22}$$

In Figure 2.15, the results are shown according to Eq. 2.22, yielding $R^2 = 0.989$. This is proposed as a reasonable option to estimate the induced shear stress in case the propeller is operating in low bed clearance environments.

2.4 Discussion

The efflux velocity, U_0, has been traditionally considered a fundamental parameter in the study of the propeller jet velocity distribution and induced scour, since it is used as a scaling velocity to obtain the jet velocity distribution downstream the propeller plane and the induced velocities at bed (see Section 2.3.3). To minimize the

uncertainty associated to the calculation of the efflux velocity, the velocity field at the efflux plane was measured and the propeller thrust coefficient was obtained with Eq. 2.13. Although efflux plane is a convenient term to define the horizontal distance to the plane containing U_0, some uncertainty may be derived from the assumption of the efflux plane location. One may argue that the maximum axial velocity is located at the contraction plane, in accordance with Bernoulli. In this regard, BAW (2010) recommends $0.5D_p$ as the horizontal distance to the contraction plane, therefore to the maximum axial velocity plane. Recently, Hsieh et al. (2013) confirmed that the location of the contraction plane can be safely assumed to be located at an horizontal distance of $0.5D_p$ downstream the propeller plane by PIV measurements.

In the present work, consistent results are obtained from the velocity measurements with the pitot-static tube, which allowed to perform a dense grid of velocity measurements within the efflux plane, with a fairly simple and adaptable device. The consistency in the turbulence intensity measurements and in the spectral density distributions confirms the suitability of the instrument to obtain velocity measurements close to the propeller face if U_0 is needed. Although relevant information regarding the tangential and radial component of the jet flow are neglected using the pitot-static tube, enough information is obtained to fit the scope of the experiments. This is therefore proposed as a suitable instrument to validate the expressions in literature to any future work with similar propellers.

Once the U_0 is characterized, the velocity distribution downstream the propeller face can be estimated. The decay of the mean axial velocity has been studied by several authors (e.g. Fuehrer and Romisch (1977), Blaauw and Kaa (1978), Stewart (1992), and Hamill and Kee (2016)), all of them proposing empirical equations to obtain the maximum axial velocity at any distance from propeller plane. Under the assumption of axisymmetric flow and a dynamically similar diffusion process, once the axial velocity is known, the velocity distribution can be characterized by a Gaussian distribution function of the form of Eq. 2.20. Recent research performed by Hong, Yeh, and Chiew (2020) proposed an analytic method to obtain the axial velocity magnitude and distribution using the point-source method of Pani and Dash (1983). In the present work, the equation proposed by Blaauw and Kaa (1978) is used to estimate the velocity distribution downstream the propeller face, at the positions of the shear plate. The maximum velocities at the bottom depth are located over the shear plate positions in the experiments ($2.7D_p < X_{plate} < 5.7D_p$, see Table 2.2). Since BSS3 and BSS4 experiments (plate located at $3.7D_p < X_{plate} < 5.7D_p$) yielded slightly higher mean bed shear stresses than BSS1 and BSS2 experiments, the former are used to relate the maximum bed shear stress with the flow velocity. Eq. 2.19 is used to obtain the maximum bottom velocities, as proposed in Maynord (2000), to validate the model with the performed measurements. The method proposed by Maynord (2000), to estimate peak bed shear stresses, yielded good agreement

with the experimental results in case of BSS4 experiments, where $D_p/C_h = 1$ is in range with the recommendations by the author. In case of BSS3 experiments, where $D_p/C_h > 1.2$, out of the recommended range, the experimental results are largely overestimated.

Since no other models exist in literature to compute the bed shear stress in the present conditions, an adjustment of the experimental data is proposed to obtain the mean bed shear stress due to propellers in low bed clearance situations ($D_p/C_h > 1.2$). No experimental measurements on bed velocity were available to validate any of the aforementioned methods, therefore the measured bed shear stresses are related with the U_0 through the empirical coefficient C_f. In this case, the C_f is inversely related to the bed clearance (see Eq. 2.22). Still, accurate near-bed velocity measurements are considered highly relevant to this research, and must be the focus of further work. The measurement of velocity profiles over the shear plate, including near-bed velocity measurements, would provide interesting insights to the results, allowing the validation of the shear plate measurements with indirect computation of bed shear stress. Several methods to compute the bed shear stress from velocity measurements close near the horizontal bed are mentioned in the introductory section of this Chapter.

Experience in literature can be used to qualitatively compare the performed experiments with the expected velocity measurements over the shear plate. Recently, Wei, Chiew, and Cheng (2020a) performed an experimental work with PIV to measure the characteristics of the propeller jet constrained by an horizontal boundary, obtaining clear results on the spatial distribution of the bed shear stresses. This research is in line with Hsieh, Low, and Chiew (2016), Wei, Chiew, and Hsieh (2017), and Guan et al. (2019), where the same system was used to obtain highly spatial resolved velocity measurements that allowed to obtain the linear velocity gradient in the viscous sub-layer, therefore the shear stress. In their work, shear stresses between 0.2 and 0.3 Nm^{-2} are obtained for a small scale propeller of $D_p = 7.5$ cm with $U_0 = 0.424$ ms^{-1}. Since the measurements are performed over a hydraulically smooth surface and at $C_h = 1D_p$, Maynord's equation is directly comparable to their results, computing the U_b with Eq. 2.19. In this conditions, a bed shear stress of $\tau \approx 0.2Nm^{-2}$ is obtained, in range with the results in Wei, Chiew, and Cheng (2020a). The applicability of Maynord's equation in the present work is also proven in case of $C_h = 1D_p$ (see Figure 2.14 (b)). According to Wei, Chiew, and Cheng (2020a), the maximum shear stress in streamwise direction in case of a free propeller at $C_h = 1D_p$ is found at a distance x = $4.3D_p$, and centered in the propeller axis. In Wei, Chiew, and Hsieh (2017), for the same conditions and propeller, the impingement region can be located between 1 and 2 D_p, while the wall jet is formed between 3 and 4 D_p. In case of a propeller with $C_h = 0.5D_p$, a wall jet exists already at a distance x = $2D_p$. Considering the former, the measurements in this work can be located

at the wall-jet region, while the maximum shear stresses can be located at the center of the shear plate, in case of BSS3 and BSS4 experiments, which is the area of interest.

Although it is widely accepted that the induced shear stress is the driving force that cause bed scour, no systematic empirical research in bed shear stress induced by propeller jets has been published so far. Nevertheless, some attempts have been made in the past to propose empirical friction coefficients to estimate the bottom shear stress in case of propeller jet flow with different methods (Wei, Chiew, and Hsieh, 2017; Hong et al., 2016; Maynord, 2000; Blaauw and Kaa, 1978). Because of that, a reliable estimation of the shear forces over the sediment bed is needed to advise the potential damage that a ship may cause when navigating in low bed clearance environments, including scour, high sediment concentration in the water column or re-suspension of contaminated sediment. With the proposed model in Eq. 2.21, an average value of bed shear stress is obtained as a function of U_0 and the bed clearance. It is known, however, that peak values of shear stress are highly relevant to the incipient motion, resuspension and transport. The analysis performed in Appendix B with the long-series and the 6 repetitions of BSS1 yielded CV of 100%, which indicates a highly fluctuating phenomenon that may cause considerably high peaks of pressure over the individual grains. The other experiments yielded lower variability, with CV between 70% and 85%. This is, again, once averaging the forces over the 0.1 m^2 area. Still, uncertainty due to the estimation of the variability of the measurements cannot be assessed at this point yet. As mentioned previously, independent validation of the measurements is still needed to provide a reliable range of shear stress fluctuations under the present experimental conditions. Because of that, further experimental work is necessary to evaluate the fluctuations of the measured bed shear stress during longer time-series.

The development of the instrument is considered a benchmark to future research, with different bottom roughness to study the influence of this parameter in the measured shear stress. Different roughness must be tested under propeller jet at the same conditions of the herein presented experiments to obtain useful results that may have application at field to design bottom protections at harbors and slope banks protections in navigable channels, in case of unconfined propeller jets. Experiments in the same conditions over hydraulically smooth bed are considered interesting to validate the expressions proposed in literature and already mentioned in this Section.

2.5 Concluding remarks

- The Pitot-static tube coupled to the differential pressure sensors is proved to be a simple and adaptable method to obtain the time-average velocity distribution along parallel planes to the propeller face.

- A shear plate has been developed and successfully tested at the LWI to obtain the time-averaged bed shear stress caused by a propeller model over a roughed horizontal bottom for the first time.
- Results are in accordance with the expected behavior, being the shear stress a function of the squared efflux velocity and the friction coefficient.
- The model proposed in Maynord (2000) show good agreement with the experimental results in one of the experimental conditions ($C_h = 1D_p$), but no satisfactory results are obtained by this method at lower bed clearance distance.
- A new empirical model is proposed to obtain the bed shear stress due to unconfined propeller jets over roughed beds in case of low bed clearance conditions.

Chapter 3

Local scour due to twin-propeller confined jet

3.1 Introduction

The use of marine propellers causes any vessel navigating or maneuvering in a harbor to induce erosion over the seabed when the bed clearance is not large enough. The high-speed wash coming out of the propeller eventually reaches the seabed, either due to its free expansion or the interaction with a port structure such as a berthing quay. Later, the sediment is resuspended and transported, thus leading to a scour hole. The magnitude of the scour hole can be important and therefore cause several problems if not noticed and managed in due time. Structural stability of the marine structures and accumulation of sediment in navigable channels, therefore reducing its operational draft, are two of the main problems arisen due to ship propellers induced scour. References of this well documented problem are found in several bedside books in this topic, such as Gaythwaite (2004), Hoffmans and Verheij (2021), Whitehouse (1998), and Sumer and Fredsøe (2002).

The study of the propeller induced erosion has been traditionally performed experimentally in physical models. The propeller jet properties and their effects over the sediment bed have been of importance during the past and recent years. Lam et al. (2011) published a literature review on the experimental studies on propeller jets during the last decades, showing the different empirical and semi-empirical expressions developed to characterize the propeller jet, mostly focused on local scour studies. They collected the different methods to obtain the efflux velocity (U_0) parameter, the decay in the axial velocity with the axial distance, or the velocity at the seabed as a function of the efflux velocity. More recently, Wei, Chiew, and Cheng (2020b) published an exhaustive review of the propeller induced scour recent and past research, including both the local scour research performed at physical models and recent studies in flow behavior during the scour process performed by PIV. Traditionally, two main research lines have been followed in propeller induced local scour: unconfined scour and confined scour. The former assumes the free expanding of the propeller jet flow while the latter considers the interaction of the jet flow

with port structures (closed or open quays). Between them, research in scour due to confined propeller jets have received much less attention, and not many articles are found in literature about the topic. In case of confinement by a closed quay wall, only Hamill, Johnston, and Stewart (1999) and Cui et al. (2020b) proposed an expression to determine the expected scour depth due to single and twin propeller jets, respectively.

Besides the experimental research in physical models, several studies have been performed in-situ to validate all the empirical or semi-empirical equations coming out from the laboratory. The applicability of the laboratory expressions is discussed, for instance, in Roubos, Blockland, and Van Der Plas (2014). In Mujal-Colilles et al. (2017b), bathymetries of the harbour basin are used to validate some of the equations existing in guidelines using real vessel and maneuver data as input to the models. Blokland and Smedes (1996) proposed one of the most used methods to analytically estimate the propeller induced velocity at seabed from field tests too. Abramowicz-Gerigk et al. (2018) studied the bow thrusters induced currents by large ships and successfully test the expressions proposed in PIANC (2015) for the most common ferry-type vessels at Gdynia port.

The last years have witnessed the growing trend in numerical studies in all branches of fluid mechanics and sediment transport. Several numerical studies have been performed in propeller jet modeling over the last two decades. The earlier references are included in Carlton (2012), although a considerable number of more recent articles, mostly focused on propeller design, noise reduction, cavitation, etc., have been published in this field (Ahmed, Croaker, and Doolan, 2020; Sun et al., 2018; Usta and Korkut, 2018). Focusing on the flow evolution of a twin propeller, Cui et al. (2020a) recently published a combination of numerical and experimental research on the axial evolution of the twin propeller jet velocity and turbulence intensity. More recently, Guarnieri et al. (2021) studied the erosion effects of the large commercial vessels over the sediment of the port of Genoa through a numerical study, considering the propellers position as a movable flow input, and studying the effects over the sediment with the hydrodynamics and mud transport models MIKE 3 FM.

In reality, multiple types of propellers and ships are found, meaning that it is difficult to generalize when analyzing the effects of the propeller jets. However, some types of ships are commonly associated with a specific propeller type. For instance, ferry and RO-RO ships are commonly associated with stern twin propellers, combined with one or two bow thrusters to maneuver. These are one of the most common ships transiting Mediterranean ports (Marzano et al., 2020) and are object of the present work. Depending on the port, the characteristics of the sediment can differ in orders of magnitude. Sediment has been traditionally a problem in scaled physical models, because of the impossibility to scale sediment if the geometrical

scale is too large. The use of several sediment sizes usually permits to account for a wide range of sediment types, although there is a need to validate any expression obtained at laboratory in field cases to study its applicability, since the magnitude of the scale effects are uncertain.

The present chapter presents an experimental study performed at the Laboratori d'Enginyeria Marítima (LIM), at the Universitat Politècnica de Catalunya (UPC-BarcelonaTECH), with a twin-propeller model in confined condition, i.e., near a vertical boundary. Typical RO-RO and ferry ships propellers are modeled in the presented set of experiments, aiming at studying their effects near the harbor structures, where they operate with daily basins. Mujal-Colilles et al. (2018) presented the initial set of experiments, and the present contribution increases the scenarios in pitch ratio and, more importantly, improving the measuring area by reaching to up to 0.05 m to the vertical wall, allowing the analysis of the local scour at the closest locations to the vertical wall. With the obtained results, a new empirical relationship between maneuvering conditions and scouring action is presented.

The current chapter is divided in the following sections: The description of the physical model and the experiments is provided in Section 3.2. The experimental results are presented in Section 3.3, focusing on the evolution of the morphology of the scour hole (Section 3.3.1), the evolution of the maximum scouring depth (Sections 3.3.2 and 3.3.3), the comparison with existing formulae in literature (Section 3.3.4) and the dimensional analysis to propose the new model (Section 3.3.5). Results are discussed in Section 3.4. Finally, conclusions of this work and recommendations for further research are provided in Section 4.6.

3.2 Experimental Setup

The following sections (3.2.1, 3.2.2 and 3.2.3) describe the physical model where the experiments were performed, the scaling considerations and the set of experiments performed at the model, respectively.

3.2.1 Physical model

The experiments presented in this chapter were conducted in a medium-scale water tank named *LaBassa*. *LaBassa* is a 12.5 x 4.6 x 2.5 m concrete basin with moving-bed of uniform sand equipped with two different mobile bridges. The mobile bridges allow longitudinal movement along the tank length so that the longitudinal position is adjustable. A twin-propeller model and a pair of echo-sounders are installed on each bridge. The first is fixed at the tank centre-line, while the last are moved transversely by a mechanical belt. During the present experiments, the twin propeller model was located in the propeller's bridge, in a position close enough to the

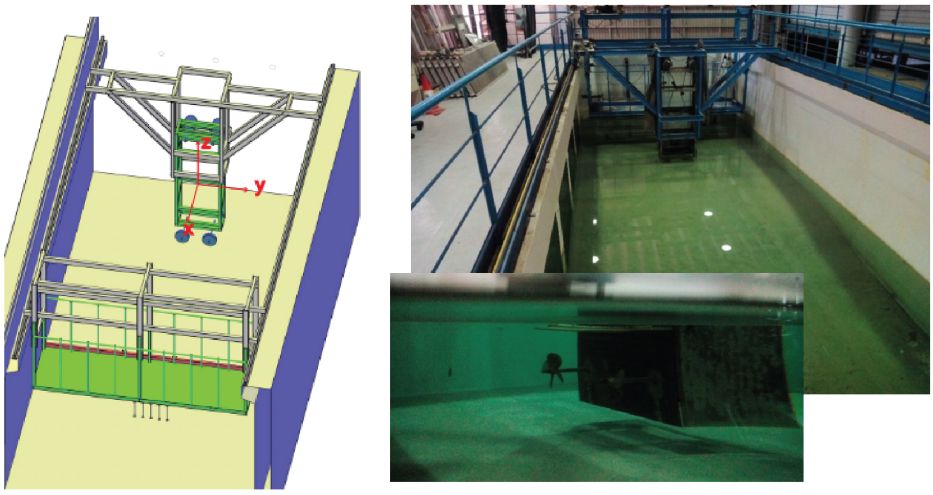

FIGURE 3.1: 3D and picture of *LaBassa* basin.

TABLE 3.1: Propeller model and sediment characteristics

Propeller diameter	D_p	0.25 m
Distance between axes	a_p	0.5 m
Propeller pitch ratio	p'	1.0
Blade Area Ratio (B.A.R)	β	0.75
Sediment diameter	d_{50}	0.250 mm
Sediment diameter	d_{90}	0.375 mm

vertical quay wall (in advance Front Wall (FW)) to ensure a confined flow condition. This set-up aims at studying the effects of a confined twin propeller jet over the sand bed near a vertical boundary. A 3D sketch in Figure 3.1 is included with a picture of the basin and the twin propeller system to the good guidance of the reader. In the present experiments, scour due to both forward (FWD) and backward (BWD) rotation of the twin propellers is studied by conducting two different sets of experiments in the same conditions: Forward (FWD) and Back & Forth (B & F). FWD experiments are performed with consecutive runs of forward rotation, while B & F experiments combine alternatively forward and backward rotation. The experiments are explained in detail in subsection 3.2.3. The main characteristics of the twin propeller model and the sediment used in the present experiments are summarized in Table 3.3. Note that the propeller model is the same propeller named *Prop2* in Chapter 2 of this dissertation.

3.2.2 Scaling of the experiment

The present model is scaled from typical RO-RO and RO-PAX vessels, with twin propellers diameter up to $D_p \approx 6$ m and a range of propellers speed of rotation between 90 and 140 rpm. These kind of ships usually operate with daily basins in most of

the Spanish Mediterranean ports with short sea shipping industry (Castells-Sanabra et al., 2021; Marzano et al., 2020). The twin propeller system, combined with transverse thrusters, allows these vessels to maneuver by their own means, i.e., with no need of tug assistance, in small harbor basins with low Under Keel Clearance (UKC) (defined as the 30% or less of the static draft of a ship according to IMO (1993)) and short distances to closed berthing quays. The nature of their commercial activity makes these ships to perform the same maneuvers every day at the same basins, thus having an accumulative effect over the sediment bed. These maneuvers have a total duration of around 25 minutes/maneuver with an accumulated time of 600 maneuvers per year.

To fulfill the similarity requirements, the Froude number (Fr) is used to scale the dynamic effects (see Eq. 2.14, in Chapter 2), considering also the Reynolds self-similarity theory by ensuring high enough Reynolds number ($Re > 10^5$) of the flow (see Eq. 2.15, in Chapter 2) and the propeller (see Eq. 2.16, in Chapter 2) to neglect scale effects due to viscosity. Moreover, the range of densimetric Froude numbers (Fr_d) (Eq. 3.1) covered by the presented experiments is higher than in many of the existing laboratory studies in propeller induced scour, where a considerably lower range ($5 < Fr_d < 15$) is usually found (Tan and Yüksel, 2018; Hong, Chiew, and Cheng, 2013; Cui et al., 2019; Cui et al., 2020c; Hamill, 1987). However, scale effects due to the sediment size must be expected since the densimetric Froude number at prototype situation may reach $Fr_d \approx 170$ in case of big ships over fine sand sediment (Mujal-Colilles et al., 2017b). Table 3.2 summarizes the range of non-dimensional parameter values covered by the present experiments, according to the results yielded by Eqs. 2.14, 2.16, 2.15, 2.17 and 3.1.

$$Fr_d = \frac{U_0}{\sqrt{g d_{50}(\frac{\rho_s}{\rho_w} - 1)}} \tag{3.1}$$

TABLE 3.2: Summary of non-dimensional parameters

Fr	$Re_f \times 10^5$	$Re_p \times 10^5$	Fr_d
1.01-1.34	3.94-5.26	1 - 1.33	23-31

3.2.3 Set of experiments

To study the scouring effects of the twin propellers nearby a vertical wall, a set of 24 experiments in confined scour is presented, as summarized in Table 3.3. The experimental conditions are included in the table and shown in the sketch in Figure 3.2. The experiments covered 2 horizontal distances to the FW, or wall clearance (X_w), and 2 distances from the propeller axis to the sand bed, or bed clearance (C_h) at 3 propeller speeds of rotation (n). In Figure 3.2, the dashed lines show a characteristic

ship according to the geometric scale used in these experiments ($\lambda = 1/25$). The grey structure in the upstream part of the propellers was covered by a solid steel plate, trying to reproduce the effects of a ship hull with a large block coefficient, such as RO-RO or RO-PAX ships.

TABLE 3.3: Summary of experiments

Regime	$\mathbf{X}_w$	$\mathbf{C}_h$	**n (rpm)**	**time (s)**	**exp #**
B & F	X_w^{min}	C_h^{min}	300	1800	1
			350	1800	2
			400	3600	3
		C_h^{max}	300	1800	4
			350	1800	5
			400	1800	6
	X_w^{max}	C_h^{min}	300	3600	7
			350	3600	8
			400	3600	9
		C_h^{max}	300	1800	10
			350	1800	11
			400	1800	12
FWD	X_w^{min}	C_h^{min}	300	1800	13
			350	1800	14
			400	3600	15
		C_h^{max}	300	1800	16
			350	1800	17
			400	1800	18
	X_w^{max}	C_h^{min}	300	1800	19
			350	1800	20
			400	1800	21
		C_h^{max}	300	1800	22
			350	1800	23
			400	1800	24

During each experiment, the propellers were started and stopped every 5 minutes and the whole measuring area in Figure 3.2 was scanned. The scanning was performed by 2 @ULTRALAB UWS1M Echo Sounders with accuracy of 1%. The echo-sounders were mounted nearby each other, separated by 7.5 cm, over the moving bridge. A total of 38 longitudinal profiles were obtained at 40Hz sampling rate, containing the bed elevation. Laser lectures of longitudinal and transversal distance to a reference point were obtained simultaneously allowing to locate every single

measure of the echosounder and generate a 3D grid of the measuring area. A three-dimensional surface was interpolated to the scattered data in the input vectors, obtained from the echo-sounders measurements. The interpolation was performed over a grid with transversal and longitudinal resolution of 1 cm by surface linear fitting. An example of a 3D grid is shown in Figure 3.3.

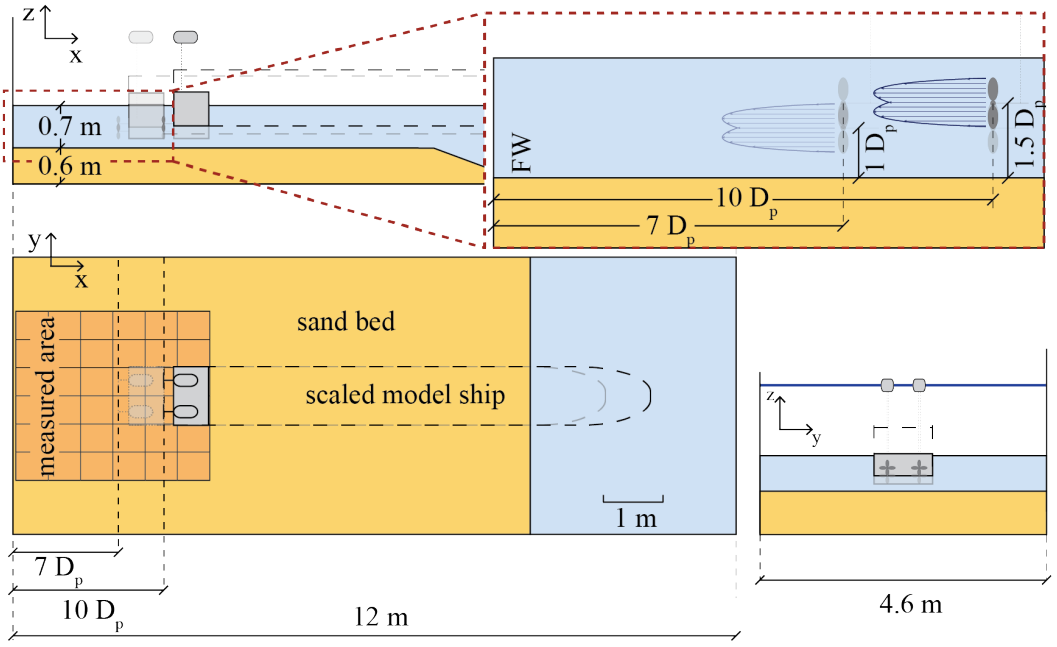

FIGURE 3.2: Sketch of *LaBassa* basin.

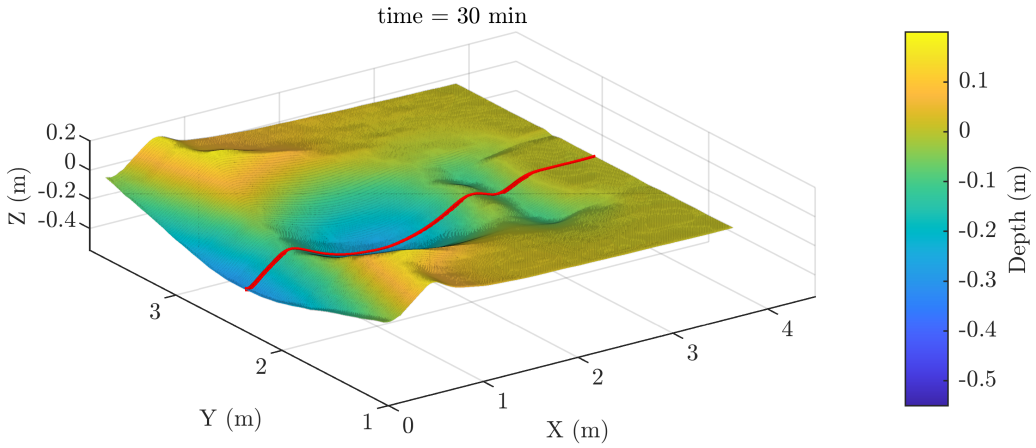

FIGURE 3.3: 3D Grid obtained at Exp # 21.

The total time for each experiment is set to 30 minutes (1800s), with some experiments being extended up to 60 minutes (3600s) to observe the further evolution of the scour profiles in different scenarios. The regime column in Table 3.3 states for the Forward (FWD) or Back & Forth (B & F) rotation, as mentioned in sub-section 3.2.1. In FWD regime, the propellers counterrotate (inward rotation) and the induced flow

is directed towards the FW during the total duration of the experiment. In B & F regime, the propellers rotation changes intermittently every 5 minutes from backward (BWD) to forward (FWD) rotation and the induced flow is directed first towards the unconfined part of the tank (BWD rotation), where the propeller supporting structure is located, and after to the FW (FWD rotation). The intention behind the B & F experiments is to compare the results from the traditional experiments, with steady FWD rotation, with the results obtained by combining BWD and FWD rotation. The last is considered to be a set-up closer to the reality of a ship near the wall, which berths and unberths by combining backward and forward propeller rotation (Guarnieri et al., 2021; Llull et al., 2020).

3.3 Results

Propeller induced scour is a three-dimensional process of sediment resuspension and transport that happens over a mobile sediment bed in response to the forcing by a single or multiple propeller jet. The time dependent scour process is described in this section for the case of a confined twin propeller system, to show the more important characteristics of the scour hole with special attention to the maximum depth. Particularly, the twin propeller confined scour process is described with contour plots focusing on the eroded areas and their evolution with time.

In twin propeller systems, jets are originated separately from each propeller and they are not initially influenced by one another. However, at a certain distance, which depends mainly on the distance between propeller axes and the propeller speed of rotation, both jets merge into a unique jet (Jiang et al., 2019; Mujal-Colilles et al., 2017a). The merged jet impinges the seabed and causes a developing scour hole (in advance HBH hole since it develops far from the front wall, in the Harbour Basin). This local scour hole is enlarged along the axial flow direction while expands symmetrically from its maximum depth longitudinal profile until it reaches the equilibrium. When rotating in the FWD direction, the influence of the front wall contributes to an important scouring process at its toe, downstream of the HBH hole. This second hole (in advance FWH hole) grows radially in the XY plane, from the twin propeller central axis–wall plane intersection. Both scour holes eventually merge, if equilibrium is not reached before, becoming a single main hole. The described process can be observed at 10 minutes time intervals in the contour plots showed in Figure 3.4 (a) and (b). In these cases, the mid speed of rotation scenario (350rpm) is chosen as the most representative of all the experiments. The contour plots corresponding to the whole set of experiments, at 5 minutes time intervals, are included in the Appendix D.1.

One of the most relevant features of all the experiments analyzed is that C_h^{min} cases induce a deeper HBH hole than C_h^{max} ones, while contrarily, the latter yields a

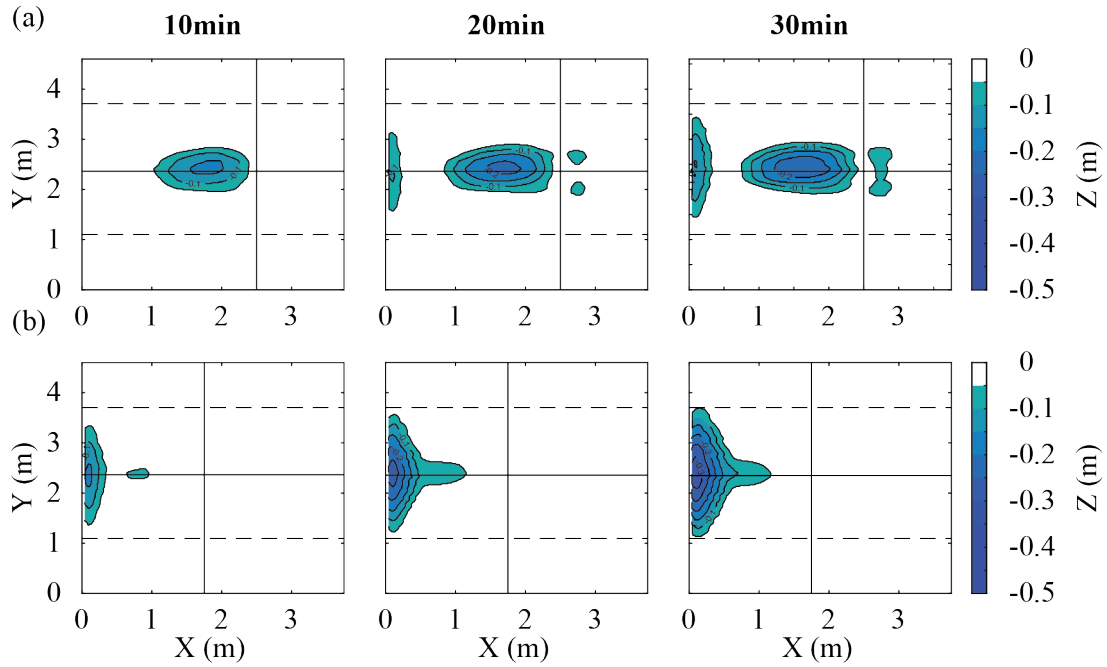

FIGURE 3.4: 2D contours of the plain view. (a) Exp # 20: C_h^{min}, X_w^{max}, FWD regime, 350rpm; (b) Exp # 17: C_h^{max}, X_w^{min}, FWD regime, 350rpm. The vertical black solid line shows the propellers plane position (X_w^{max} = $10D_p$, X_w^{min} = $7D_p$).

deeper scour hole near the front wall. The same pattern is observed in Mujal-Colilles et al. (2018). The larger the propeller bed clearance, the lower is the influence of the horizontal boundary and therefore, a more energetic jet reaches the vertical structure, thus inducing a deeper FWH hole. The wall clearance is related to both the depth of the FWH hole and the merging of the HBH and FWH hole. This effect is clearly visible in Figure 3.4 (a) and (b), where the two paradigmatic scenarios, i.e., propeller located close to the bed and far from the wall or far from the bed and close to the wall, are shown. The condition of *merged* or *no-merged* holes is related to the development of the scour hole and is analyzed in detail in Section 3.3.1.

As previously explained, B & F scenarios (Figure 3.5 (a) and (b)) aim to be more realistic in terms of reproducing arrival and departure ship maneuvers, where the propellers are used mostly in backward and forward regimes, respectively. In these experiments, a new scour hole is formed upstream of the propellers plane (HBA, Harbour Basin Area), due to the backward (BWD) rotation. In advance, this scour hole will be referred as HBH_{BWD} hole. The structure nearby the propellers, simulating the ship hull, deflects the jet flow and causes the scour hole to be closer in this regime than the hole at the harbor basin area due to forward rotation, in advance HBH_{FWD} hole. The behavior of the backward flow is obviously not comparable to a free developing jet, and neither is the scour hole created. The HBH_{BWD} hole, although of considerable depth in some of the experiments ($\sim 1.5D_p$), does never reach

to merge with the FWH hole and a very clear separation always exist between them. It is thus considered that they must be object of an independent analysis. This particular behavior is detailed in Section 3.3.2.

The HBA area downstream the propeller plane, where the HBH_{FWD} hole is found, is not highly eroded in the B & F experiments. A different behavior is observed in the downstream holes, compared to the FWD experiments. The suction of the propellers when rotating backward and the accretion area in the surroundings of the HBH_{BWD} hole may be of importance, contributing to an erosion-refilling process that keeps the morphology in the HBH_{FWD} less affected in comparison with its analogue (HBH hole) in FWD experiments. In Figure D.7 (Appendix D.1), for instance, it is observed that the HBH_{FWD} hole is reduced at t = 15min, respect to t = 10min, and the same happens at t = 25min, respect to t = 20min. At t = 15min and t = 25min, the backward rotation just finished, while at t = 10min and t = 20min the forward rotation just did.

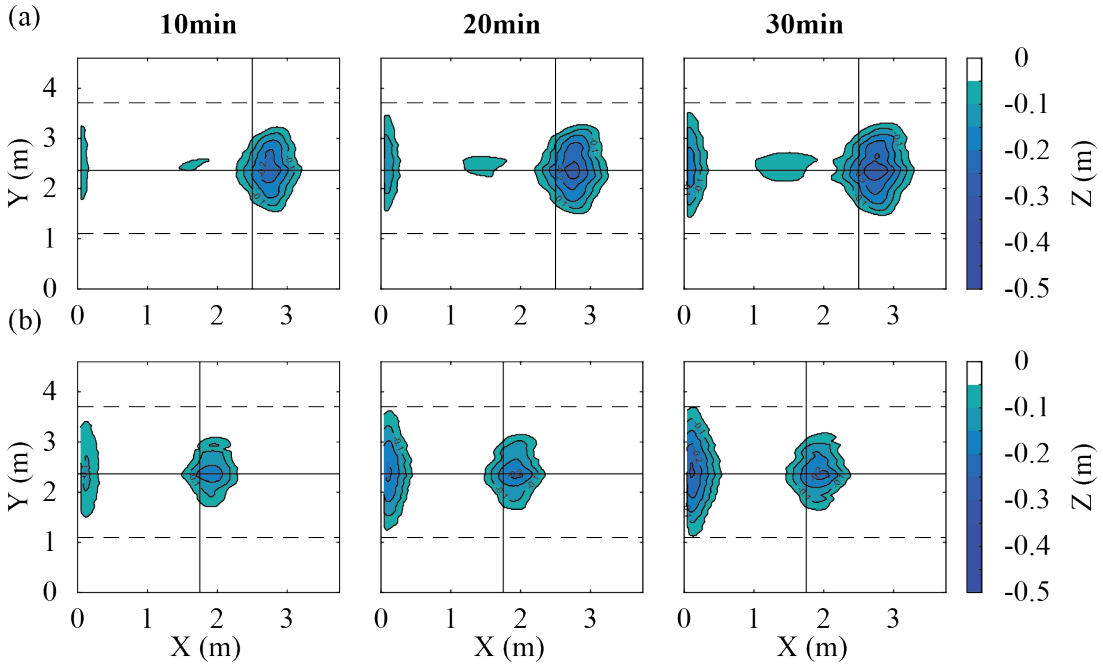

FIGURE 3.5: 2D contours of the plain view. (a) Exp # 8: C_h^{min}, X_w^{max}, B & F regime, 350rpm; (b) Exp # 5: C_h^{max}, X_w^{min}, B & F regime, 350rpm. The vertical black solid line shows the propellers plane position (X_w^{max} = $10D_p$, X_w^{min} = $7D_p$).

3.3.1 Maximum depth profile

The evolution of the maximum scouring depth profile is a key to obtain both the position of the maximum expected depth and the maximum length of the entire scour hole. These geometric characteristics are needed to estimate parameters of interest such as the eroded volume (Penna et al., 2019). In the current experiments, due to the distance between the twin propellers (a_p), a single scour hole is observed as the

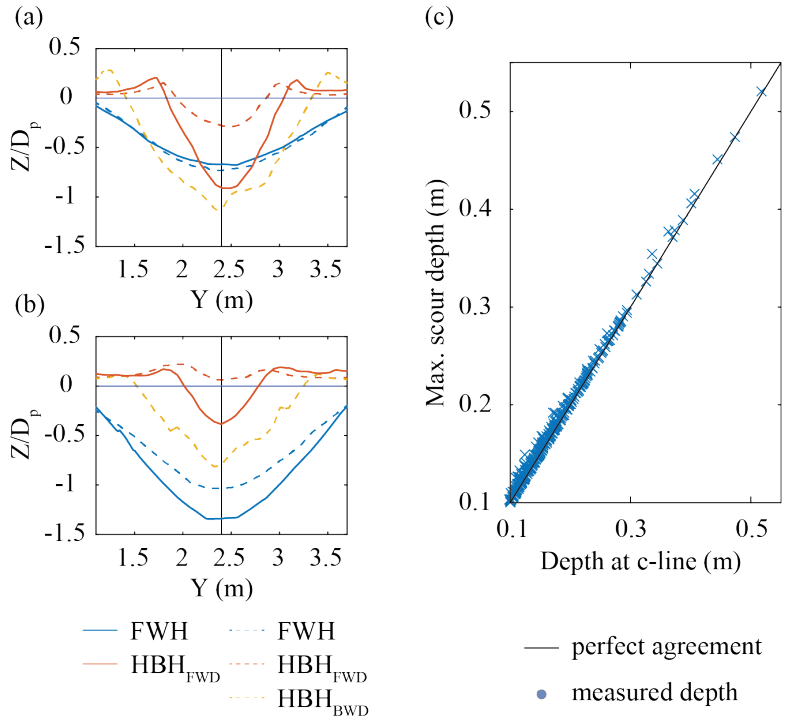

FIGURE 3.6: Transverse profiles at the three scour holes location in FWD experiments (solid line) and B & F experiments (dashed line) for a speed of rotation n=350rpm. (a) C_h^{min}, X_w^{max}; (b) C_h^{max}, X_w^{min}. (c) Agreement between the maximum depth and depth at the center-line at the same X position along the whole measurement grid, for all the experiments and time intervals.

bed morphology evolves, as seen above (Figures 3.4 and 3.5). The centre-line profile, located between the twin propeller axes, is considered to be the longitudinal axis from where the scour hole expands symmetrically. Figure 3.6 (a) and (b) shows the transverse profiles at the location of the maximum depth of every scour hole. Both FWD and B & F experiments are considered. The maximum depth at every X position along the whole measurement grid, with $\Delta X = 0.01$m, is compared with its corresponding center-line depth measured at the same X coordinate (for depths higher than 0.1m). The agreement, in Figure 3.6 (c) indicates that a negligible error is committed if the maximum depth profile is assumed to be in the center-line (rmse = 0.005 m). Thus, the following analysis of maximum scour depth in this chapter is focused on the center-line profile.

The center-line profiles evolve differently depending on the experimental conditions. In every profile, the separation between the FWH hole and the HBH hole is found by locating the local maximum between the FWA area and the HBA area. The method is based on the calculation of the first derivative at each position and is explained in detail in Appendix C. Figure 3.7 (a) to (d) shows that this maximum is found in some of the experiments (solid line profiles), although not in all of them

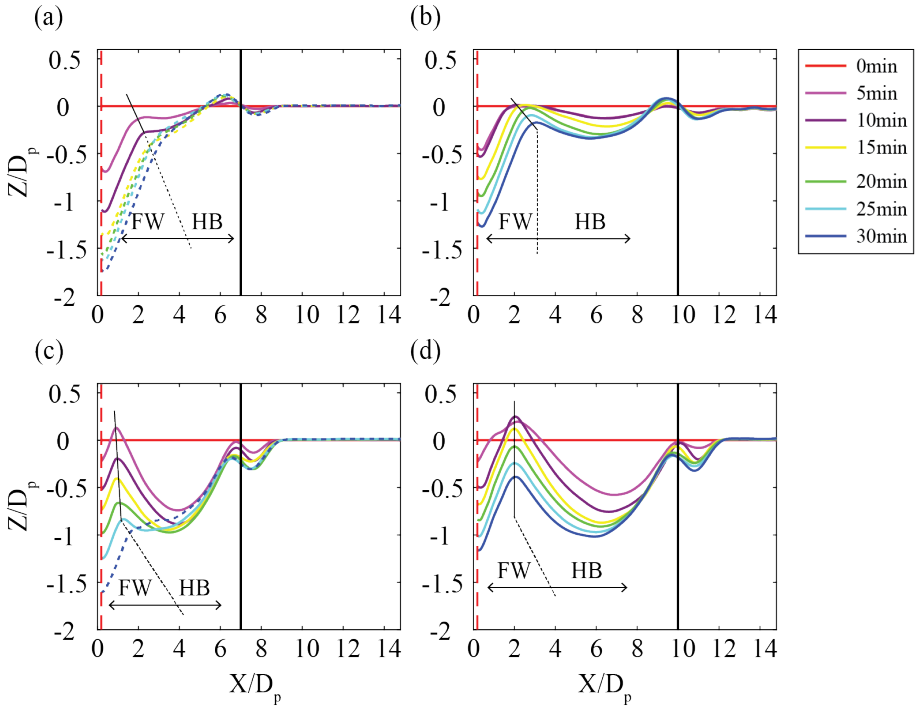

FIGURE 3.7: Longitudinal profiles of FWD experiments at 400 rpm. (a) C_h^{max}, X_w^{min}; (b) C_h^{max}, X_w^{max}; (c) C_h^{min}, X_w^{min}; (d) C_h^{min}, X_w^{max}.

(dashed line profiles), due to the merging of the two holes.

Since the morphological differences (one or two holes in the maximum depth profile) depend not only on the experimental conditions, but also on time, central profiles are categorized as follows: *no-merged*, *transition to merge* and *merged* profiles, according to the methodology detailed in Appendix C.

Figure 3.7 clearly shows that, in FWD experiments, X_w^{min} scenarios (Figure 3.7 (a) and (c)) tend to yield a merged profile, while X_w^{max} experiments (Figure 3.7 (b) and (d)) preserve the initial two-hole shape. This is especially true in C_h^{min} cases, where the HBH hole is much more developed than in C_h^{max} experiments.

The longitudinal profiles in B & F experiments are categorized into *no-merged* and *merged* profiles according to the same criteria explained for FWD experiments (see Appendix C). In these experiments, the main hole far from the FW appears due to the backward rotation (HBH_{BWD} hole), while the HBH_{FWD} and FWH holes are the ones that may merge or keep the two-hole shape. In Figure 3.8, *merged* profiles are observable (dashed lines) in the X_w^{min} cases (Figure 3.8 (a) and (c)), while the *no-merged* profiles are found in X_w^{max} experiments (Figure 3.8 (b) and (d)). This is in accordance with the results in FWD experiments. In case of B & F experiments, although the propeller's forward rotation time is reduced to the half (compared with FWD experiments), the maximum scour depth at the FW barely changes between

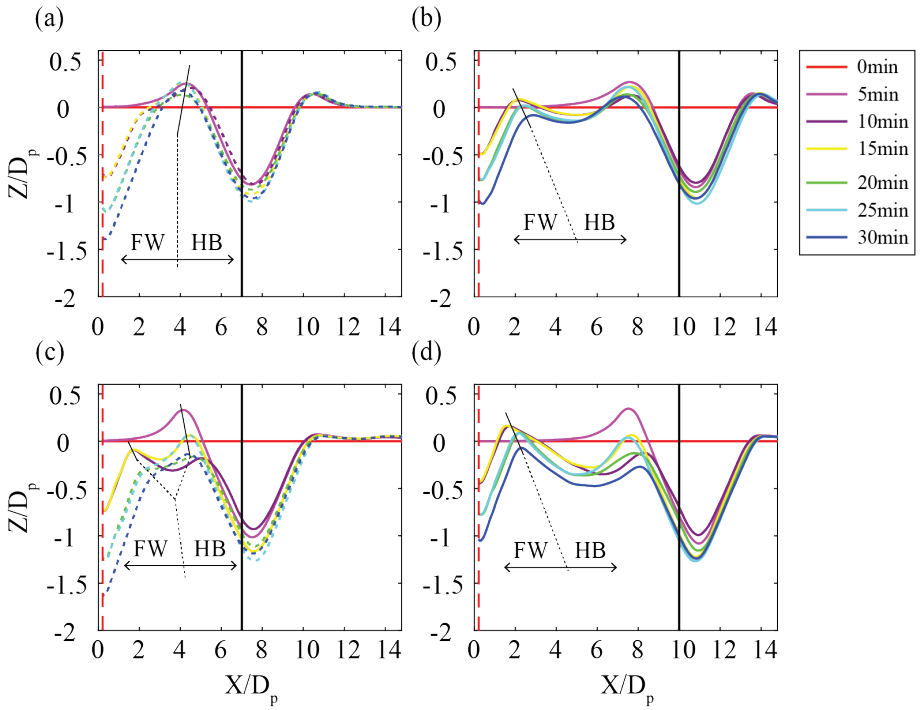

FIGURE 3.8: Longitudinal profiles of B & F experiments at 400 rpm. (a) C_h^{max}, X_w^{min}; (b) C_h^{max}, X_w^{max}; (c) C_h^{min}, X_w^{min}; (d) C_h^{min}, X_w^{max}.

both scenarios. This behavior is analyzed through the time evolution of the maximum scour depth, in Section 3.3.2.

3.3.2 Time-series of maximum scour depth

Maximum depth at the Front Wall

The different evolution in the maximum scour depth near the FW is observed in Figure 3.9, both in case of X_w^{min} and X_w^{max} (Figure 3.9 (a) and (b), respectively), at each C_h and regime (FWD and B & F). Note that the reference time in this figure is modified to fit only the forward rotation time to facilitate the comparison between FWD and B & F scenarios. The time series in this figure includes the long experiments (up to 60 minutes) summarized in table 3.3.

Figure 3.9 shows that in all cases, C_h^{min} experiments (red lines) in B & F regime (solid lines) yielded higher scour depths near the front wall than their corresponding FWD experiment. In case of C_h^{max} (blue lines), FWD and B & F experiments show an almost identical behavior at minimum wall clearance, i.e., X_w^{min} (Figure 3.9 (a)). On the other hand, in X_w^{max} experiments (Figure 3.9 (b)), B & F experiments yielded again higher depths at the FW, at any time.

In Figure 3.9 (a) (X_w^{min}), the maximum depth evolution exhibits a change in the growing trend, pointing to the stabilization of the maximum scouring depth, at the

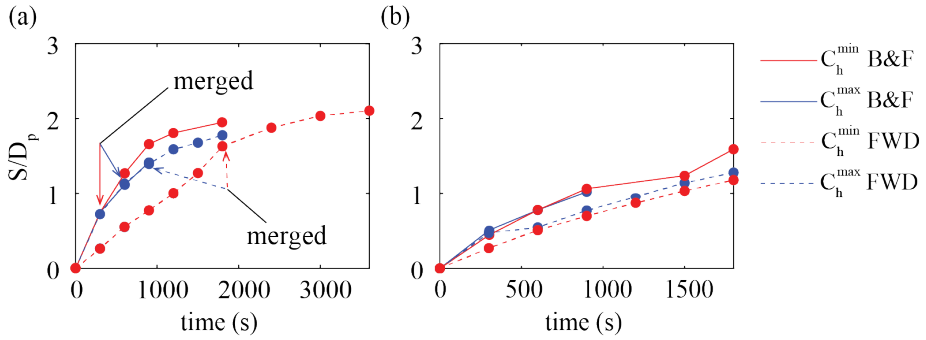

FIGURE 3.9: Evolution of maximum depth at FW. Experiments at 400rpm. The arrows show the merging time. (a) X_w^{min}; (b) X_w^{max}. The reference time in the figure is adjusted to fit the forward rotation time.

same FW depth ($\approx 2D_p$) in all cases. In case of FWD experiments, the change in the trend is found just after the profile becomes *merged*. In case of B & F, although the profiles are merged at an earlier time, the stabilization is reached at the same depth than at FWD ones, meaning that the FW hole morphology evolution may be conditioned by the different regime (FWD or B & F), but the maximum scouring depth do not necessarily change.

In case of mid or low speed of rotation (350 rpm and 300 rpm), the behavior observed in the scour profiles does not change substantially, compared to 400 rpm. In general, the scour depth is reduced and the merging, if exists, is delayed with the lower speed of rotation. The scour depth evolution and the longitudinal profiles in case of mid and low speed of rotation scenarios are shown in Appendix D.3 and Appendix D.2, respectively. Remarkably, clear differences are observed in case of B & F experiments, depending on the wall clearance. In these experiments, minimum wall clearance yielded higher scour depths at any speed of rotation, regardless of the C_h variable. In case of FWD experiments, not such a clear difference is observed, being the C_h variable also significant in the scour depth evolution. The maximum depth near the FW is studied in detail in Sections 3.3.4 and 3.3.5.

Maximum depth at the Harbor Basin. FWD experiments.

In FWD experiments, the evolution of the HBH is plotted in Figure 3.10 for each experiment, at each speed of rotation. These figures show that, regardless of the speed of rotation, only X_w^{min} experiments end up with a merged profile, being this feature highly related to the wall clearance. Once the profile is merged, only one scour hole is found and the position of the maximum depth becomes the same for both FWH and HBH holes. The experimental time step at which the merging occurs is shown in Figure 3.10, with black arrows. Since the equilibrium depth is not reached, longer experiments are needed to evaluate the final condition of each experiment. Due to the growing trend in the FWH hole in case of X_w^{max} experiments (Figure 3.10 (b)) it is

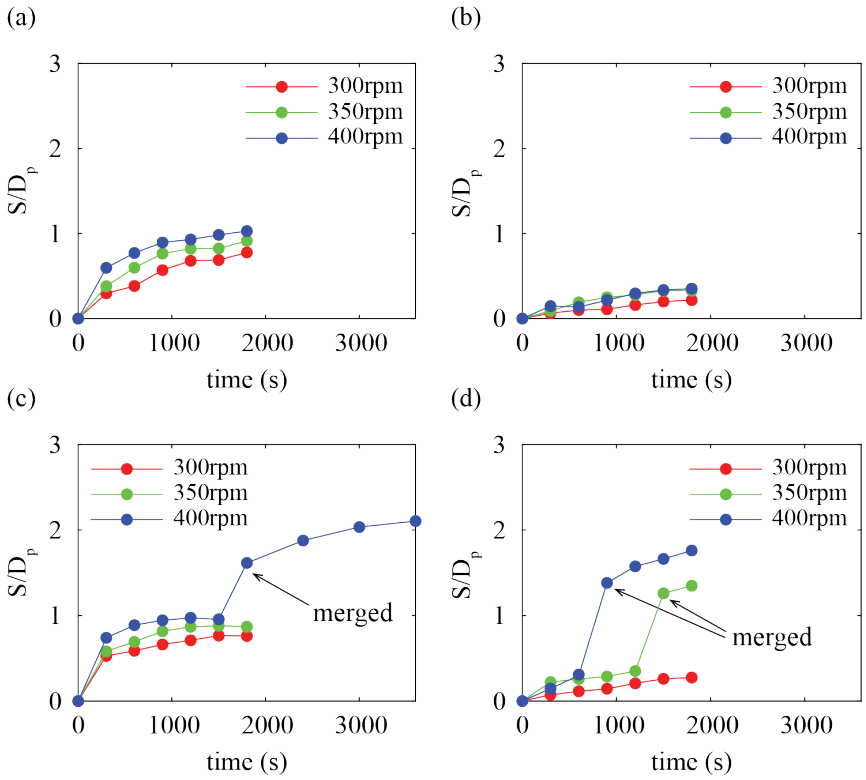

FIGURE 3.10: Evolution of maximum depth at HB. Only FWD experiments. The black arrows show the merging time.(a) C_h^{min},X_w^{max}; (b) C_h^{max},X_w^{max}; (c) C_h^{min},X_w^{min}; (d) C_h^{max},X_w^{min}.

presumable that merging of the two holes can eventually occur.

The evolution of HBH holes at different wall clearance distances, both in C_h^{min} and C_h^{max} scenarios, is comparable up the merging process occurs. However, the C_h variable clearly conditions the maximum depth in the present experiments, reaching $\approx 1D_p$ in case of C_h^{min} and less than $\frac{1}{2}D_p$ in case of C_h^{max}. Interestingly, the maximum depth in the HBH does not overcome $\approx 1D_p$ in any case. Indeed, in case of C_h^{min}, X_w^{min} (3.10 (c)), the maximum depth evolution behaves as an equilibrium depth when reaches the mentioned threshold, until the profile becomes merged. After that, as seen in Fig 3.9, the whole profile tends to the stabilization. One can compare the time-series in Figure 3.10 (c) with their corresponding longitudinal profile evolution in Figure 3.7 (c) (X_w^{min}, C_h^{min}) to observe the relation between the maximum depth in the HBH hole and the evolution of the morphology of the scour profile. At t = 10 min, the maximum scour depth of $\approx 1D_p$ is reached and no further growing is observed. However, the downstream boundary of the scour hole is being eroded due to the effect of the wall. At t=25 minutes, the downstream boundary of the scour hole already reached the same depth ($\approx 1D_p$) as the maximum scour depth at the HBH hole. At this point, the profile becomes *merged*. The further development of the *merged* profile, up to 60 minutes, is observed in the time-series.

Maximum depth at the Harbor Basin (B & F experiments)

During the B & F experiments, scour holes due to backward rotation appears at the upstream side of the propellers (the opposite of the front wall) as shown previously in Figure 3.5. The time-series in Figure 3.11 show the evolution of the maximum depth at the HBH_{BWD} holes, at each experiment. A coincident behavior is observed at X_w^{min} and X_w^{max}, since the effect of the wall is not relevant during backwards rotation. Therefore, the X_w^{min} and X_w^{max} time-series are considered just as experiments to prove repeatability.

Some differences are observable between the maximum scour depth at C_h^{min} (Figure 3.11 (a) and (c)) and at C_h^{max} (Figure 3.11 (b) and (d)), yielding the latter slightly lower values of eroded depth. Since both scenarios can be considered as low bed-clearance conditions, a big difference is not observed. Differences due to the propellers speed of rotation are present in all cases, showing consistency in the results, although they are not of considerable magnitude. Still, the well-defined evolution of all the experiments shows agreement with the expected results.

In these time-series, a common behavior is observed for any experimental condition: rapid growing at the first 5 minutes and maximum depth stabilization at an approximated scour depth of $\approx 1D_p$. After that, an erosion refilling process is observed in the maximum depth time-series, similar to the expected in case of live-bed scour, due to the change between Forward and Backward rotation.

The scour depth does not substantially change from $t = 5$ minutes to the end of the experiment (either 30 or 60 minutes), compared with the huge increase at the first time step. For instance, considering the scenarios of maximum propeller speed of rotation, the increase in maximum depth between 15 and 25 minutes (i.e. 5 minutes of forward and 5 minutes backwards rotation) at the HBH_{BWD} hole, in average, is 0.0035 ± 0.001 m per minute, which is of the order of magnitude of the sediment diameter. Considering all the experiments, the average depth increase between 15 and 25 minutes is 0.017 ± 0.006 m, which corresponds to a 6 ± 0.8 % of the total depth. Moreover, the profiles up to 60 minutes do not show any significant increase in the maximum depth evolution. Therefore, although some increase may be expected in case of longer experiments, the asymptotic or equilibrium depth is assumed to be close to the measured scour depth at t = 25 minutes (the last time interval with backwards rotation in common at all the experiments). Considering the depth at 25 minutes as the equilibrium depth, used to normalize every scour depth at any time, the general model in Eq. 3.2 is adjusted to the experimental data. Note that in this case, the time is re-scaled to fit the backwards rotation time.

$$\frac{S_{m,t}}{S_{m,e}} = 1 - exp[A(\frac{t}{T})^B] + C \tag{3.2}$$

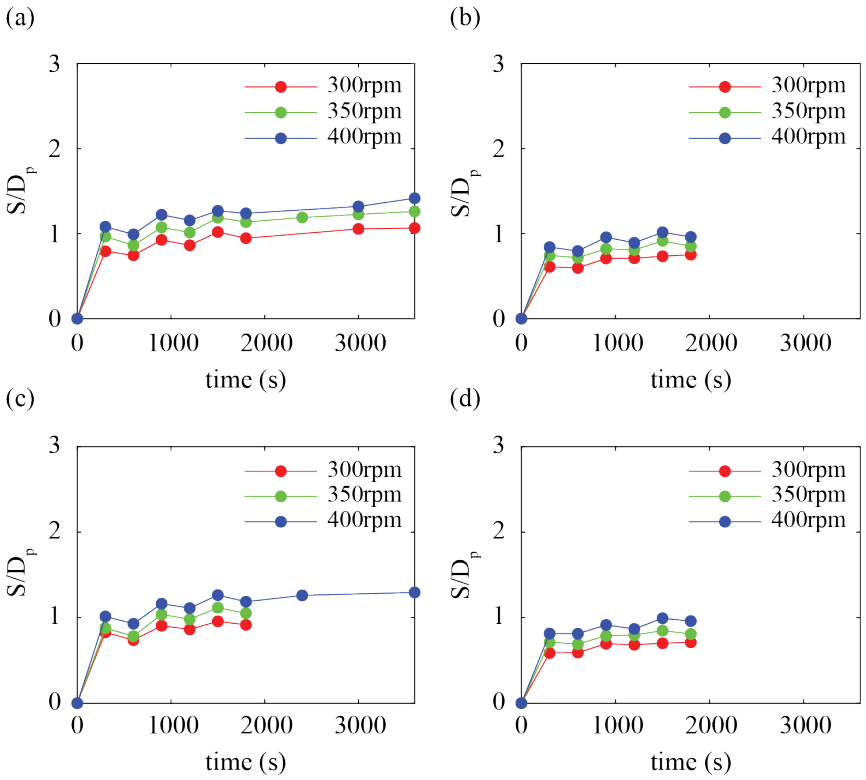

FIGURE 3.11: Evolution of maximum depth at HB. Only B & F experiments. (a) C_h^{min},X_w^{max}; (b) C_h^{max},X_w^{max}; (c) C_h^{min},X_w^{min}; (d) C_h^{max},X_w^{min}.

where:

$S_{m,t}$ = Scour depth at the HBH_{BWD} at any time (t) (m)
$S_{m,e}$ = Maximum or equilibrium scour depth at each experiment (m)

With t in seconds, and T being the time-scale, which is the value of the speed of rotation (s^{-1}). The adjustment yielded $A = -0.01$, $B = 0.7$ and $C = 0.006$, with an $R^2 = 0.995$. The adjustment and the agreement are shown in Figure 3.12, grouped by C_h.

As seen in the time-series in Figure 3.11, the maximum scour depth ($S_{m,e}$) can be defined as a function of the bed clearance (C_h) and the speed of rotation (n), since these are the variables conditioning the scour process in case of backward rotation. Considering the maximum depth (at t = 25 minutes) as the equilibrium depth at each experiment, Eq. 3.2 is adjusted to predict $S_{m,e}$ as a function of the experimental variables. The U_0 is not included in this analysis, since there is no experimental evidence that one can assume the efflux velocity to be equal to the induced velocity in backwards rotation. Instead, nD_p is included in the Froude number in Eq. 3.3.

$$\frac{S_{m,e}}{D_p} = A\left(\frac{nD_p}{\sqrt{gD_p}}\right)^B \left(\frac{C_h}{D_p}\right)^C \tag{3.3}$$

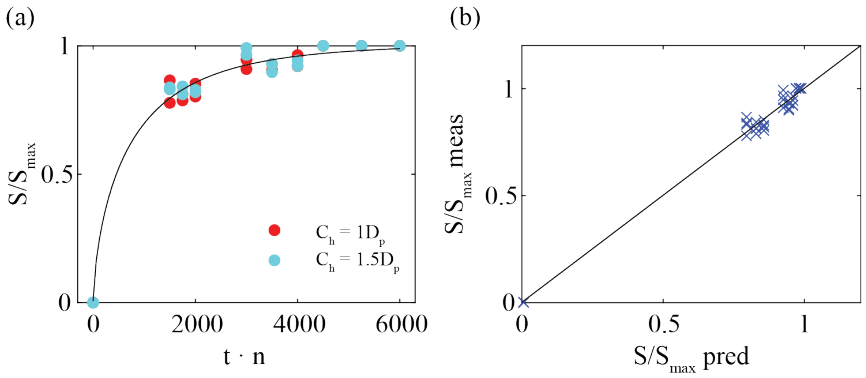

FIGURE 3.12: (a) Adjusted model to the HBH_{BWD} data. (b) Agreement between predicted and measured dimensionless scour depth.

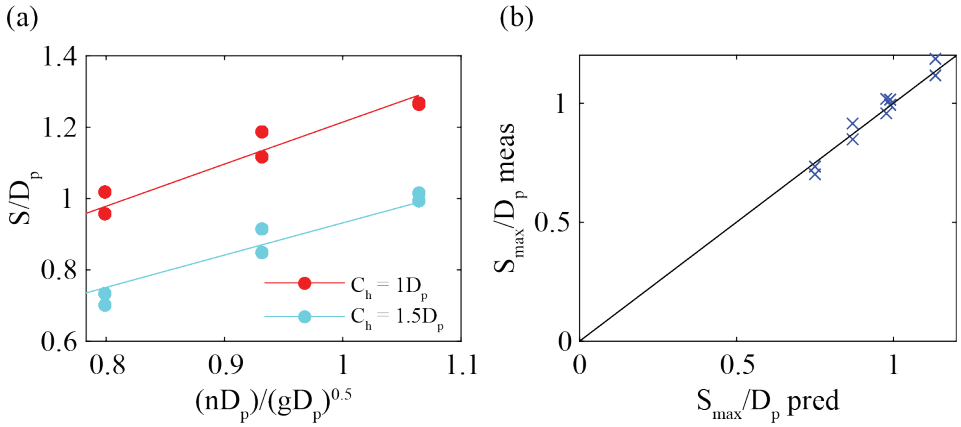

FIGURE 3.13: a) Adjusted model to the HBH_{BWD} data. (b) Agreement between predicted and measured dimensionless scour depth.

The best fit for the adjusted model yielded $R^2 = 0.97$, with $A = 1.21$, $B = 0.96$ and $C = -0.65$. However, if the coefficients B and C are fixed to 1 and -0.5, respectively, the maximum scour depth, normalized with the propeller diameter, is proportional to the Froude number $(\frac{nD_p}{\sqrt{gD_p}})$ and inversely proportional to the squared root of the bed clearance $(\frac{C_h}{D_p})$. In this case, the proportionality coefficient, A, is 1.19 and the determination coefficient is $R^2 = 0.94$. This is shown in Figure 3.13, where the predicted scour depth at each C_h condition is plotted together with the measured data. Therefore, 3.3 is proposed as a new empirical model to estimate the equilibrium scour depth due to backward rotating propeller jets in low bed clearance conditions.

$$\frac{S_{m,e}}{D_p} = 1.19\left(\frac{nD_p}{\sqrt{gD_p}}\right)\left(\frac{C_h}{D_p}\right)^{-0.5} \tag{3.4}$$

3.3.3 Maximum depth position

The expected position of the maximum scour depth in case of twin propeller confined jets is analyzed by finding the maximum depth at HBA and FWA sub-areas in

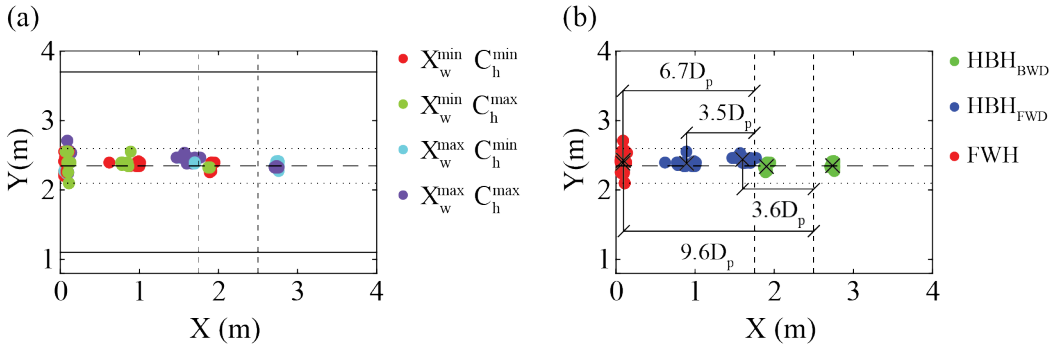

FIGURE 3.14: Position of the maximum depth in the FWA and HBA areas. All the experiments are included. (a) Positions colored by experimental conditions. (b) Clustering defining the three different types of scour hole, along with the distance to the cluster centroid. Vertical dashed lines show the position of the propeller plane. Horizontal solid lines in (a) show the measurement grid boundaries over the Y axis.

each profile. Therefore, in case of *merged* profiles at FWD experiments, only one maximum depth position is shown (near the Front Wall), while in any other case both the maximum depth at the FWA and the HBA sub-areas are located. In Figure 3.14, the positions of the maximum depth over the whole grid are observed, grouped by its corresponding experimental conditions (Figure 3.14 (a)) and clustered by hole type (Figure 3.14 (b)). The k-means clustering algorithm locates 5 different data clusters to minimize the distance (Euclidian distance) between each object and the cluster centroid. The centroid is assumed to be a representative position of the maximum depth location of every characteristic scour hole. Within every cluster a unique value of X_w is present, clearly meaning that nor C_h, U_0 and time are relevant in the location of the scour hole. Interestingly, the distance to the maximum depth position of the HBH$_{FWD}$ hole barely changes, although the wall clearance changes considerably, thus pointing to a negligible effect of the FW in the spreading of the twin propeller jet, in the range of distances covered by the present experiments.

3.3.4 Comparison with literature

Although twin propellers are a very common propulsion system in several types of maritime vessels, few works have been published regarding twin propeller induced scour, and lesser in case of confined jets. Some recommendations are found in the international guidelines (PIANC, 2015; BAW, 2010), considering this type of propulsion system and focused on maximum scour depth prediction. Since the equilibrium condition is not found in all cases, the expressions in literature focused on the calculation of the equilibrium depth are not comparable to the obtained results directly. However, the existing models to obtain the time-dependent scour depth may be applied. Cui et al. (2020b) proposed an empirical model for inwards rotating twin propellers in confined scenarios, following the previous study of unconfined twin

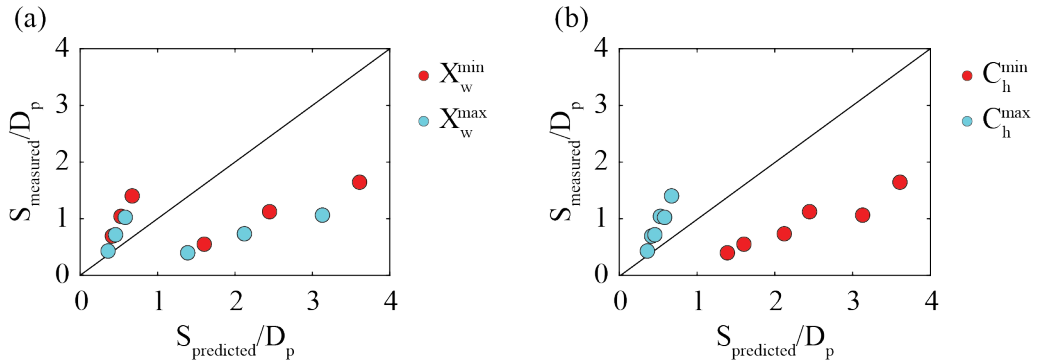

FIGURE 3.15: Comparison between literature equations and experimental results at t=30min.

propeller scour in Cui et al. (2019), where a temporal model for the prediction of the induced scour due to twin propeller jets is shown. Cui et al. (2020b) proposed Eq. 3.8 to simply obtain the maximum scour due to a confined twin propeller jet (S_{conf}), from the more complex Eq. 3.5 in Cui et al. (2019), focused on the time evolution of the maximum scour depth in case of unconfined twin propeller jets (S_{unconf}).

$$S_{unconf} = \Omega[ln(t)]^{\Gamma} \tag{3.5}$$

$$\Omega = 0.2526(\frac{a_p}{d_{50}})^{-0.859}(\frac{C}{d_{50}})^{-4.63}(\frac{D_p}{d_{50}})^{3.58}Fr_d^{4.35} \tag{3.6}$$

$$\Gamma = 1.389(\frac{a_p}{d_{50}})^{0.1571}(\frac{C}{d_{50}})^{0.742}(\frac{D_p}{d_{50}})^{-0.522}Fr_d^{-0.682} \tag{3.7}$$

$$\frac{S_{conf}}{S_{unconf}} = 3.5(\frac{X_w}{D_p})^{-0.4} \tag{3.8}$$

In this case, the experimental values obtained at $t = 30$ minutes, as in Cui et al. (2019), are used. Only FWD experiments are included for the sake of good comparison. Although in Cui et al. (2020b), only experiments with the lower bed clearance are performed ($0.5D_p$ from the propeller tip, i.e., C_h^{min} scenarios in the present work), Cui et al. (2019) included a more extensive range of seabed clearance distances, considering the influence of this variable on the final scour profile. The range of bed clearance in Cui et al. (2019) is coincident with the one in the present work. In Figure 3.15, the predicted scour depth values yielded by Eq. 3.8 are plotted against the measured scour depths near the front wall in the work presented herein. Significant disagreements are found between the experimental results and the proposed models. The results are colored by X_w and C_h, showing that the proposed model clusters the data according to the clearance distance, since this variable is not considered as input parameter. Moreover, the results of the present study do not fit the model neither in case of C_h^{min} nor C_h^{max}.

3.3.5 Temporal evolution of maximum scour depth at FW

Since the existing models do not fit the results obtained in the laboratory, a new empirical non-linear model for time-dependent scour due to confined twin propeller jets is proposed, regardless of the unconfined scour profile. The time-dependent scour depth near the front wall (S) can be expressed as a function of the following dimensional parameters:

$$S = f(U_0, X_w, C_h, d_{50}, g, \rho_w, \rho_s, t, \mu, a_p) \tag{3.9}$$

In the present set of data, important parameters clearly conditioning the scour process (d_{50}, a_p) are unique due to experimental limitations. The other important parameters involved in the propeller induced scour (U_0, X_w, C_h) cover a realistic range of values in cases of RO-RO ships maneuvering in shallow waters, i.e. with low UKC, since they are scaled from the study case vessel type as explained in Section 3.2.2.

Using the Buckingham Π theorem, if constant parameters and viscosity are not considered and ρ_s, X_w, and U_0, are used as fundamental variables, the following non-dimensional parameters are obtained:

$$\Pi_1 = \frac{S}{X_w} \tag{3.10}$$

$$\Pi_2 = \frac{C_h}{X_w} \tag{3.11}$$

$$\Pi_3 = \frac{U_0}{\sqrt{gX_w}} \tag{3.12}$$

$$\Pi_4 = \frac{t}{X_w/U_0} \tag{3.13}$$

$$\Pi_1 = f(\Pi_2, \Pi_3, \Pi_4) \tag{3.14}$$

The confinement situation is considered to be the most important characteristic of the scour near quay walls, and consequently the wall clearance (X_w) is chosen as fundamental parameter. Thus, Π_3, a Froude number the characteristic length of which is not the jet or propeller diameter, but the wall clearance, is obtained. This parameter is referred in advance as wall Froude number (Fr_w). The Fr_w increases linearly with the efflux velocity and decreases with the square root of the distance to the wall, meaning that the relation between the initial velocity of the jet and the distance from the jet to the quay wall is of main importance in the confined scour process. Time is dimensionless with the time scale, which in this model is proposed to be (X_w/U_0). An optimization of the general non-linear model in Eq. 3.14 is performed to get the best coefficient of determination, and different constants and powers [k_1, a, b, c] are proposed to obtain the best fit.

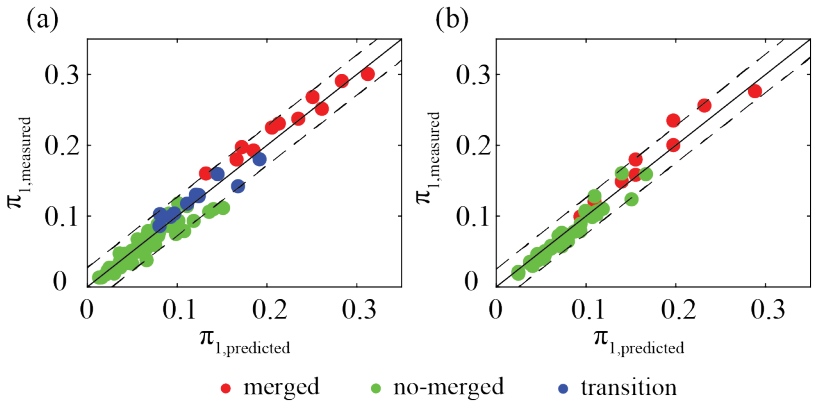

FIGURE 3.16: Agreement between predicted and measured scour depth at the FW, relative to the wall clearance. (a) FWD experiments (b) B & F experiments

Figure 3.16 shows the linear agreement between the predicted and measured scour depth to the wall clearance (Π_1) in case of FWD experiments (Figure 3.16 (a)) and B & F experiments (Figure 3.16 (b)). The merging condition is chosen as the grouping variable, yielding a clear gradient from no-merged to merged scenarios as the maximum depth – wall clearance ratio increases. In both cases, the transition between no-merged and merged is located around $\Pi_1 \approx 0.15$. The different fitted logarithmic curves and the measured data, coloured depending on the experimental setup in the legend, are plotted and included in Appendix E, Figure E.1. In case of FWD experiment, the data corresponding to the experiments with $n = 350$ rpm (mid speed of rotation) are not shown to avoid overlapping data points.

A different model is fitted for each gear scenario (FWD and B & F experiments). Eq. 3.15 and Eq. 3.16 show the non-linear models for each one of them, that yielded coefficients of determination $R^2 = 0.971$ and $R^2 = 0.952$ respectively. For FWD experiments, the time dependent scour depth increases with the Fr_w to the power of 2, being this parameter much more influent than the bed clearance (C_h). In case of B & F experiments, the bed clearance does not even appear in the equation, thus the scour depth depends on Fr_w and time. It must be mentioned that the time variable in B & F experiments is referred only to the forward rotation time in the experiments.

$$\frac{S}{X_w} = 2.539 \times 10^{-4} \left(\frac{C_h}{X_w}\right)^{0.5} \left(\frac{U_0}{\sqrt{g X_w}}\right)^2 \left[ln\left(\frac{t U_0}{X_w}\right)\right]^{4.425} \tag{3.15}$$

$$\frac{S}{X_w} = 2.531 \times 10^{-3} \left(\frac{U_0}{\sqrt{g X_w}}\right)^{2.67} \left[ln\left(\frac{t U_0}{X_w}\right)\right]^{3.19} \tag{3.16}$$

At any time, both for FWD and B & F scenarios, a linear agreement is found between Fr_w and Π_1, yielding a coincident threshold value of Fr_w above which erosion near the quay wall is present. The threshold value of sediment scour at FW is found to lay between 0.25 and 0.3, thus, no significative scour should be found if

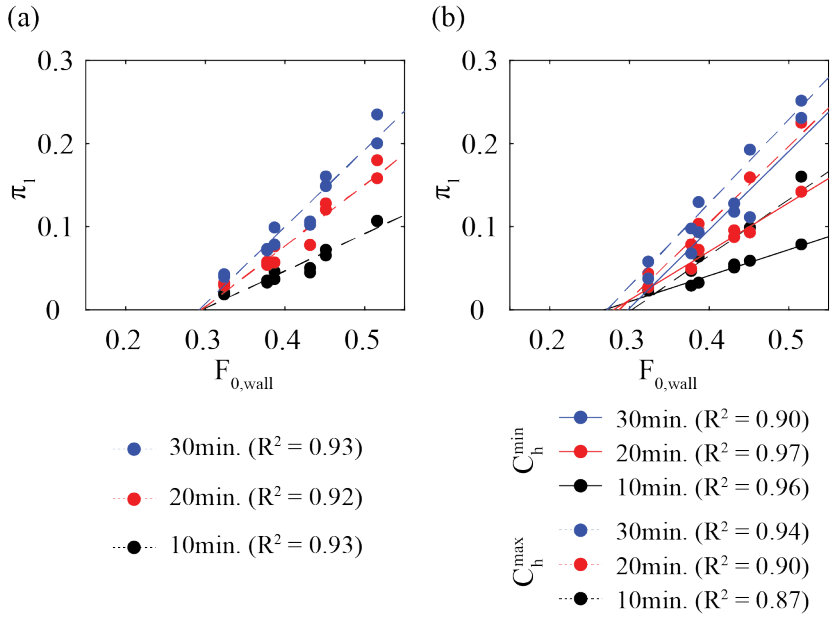

FIGURE 3.17: (a) B & F; (b) FWD.

$Fr_w < 0.25$. Figure 3.17 shows the scour depth values at FW, relative to the wall clearance, and their linear relation with the wall Froude number at each case.

3.4 Discussion

In the present chapter, the scouring action produced by twin propellers nearby quay walls is studied through a set of laboratory experiments over a mobile sand bed. The scouring action of this particular propulsion system, although very common in a wide range of ships, has been barely studied so far compared to the scour due to single propeller jets. The maximum scour depth is a measure of the potential damage and it is a needed parameter in marine structures design. In PIANC (2015), it is recommended to account for the over-costs due to either a deeper construction according to the predicted maximum scour depth or due to scour protection if the former is not considered. The maximum scour depth is found in the equilibrium profile of any scour hole. Most of the laboratory experiments in propeller scour are thus focused on finding the equilibrium profile and characterizing the maximum scour depth as a function of the experimental setup. However, experiments at laboratory are limited and it is time-consuming to account for all the parameters involved in the scour phenomenon, summing up the intrinsic effects that the scale may have in any laboratory study (scale effects due to gravity or sediment size for instance). Still, the major part of the scientific literature in propeller scour in the past years comes from physical models. Several examples are mentioned in the introductory section of this chapter.

The limits of the scouring areas, named FWA and HBA areas following Mujal-Colilles et al. (2018) terminology, have been defined in this paper by finding the boundaries of the scour holes, which expand from its maximum depth position located either near the FW, downstream the propellers in the HB or upstream the propellers below the ship's hull, as detailed in Section 3.3.1. Although it is not expected to find such clearly distinguishable areas in-situ due to the ship motion, differences may be observable if scour holes are found in the HB or near the FW, thus knowing that a FWH hole or a HBH hole is present. In Mujal-Colilles et al. (2017b), for instance, the scour holes near the quay walls and far from them, at the harbor basin, are observable and analyzed through bathymetric studies performed by the port authorities during several years. The merging of the FWH and HBH hole should be also considered, since it is pretty clear that short distances to the front wall have a great influence on the development of a deeper scour hole.

The backward rotation is here analyzed for the first time to advise the effects of real maneuvers over the harbor basin sediment bed. Clear differences are observed, as expected, in the evolution of the downstream holes due to forward rotation, and to ones created upstream when the propellers are operating in backward regime. The difference in the flow field and, overall, the interaction with the ship's hull may be of great importance. In this case, a proper model of a ship hull is not used, but the effects observed may be used as an approximation of the real cases. The obtained data in maximum scour depth due to backward rotation showed a very well-defined behavior, being the speed of rotation and the clearance distance the two variables conditioning the scour depth evolution. Equilibrium is not considered to be totally reached, but no significant changes are expected in any of the analyzed experiments. The proposed model, thus, is considered to be useful for practical applications, and expected to yield good results in the range of the present non-dimensional parameters, with due consideration of the effects of the change in sediment size.

Section 3.3.5 shows that the more harmful scenarios correspond to the lower wall clearances, regardless of the change in flow velocities. The affected area is not analyzed in detail in this chapter, although it is a variable of interest and must be studied in future works. In Roubos, Blockland, and Van Der Plas (2014), the authors point out that the effects of the twin jets, compared to the effects of a single jet, are related to a larger scour area, although not necessarily a deeper hole. It is considered that mainly the a_p/D_p and the X_w/D_p ratios play an important role in the widening and deepening of the scour hole, and thus both terms must be considered in confined twin propeller induced scour studies. For a unique distance to the quay wall, a higher a_p/D_p is expected to enlarge the width of the scour hole while decrease its depth. In the experiments presented in this article, the distance between the propeller axes is not included as a variable, and the results obtained must be considered in case the a_p/D_p is coincident or similar to the one in this work. Even so, it is not

considered that the a_p/D_p ratio can have a very wide variability in the case of the main propellers, although it could vary widely in the case of transverse thrusters.

The effects of the seabed clearance, C_h, have been analyzed in this work, showing an opposite effect over the HBA and the FWA areas. While at HBA area, the bed clearance has an inverse relation with the scour depth, S, (the farther the propeller is located, the less scour is found), the effects over the FWA area are found to follow direct relation with the bed clearance. Two different distances are studied in the present experiments, both being in the range of the low UKC. Therefore, the obtained relation between C_h and S must be expected in low bed clearance situations. At higher clearance distances, the effect of the propeller jet in the FWH hole is expected to be reduced and eventually become negligible, as it is in the case of the wall clearance. Further experiments must be focused in finding this threshold, that may have direct practical applicability at field.

The position of the maximum depth over the X axis at HBH holes, referred to the propeller plane, does not change regardless of the change in X_w, C_h or time. In all the scenarios, at any time, the maximum depth at HBH hole (or HBH_{FWD} hole in case of B & F experiments) is located at $\approx 3.5D_p$ from the propeller plane. These results are in good agreement with Cui et al. (2020b) for their experiments at $X_w = 7D_p$, although it is not explicitly analyzed in their article. The lack of change with the increasing X_w can be explained if the wall clearance does not have any effect in the expansion angle of the propeller jet at the present range of wall clearance. Wei and Chiew (2019) analyzed the effects of the vertical wall close to the propeller jet in case of single propeller, and showed that the expansion angle of the jet may decrease with the increasing wall clearance up to $X_w = 4D_p$. No effects are expected at further distance. Contrarily, the lack of change in the position of the maximum depth at the HBH hole may be related with the presence of a horizontal boundary. As studied in Johnston et al. (2013), for bed clearance up to at least $2D_p$, an increase of the expansion angle must be expected with the increasing clearance, from a minimum value of $\approx 8°$. The increase in the expansion angle due to the increase in the bed clearance in the present experiments would yield a similar distance to the jet impingement point, thus a similar location of the maximum scour depth.

As previously explained, the non-dimensional parameter Π_1 is linearly dependent on the Fr_w at each experimental time, yielding a threshold value below which scour is not found. This threshold is found at $Fr_w \approx 0.25$. In the same line, Cui et al. (2020b) reported no scour near the quay wall in the test experiments at $X_w = 9D_p$, although with wall clearance of $X_w = 7D_p$ scour was visible. Therefore, considering a no-scour threshold at $X_w = 7D_p$ in their experiments, performed over a sandy bed of $d_{50} = 0.2mm$ and with a twin-propeller of $D_p = 55mm$ rotating at 500rpm, the obtained wall Froude number is $Fr_w = 0.24$. This result is slightly below the threshold

obtained in this article, probably due to the slightly lesser sediment diameter used by Cui et al. (2020b) in comparison with the present study. This difference points to a partial agreement and to the need to consider different sediment diameters to obtain a clear threshold of the wall Froude number to prevent scour over non-protected beds in case of confined twin propeller jets.

The proposed empirical models to predict the maximum scour depth evolution are expected to work for the range of the non-dimensional parameters in this article. Due to the limitations in the sediment size, this model shall be tested over different seabed compositions to study their performance in other scenarios. However, the range of densimetric Froude number (Fr_d) covered by the present experiments ($22 < Fr_d < 32$) is closer to the real situations than most of the works found in literature, as stated in section 3.2.2, which make the results obtained more realistic to the analysis of the local scour phenomenon. Moreover, the interesting relationships that the models yielded between the different parameters are considered to be useful for future experimental designs and to practical applications. Both in FWD and B & F experiments, the most harmful experimental set up for the FW area is the combination between higher speed of rotation and shorter wall clearance, regardless of the seabed clearance in case of B & F and combined with the higher seabed clearance in case of FWD. The next two scenarios, sorting by maximum depth of scour, are by far the 400rpm X_w^{min}, and the 350rpm X_w^{min}, meaning that a significant change in the efflux velocity is not of importance if the wall clearance is not increased. The same behavior is observed at lower speeds of rotation: low speed close to the wall is more harmful than mid speed far from the wall.

According to the experimental results, a clear relation is observed between the merging condition of every profile and the scour depth. Three different categories have been assigned to any profile for any scenario at any time: *no-merged*, *transition* or *merged* profile. In both FWD and B & F scenarios, the location of the transition area points to a relation between the scour depth near the front wall and the preservation of the two-hole morphology, with a threshold around the 15% of the wall-clearance, according to the obtained results.

In Figure 3.10, an interesting behavior is observed regarding to the merging condition in C_h^{min} cases. The HBH hole is quickly developed, reaching the approximate depth of $1D_p$ after 5 minutes run both for X_w^{min} and X_w^{max} scenarios. At X_w^{min}, no growing is observed until t=25 minutes, being the observed behavior assimilable to an equilibrium profile. During all this time, the depth at HBH hole is not growing further, but the downstream boundary of the HBH hole is being eroded until it reaches the same maximum depth: $\approx 1D_p$. The two-holes profile is therefore merged. At this point, the clear linearly growing trend that the FWH hole followed so far roughly decays and the whole merged profile tend to the stabilization. At,

X_w^{max} the same behaviour is expected. The maximum HBH hole depth, thus, cannot go further $1D_p$.

3.5 Concluding remarks

- A new set of experiments on twin propeller induced scour near quay walls is presented in this work. A total of 24 experiments on confined local scour are performed with different experimental conditions, aiming to analyze the influence of important parameters such as the bed clearance (C_h), the wall clearance (X_w) and the efflux velocity of the propeller (U_0) in the scour depth.

- Two different regimes of propeller rotation are analyzed in this work: FWD and B & F rotation. B & F experiments aims at obtaining the scour evolution by iterating between backward and forward rotation, a behavior that is found in real ships when iterating berthing and unberthing maneuvers. In case of scour evolution near the Front Wall, differences are observed between the results obtained with the steady FWD rotation and the B & F iterations, being the results for the latter scenarios only dependent on the wall clearance and the time. FWD experiments allowed comparison with the empirical relations found in literature.

- Two empirical models are proposed in this paper to obtain the time dependent scour depth due to twin propellers in confined condition due to quay walls. The use of the proposed models must be restricted to the range of non-dimensional parameters used in the experiments. New experimental work is needed to evaluate the twin-propeller induced scour over different sediment sizes, also including different separations between the propeller axes.

- The threshold to scour is found to be dependent on the wall Froude number (Fr_w). At each time considered, a linear relation between the scour depth and the wall Froude number is found, agreeing all of them in a common threshold around $Fr_w \approx 0.25$, below which erosion is not found.

- A clear relation between the category of the profile (*merged*, *transition to merge* and *no-merged*) and the scour depth is found. A transition scour depth around the 15 % of the wall-clearance is observed in the present experiments, showing a threshold below which the scour profile maintains a two-hole morphology.

- Due to backward rotation, the scour hole exhibit a very different behavior. A very fast growing of the maximum depth is observed, and the stabilization is reached at $\approx$ 10 minutes of experiment. The maximum scour depths are used to obtain an empirical relation between the experimental variables and the equilibrium depth due to backward rotating twin propellers with interaction with a squared structure.

Chapter 4

AIS data and maneuver simulation to prevent bed scour in harbor environments

4.1 Introduction

International guidelines such as BAW (2010) and PIANC (2015) propose different prevention and protection systems against the scour induced by propellers in the navigation channel and the harbor basin. Predictive formulas are based on previous estimation of the efflux velocity (U_0) and the bed velocity (U_b), using Shields criteria as the threshold for resuspension. As reported by Mujal-Colilles et al. (2017b), most of the existing equations overestimate, by far, real results of maximum scouring depth. However, the methods proposed in these guidelines to design bed protections have been satisfactorily applied in plenty of harbors (PIANC, 2015), when the problem has been detected and managed in due time. Nevertheless, there is little information in literature and the guidelines regarding the relationship between the ship maneuver characteristics and its effects over the seabed. Some standard situations are defined in BAW (2010), that take into account the distance from the ship to a vertical boundary, or the presence of a rudder, but no general guidance including the maneuver pattern is present. In some communications, there is explicit mention of the most harmful maneuver situations. For instance, according to Hawkswood, Lafeber, and Hawkswood (2014), the most harmful maneuver section is the cast off, when the ship is stationary and accelerates to gain steerage. In this work, the authors also make explicit mention to the *crabbing* motion. They advise that no modeling studies are found in literature, but it is suspected that this specific maneuver may cause greater erosion depths. Crabbing is the ability of ships to move sideways without forward speed. In nautical terms it means that a specific ship has sway motion but no surge. This lateral motion is usually achieved by combining astern and ahead propellers with bow-thruster.

The work presented in this Chapter uses the methodology applied in Llull et al. (2020) in a case study, combining field data with a maneuver numerical simulator, to

analyze the maneuver pattern and take the engine behavior into consideration when studying the sediment scour at field. The field data consists on a series of bathymetric surveys performed at a specific harbor basin, where scour due to the maneuvers of a ferry ship was found. Moreover, AIS data is included to study and characterize the maneuver. AIS states for Automatic Identification System and is defined in IMO (1993) as an automatic tracking system for identification and location of vessels by exchanging data via VHF communication to other nearby vessels (Castells-Sanabra et al., 2018). The maneuver pattern is reproduced on a maneuver simulator, which allows to obtain the engine and thrusters behavior through the maneuver.

The present Chapter is organized as follows: In Section 4.2, the background of the study, the evolution of the harbor basin bed morphology, the statistics of use of the basin and the description study ship are included. In Section 4.3, the AIS data description, the maneuver simulator characteristics and the formulation used in this work, are provided. The results of the maneuver characterization, its relationship with the observed scour, the maneuver simulation and the obtained results when appliying the formulation are shown in Section 4.4. Finally, the above is discussed in Section 4.5, while the conclusions of this research and recommendations for further work are summarized in 4.6.

4.2 Case study: Barcelona Harbor

4.2.1 Background of the study

The present work arises from the background studies performed at an inner basin of the Port of Barcelona with significant problems related to ship propeller scour. This harbor basin has been traditionally used as large ferry ship berthing terminal. The research performed by Mujal-Colilles et al. (2017b) showed the evolution of the harbor basin from 2007 to 2014, and the work presented in Castells-Sanabra et al. (2018) extended the analysis up to 2017, highlighting the appearance of additional sedimentation areas nearby the berthing quay between 2015 and 2017. The mentioned studies are used as a benchmark of the present work, which is focused on the relationship between the ship maneuver, the propellers behavior and the induced scour.

4.2.2 Evolution of the harbor basin bed

The evolution of the bathymetry of the harbor basin between 2012 and 2017 is shown in the present section through yearly hydrographic surveys, performed with a multibeam system SeaBeam1185 Elac-Nautik. Figure 4.1 shows the evolution of the sediment bed through different bathymetries over time. The red line at the side quay indicates the berthing place of the study ship since 2012. This is called in advance the West-Quay. Previous to 2012, the study ship operated at the berthing quay nearby

(at the North-Quay). As explained in Mujal-Colilles et al. (2017b), the Port Authority decided to change the location after noticing the increasing problems they had due to propeller induced scour. Previous to the change, a dredging of the basin was performed to level all the sea floor, except in the affected area near the North-Quay. The evolution between 2012 and 2014 clearly shows the erosion effects of the scour over the unprotected harbor basin, from the West-Quay to the middle of the harbor basin (see Figure 4.1). At the time, the Port Authority decided to perform adaptation works in the affected area. The works consisted on the refilling of the affected regions with recycled material (20-300) up to the -14.5 m level. After that, the refilling material was covered by a rockfill layer with diameter 1 m, reaching therefore the -13.5 m level (*Annual Report* 2015). The bathymetry of 2015 is performed after the adaptation works finished and the one in 2017 shows that the protection is stable, although scour is present in the surroundings of the rehabilitated area.

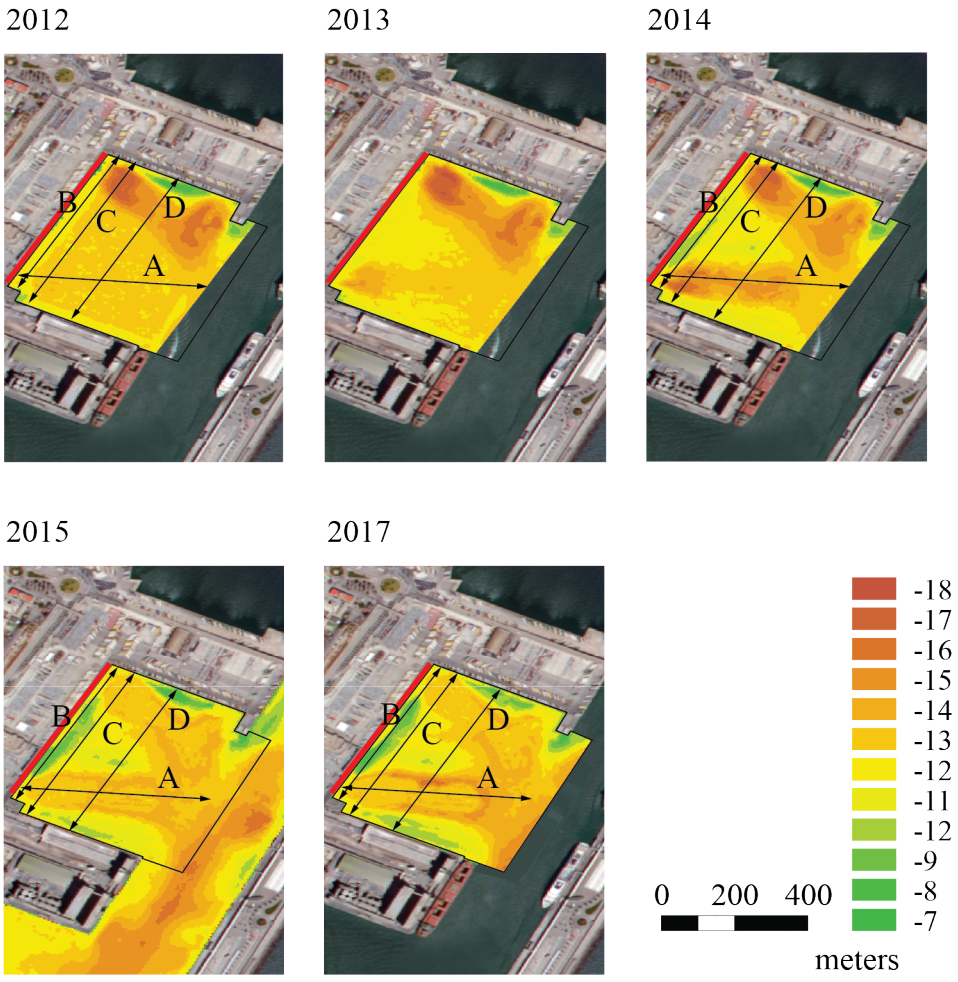

FIGURE 4.1: Bathymetric studies at the study basin performed since 2012 to 2017. The red line at the West-Quay shows the berthing location of the ferry ships at this basin during this time period. The black arrows show the interesting sections to obtain depth profiles from.

Scour is not the only problem that arises from the sediment transport due to the propeller jets action over the bed. The recirculation and the conditions of the particular basin may favor the appearance of sedimentation areas that can reach dangerous low depth, affecting the ship maneuvers. In the central area of the study quay (West-Quay) a sedimentation area is created in the middle of the berthing place, reaching a depth similar to the ship's draught (around -7 m) between 2015 and 2017 (Figure 4.1).

The black arrow-lines and the letters (A to D) in the bathymetries in Figure 4.1 correspond to elevation profiles measured over the Digital Elevation Model (DEM). The profiles are shown in the Figure 4.2, to compare the evolution of the main interest areas through the years. The elevation profiles are taken from South to North and from West to East. In 2014, the higher scouring area, reaching -18 m, is located nearby the West-Quay (Figures 4.2 (a) and (c), corresponding to profiles A and C in Figure 4.1). After the works in 2015, no scour is observed in this area. The other derived problem from the propeller jets action is the sedimentation of the eroded material. Between 2015 and 2017 the sedimentation in the parallel profile to the berthing quay increased significantly, almost reaching the -7 m level (see Figures 4.2 (b) and (c), corresponding to profiles B and C in Figure 4.1). In Figure 4.2 (b) -profile B-, two accretion areas are clearly distinguishable, separated by an area of no sedimentation between 150 m and 250 m from the back quay. This distance is in fair agreement with the location of the bow-thrusters, between the ship's bridge and the ship's bow, when the ship is berthed. This will be analyzed in detail in Section 4.4. The profiles A and D, corresponding to Figure 4.2 (a) and (d), show the existence of scour in the surroundings of the rehabilitated area. Depth increases between 2015 and 2017 are observable at profile A, at a distance of 370 m from the West-Quay, and at profile D, at a distance 150 m from the South-Quay. These distances correspond to the North and East boundary of the protected area. These effects, although present, are of considerable lower magnitude compared to the scour over the unprotected bed found in previous years. Although reaching -16 m depth, meaning 2-3 m below the design depth of the protection, the affected area is considerably smaller area than the eroded area in 2014 at the same location. Still, the evolution of the sediment volume in the inner basin (the area bounded by black solid lines in Figure 4.1), calculated from the DEM, shows an increase of 3.5 % of sediment volume above the reference level -12 m, and a decrease of 7.4 % below the same reference level, between 2015 and 2017. This means that part of the eroded sediment is transported and deposited in other areas inside the basin, while a part of it is lost out of the basin and may create sedimentation problems in other areas of the port.

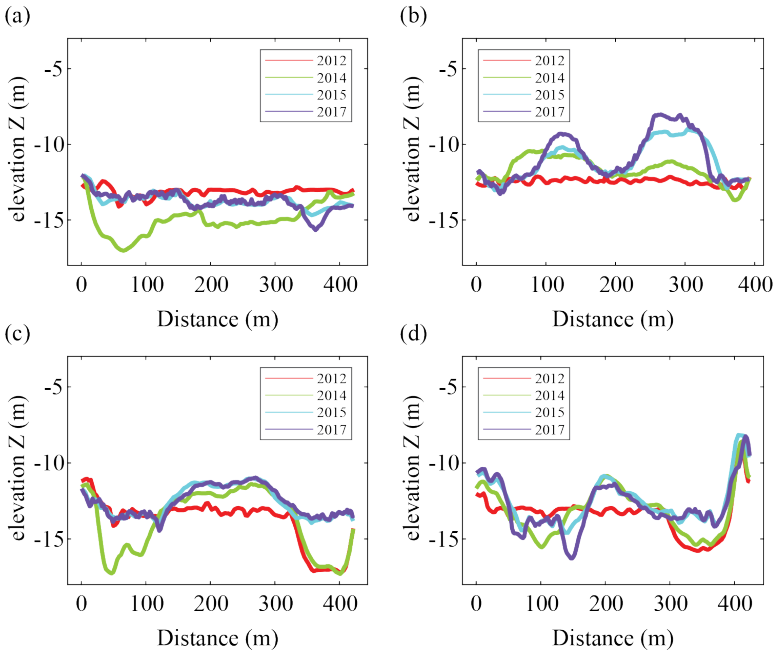

FIGURE 4.2: Elevation profiles obtained from each bathymetry in Figure 4.1 at two-years time intervals. (a): Profiles A in Figure 4.1; (b): Profiles B in Figure 4.1; (c) Profiles C in Figure 4.1; (d): Profiles D in Figure 4.1

4.2.3 Use of the harbor basin

This section presents the statistics of use of the study dock between 2013 and 2017. The data, including every single ship call, the date of each call (arrival and departure), the ship type and characteristics of the ship (length and Gross Tonnage), has been provided by the statistics department of the Port of Barcelona. In Figure 4.3, histograms of the ship type, characteristics and number of calls per week are shown. According to the statistics of use of the study dock between 2013 and 2017, the characteristic ship to study is a Ferry ship type, with 225 m in length, close to 55000 GT (Gross Tonnage), and with berthing frequency of 6 times per week. These are, indeed, the characteristics of the twin ships with a frequency of 3 calls per week each, that operate alternating at the study quay and are focus of the present work. This berthing quay is used eventually by other ships, as seen in the histograms, but all of them are of smaller size and load capacity, which indicates lower engine power and lower potential effects over the basin sediment bed.

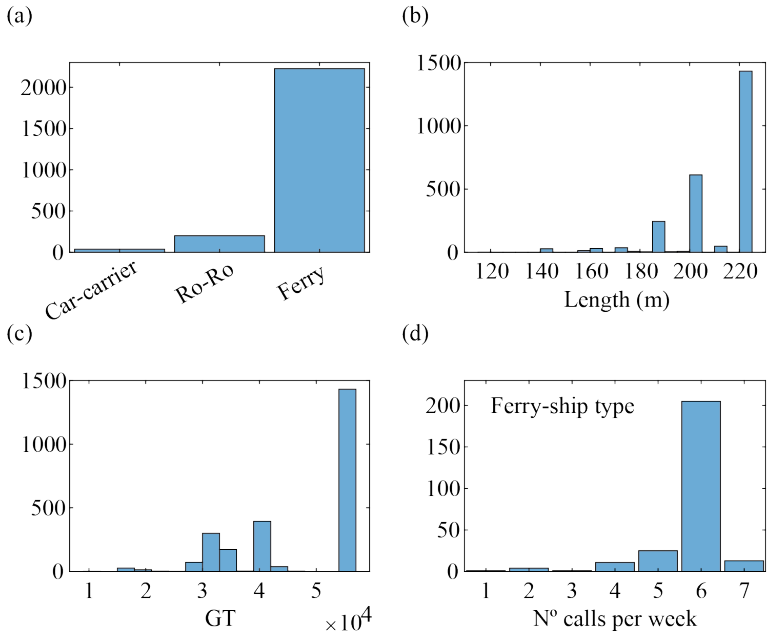

FIGURE 4.3: Statistics of berthing ships in the study quay between 2013 and 2017. (a) Ship-type; (b) Ship length; (c) Gross Tonnage (GT); (d) Number of calls per week.

4.2.4 Ship particulars

A set of twin ships is used as a study ship in this work, since these are the ships operating at the harbor basin during the last 10 years. These vessels operate with daily basis (either one or the other) at the same harbor, performing the same maneuvers in the same conditions. A sketch showing the main dimensions of the study ship is shown in Figure 4.4, adapted from Castells Sanabra et al. (2017). In Table 4.1, the characteristics of the twin ships are shown under the generic name of *Study Ship*. The study ship was lengthened in 2019 (one of the twin ships in January and the other in June), therefore the current characteristics of the ship are not exactly the same than in the period 2012-2017. These changes are shown in Table 4.1 by comparing the characteristics before and after the lengthening.

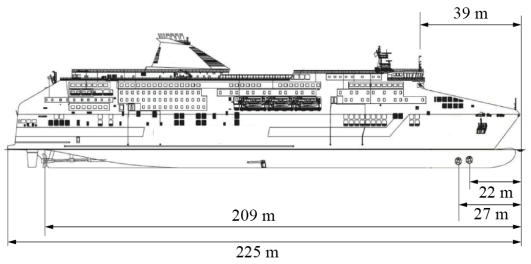

FIGURE 4.4: Dimensions of the study ship and distances to locations of interest. Adapted from Castells Sanabra et al. (2017).

TABLE 4.1: Study ship characteristics.

	after 2019	before 2019
Name	Study Ship	
Length overall	254 m	225 m
Draught	7.2	7 m
Breadth Moulded	30.4 m	
Gross Tonnage	63742 GT	54900 GT
Main Engine Power (kW)	4 x 13860 kW	
Thrusters Power	2 x 1850 kW	
Propeller type	2 x CPP (148 rpm)	
Propeller Diameter	6 m	
Bow-thrusters Diameter	2.2 m	

4.3 Methodology

4.3.1 AIS data

In this work, AIS data provided by the Barcelona Port Authority, containing the ship position (latitude and longitude), the Speed Over Ground (SOG), and the ship Heading (HDG) at time intervals of 30 seconds is used. The data set selected to study the ship maneuver consist on 15 arrival and departure maneuvers, with similar met-ocean conditions. This data set was already presented in Castells-Sanabra et al. (2018) and will be used in this work to validate more recent data obtained from the same ship at the same basin. This AIS data set is named as AIS1 through the document.

An AIS transmitter was recently adapted to directly obtain AIS data from nearby ships at the Barcelona School of Nautical Studies (FNB-UPC). The new system allows to directly receive AIS messages from all the ships in the surrounding area of Barcelona (up to 30 nautical miles, with a maximum range of 120 nautical miles, weather permitting). AIS data of 2019 (September to December, both included) is used to verify that the old maneuvers barely changed, confirming that the maneuvers must have a cumulative effect on the bed scour. All the maneuvers performed by the study ship in this period are included. This data set, named as AIS2 through the document, together with AIS1 data set, is used herein to characterize the ship maneuver in the study basin.

The accuracy of the data provided by the Port Authority (AIS1 data) is of ± 14 m, while in the case of the directly obtained data by the AIS at the (FNB-UPC) (AIS2 data) an accuracy of ± 8 m is expected, after test measurements with a signal at a fixed location.

4.3.2 Maneuver simulator

The Barcelona School of Nautical Studies (FNB, UPC) hosts a Transas NTPro 5000-v-5.35 maneuver simulator designed to be used for pilot and captain training, in naval engineering and port management (Figure 4.5). By using this simulator, the recorded maneuvers from AIS messages are reproduced to obtain the specific behavior of every necessary variable to estimate the scouring action. The harbor, the study ship and the AIS data are inputs known in the simulator. The specific study ship was not available and therefore, a ferry ship type with similar characteristics was used. Table 4.2 shows the details of the ship used in the simulator under the name *Simulator Ship*. The *Study Ship* is slightly larger than the *Simulator Ship* (up to 13 %) with larger capacity, but these little differences are not considered to have any significant effects on the arrival and departure maneuvers characteristics.

FIGURE 4.5: Picture of the maneuver simulator. Adapted from Amengual (2019).

TABLE 4.2: Simulator ship characteristics.

Name	Simulator Ship
Length overall	196 m
Draught	6.1 m
Breadth Moulded	25 m
Main Engine Power (kW)	50400 kW
Thrusters Power	3400 kW
Propellers depth	3.8 m

To perform any maneuver in the simulator, the maneuver track is first introduced in the electronic nautical chart (ECDIS -Electronic chart display and information system-) of the simulator to guide the simulator pilot during the whole maneuver.

TABLE 4.3: Summary of the simulator output.

	Variable	Units
Ship behavior	Geographical position	Lat, Lon
	Heading (HDG)	Degrees
	Speed Over Ground (SOG)	Knots
	Maneuver time	Seconds
Engines behavior	Main engine power	kW
	Bow-thrusters power	kW

Important information such as the Speed Over Ground (SOG), Heading (HDG) or maneuver time at each way-point can be included to provide good guidance to the pilot. The maneuver is performed smoothly and non-stop until the vessel berths (arrival maneuver) or departs the basin (departure maneuver). After the simulation is finished, the recorded parameters at 1Hz sampling rate are printed on a spreadsheet and are evaluated. The output of the simulator can include a plenty of parameters (e.g., ship engine behavior, dynamic ship behavior, meteorological records, etc.). For the purpose of this work, only few variables, as summarized in Table 4.3, are needed. The maneuver is repeated until the result is considered to be satisfactory to the purposes of the study.

4.3.3 Literature formulae

From the output of the simulator, the existing formulae to characterize the efflux velocity (U_0) and estimate the magnitude of the maximum bed velocity (U_b) are applied. In this work, the equations are all applied according to PIANC (2015) recommendations, which takes into account the characteristics of the study case: twin propeller ferry ship with bow-thursters and twin rudders, in a low bed clearance situation, with a combination of confined jet flow due to quay walls and unconfined flow conditions.

In order to analytically evaluate the propeller induced velocities at the seabed of a particular harbor basin, U_0 is firstly obtained with Eq. 4.1, as proposed by Blaauw and Kaa (1978) and recommended by PIANC (2015). In this case, the percentage of total power used by each engine (f_p) is the output of the simulator.

$$U_0 = C_1 \left(\frac{f_p P}{\rho_w D_p^2}\right)^{\frac{1}{3}} \tag{4.1}$$

where:

U_0 = Efflux velocity (ms^{-1})
f_p = Percentage of total installed power used (-)
P = Total installed power (W)
ρ_w = Water density (kgm^{-3})
D_p = Propeller diameter (m)
C_1 = 1.48 or 1.17 in case of free or ducted propellers and thrusters, respectively.

Since the ship is in constant motion during the maneuver, the generated jet needs to be analyzed together with the geometry of the study quay and the maneuver itself. Two different flow conditions are considered to obtain the induced flow velocity at bed: *confined* and *unconfined* flow. The confined flow refers to the case in which the jet flow reaches the quay wall and deflects on it, thus affecting the seabed due to the previous impingement. The unconfined flow, contrarily, refers to a spreading jet flow that reaches the seabed due to its own expansion. This condition is important to decide which formulation must be applied at any time of the maneuver. In this work, a threshold based on the location of the maximum velocity at the bottom is used to define the *confined* or *unconfined* condition of the ship through the maneuver. In PIANC (2015), the position to the maximum velocity at bed is assumed to be at $0.12 < C_h/X_{mu} < 0.22$ in case of unconfined flow condition, where C_h is the propeller's bed clearance and X_{mu} is the horizontal distance to the position of the maximum velocity at bed. A threshold distance of $C_h/X_w = 0.18$ is assumed to define the *confined* or *unconfined* situation at any maneuver position, with X_w being the horizontal distance from the propellers plane to the quay wall. If $C_h/X_w > 0.18$, then the situation is set to confined. To double check the potential scour at the quay wall, the results obtained in Chapter 3 of this dissertation will be used in this Chapter. A threshold of scour in case of twin propeller systems at low bed clearance conditions, i.e., $1D_p < C_h < 1.5D_p$ is found at $Fr_w \approx 0.25$, with $Fr_w = U_0/\sqrt{gX_w}$. The last will be obtained at any position of the ship, considering the previously obtained U_0 and the distance to the quay wall. This distance, X_w, is calculated at any position, from the propellers plane to the quay wall, with the ship's Heading vector. The position of the main propellers is known to be around 170 m astern of the AIS transmitter position, previous to 2019. In combination with the ship's Heading vector, and using the distance as vector modulus, the position of the main propellers during the whole maneuver and the axial distance to the quay wall are computed at any time during the maneuver.

The maximum flow velocity at the seabed is computed with the German and Dutch methods, as recommended in PIANC (2015). The expressions in these guidelines (Eqs. 4.2, 4.3, 4.4 4.5, 4.6 and 4.7) are used to obtain an estimation of the magnitude of the flow velocity at the seabed, depending on the confinement scenario. In Table 4.4, a summary of the equations is provided, together with the method (Dutch or German) and the conditions (propeller type and jet flow confinement) they are

recommended for. Although the expressions proposed for the confined flow scenario (Eqs. 4.2 and 4.5) are recommended for bow-thrusters rather than main propellers, the same expressions are used herein for the case of confined flow with main propellers, since there is no explicit formulation for this case in the guidelines.

TABLE 4.4: Set of equations to obtain the maximum velocity at bed (PIANC, 2015).

Method	**Propeller system**	**Jet confinement**	**Equation**	
Dutch Method	Single	Confined	$U_b = 2.8U_0(\frac{X_w + C_h}{D_p})^{-1}$	(4.2)
Dutch Method	Single	Unconfined	$U_b^{single} = 0.216U_0(\frac{C_h}{D_p})^{-1}$	(4.3)
Dutch Method	Twin	Unconfined	$U_b^{twin} = U_b^{single}\sqrt{2}$	(4.4)
German Method	Single	Confined	$U_b = 1.9\alpha U_0(\frac{X_w}{D_p})^{-1}$	(4.5)
German Method	Single	Unconfined	$U_b^{single} = 0.71U_0(\frac{C_h}{D_p})^{-1}$	(4.6)
German Method	Twin	Unconfined	$U_b^{twin} = 0.52U_0(\frac{C_h}{D_p})^{-0.275}$	(4.7)

where:

U_b = Flow velocity at bed (ms^{-1})
X_w = Distance from the propellers plane to the quay wall (m)
C_h = Propellers bed clearance (m)
α = Constant depending on L/D_p and C_h/D_p with range $1 < \alpha < 8$

The twin-propeller system of the study ship allows the Captain to combine ahead and astern regime at the same time during the maneuver. This combination, together with the bow-thruster, allows great maneuverability, and is commonly used during ferry ships maneuvers. As stated in the Introductory section of this dissertation, this

is the engine orders combination that allows the ship to crab (*crabbing* motion).

During the maneuver, if only one propeller is used in ahead regime, the equations for single propeller are applied. On the other hand, when both propellers are used ahead, the equations for twin propeller are applied. The formulae is only applied to ahead running propellers. It is known, however, that backwards rotation may also induce high velocities at the bed, but so far there are no recommended formulation in the guidelines to obtain the velocity at bed in this condition. Therefore, the propeller jet velocity due to propellers in astern regime won't be computed. The propellers behavior in astern regime, however, will be considered when analyzing the power output from the simulator.

4.4 Results

Characterization of the maneuver pattern

Real maneuvers obtained by AIS1 and AIS2 data sets are categorized as *arrival* and *departure* maneuvers, and mapped to show the maneuver pattern of the study vessel. Due to the lengthening of the ship in 2019, the two data sets cannot be directly compared. Therefore, the AIS2 data has been corrected with a displacement of the AIS transmitter position 29 m astern. The correction is done using the ship's heading vector, also provided by the AIS messages.

In Figure 4.6 (a) and (b), AIS2 corrected data set is mapped. Each color represents a different maneuver, this is, a different day. The days are not included as legend to avoid overlapping due to the big amount of maneuvers in the plot. The exact day of the maneuver is not of main interest, since the objective of plotting all the data together is to observe the maneuver pattern. All the maneuver characteristics are coincident, with due consideration of the arrival (a) and departure (b) maneuvers. A scaled ship sketch is added in the maps to provide a clear understanding of the maneuver in the study basin. Three points of interest are also added in the maps, showing that the maneuver is split into three sections (Maneuver Sections MS1, MS2 and MS3), to analyze the ship behavior between the points. Each point contains a letter (A or D) that defines the maneuver sections in case of arrival (A) or departure (D) maneuvers. Therefore, each maneuver section is named combining the acronym MS, the point of interest (1,2,3) and the letter to define the arrival or departure maneuver (A, D).

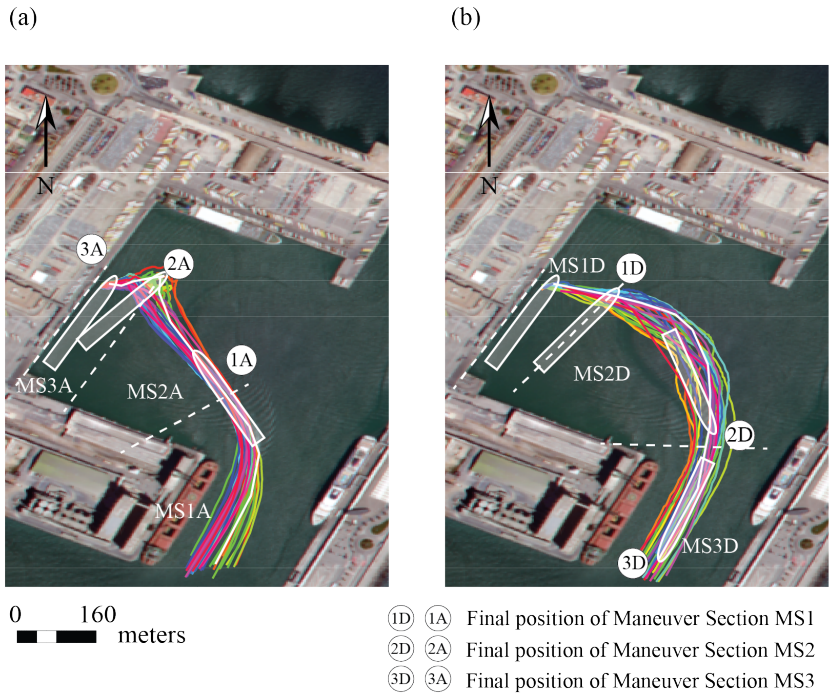

FIGURE 4.6: Maneuvers of the study ship between September 2019 and December 2019 (AIS2 data). The numbers in the legend show the positions of interest in the maneuvers.

Figure 4.6 (a), shows the arrival maneuver of the study ship. The study ship enters the harbor basin from the navigational channel by turning to the port side, with a NNW Heading (Point 1A). The ship advances while describes a starboard turn up to Heading NE (Point 2A). Finally, by approaching the side quay laterally, the ship reaches the point 3A and berths.

In Figure 4.6 (b), the departure maneuver is shown describing a simpler behavior. First, the ship moves away from the berth laterally, until reaching the turning position (Point 1D). At this point, the ship turns to the starboard describing a circular trajectory up to Heading South (Point 2D). Right after that, the ship finishes the turn and departs the port with Heading SW (Point 3D).

To allow the comparison between AIS1 and AIS2 data sets, the last is mapped with transparency below the former in Figure 4.7. Since AIS2 contains a much bigger amount of maneuvers, the accumulation of AIS positions allow to visualize the maneuver pattern and show the good agreement with AIS1 data, plotted above and colored by maneuver. Because of this, any of the data sets are suitable to be used to characterize the maneuver, regardless of the time period the data was taken from. Slight changes due to the differences on the ship size and Captain must be expected, but they are not considered to be relevant to the general maneuver pattern as per the observed results.

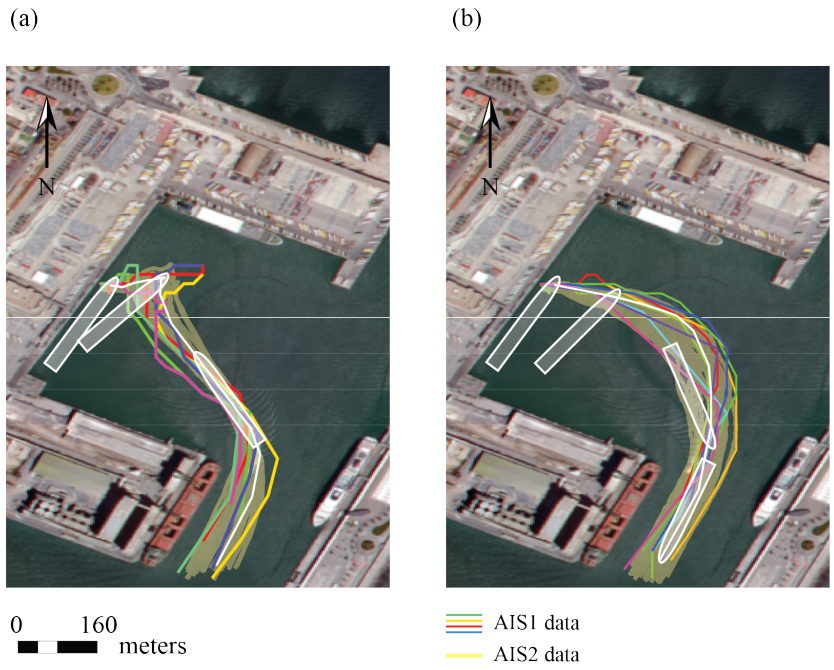

FIGURE 4.7: AIS1 data (colored lines) over AIS2 data.

Relationship between erosion pattern and ship maneuver

In order to overlap the ship maneuver to the erosion pattern, the last bathymetry available in the data set (2017) is used. To allow a more detailed visual analysis, the DEM shown in Figure 4.1 (2017) is converted to a Triangulated Irregular Network (TIN). In Figures 4.8 and 4.9, TIN are mapped both with the maneuver data over it (a) and without it (b) to allow comparison. The data includes the propellers location, obtained according to the ship's Heading at each AIS position. Figure 4.8 (a) shows the data corresponding to the arrival maneuvers. The AIS track is plotted in red dots, while the propellers location is plotted with a single white dot. The coincidence between the propellers positions through the maneuver and the eroded area is clear, being the affected area constrained to the region below the propellers during the whole maneuver. In Figure 4.8 (b), three locations of main interest are shown: (1) the area of protected bed, where the adaptation works described in 4.2.2 were performed; (2) the scour areas surrounding the protection layer; (3) the sedimentation area at the West Quay.

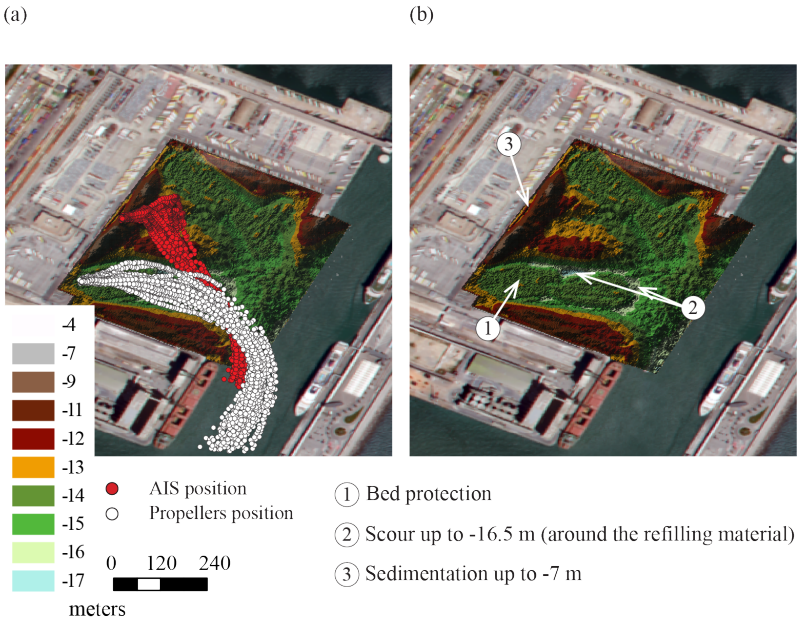

FIGURE 4.8: (a) AIS2 data of arrival maneuvers over TIN surface; (b) Only TIN surface showing the location of the areas of interest 1,2 and 3.

Figure 4.9 (a) shows the AIS data of the departure maneuvers with the propellers position. In this case, only the first part of the maneuver, corresponding to the unberthing lateral movement of the ship (i.e., MS1D in Figure 4.6), shows agreement with the affected area. The propellers positions during this part of the maneuver are coincident with the propellers positions during the arrival maneuver close to the quay wall (i.e, MS3A in Figure 4.6). However, the positions of the main propellers during the turning maneuver are not in agreement with the location of the eroded area, leading to the hypothesis that this maneuver may be less harmful than the arrival one. This could be caused by the higher importance of the bow-thrusters during this maneuver, which are used to induce starboard turning moment during the unberthing (i.e., MS1D and MS2D in Figure 4.6). The position of the bow-thrusters during the maneuver is not plotted, to avoid overlapping data points. However, as shown in the study ship sketch in Figure 4.4, they are located at 12 m and 17 m from the AIS transmitter, towards the bow of the ship. During MS1D (departure maneuver beginning), lateral displacement of the ship is needed to get off the side quay, meaning that the bow-thrusters are used to generate starboard thrust. Therefore, the bow-thrusters jets are directed towards the quay wall, at the location of the point 3 in Figure 4.9 (b), i.e., the area of sedimentation with a characteristic gap at a distance of 200 m from the SW corner (see the elevation profiles in Section 4.2.2, Figure 4.2).

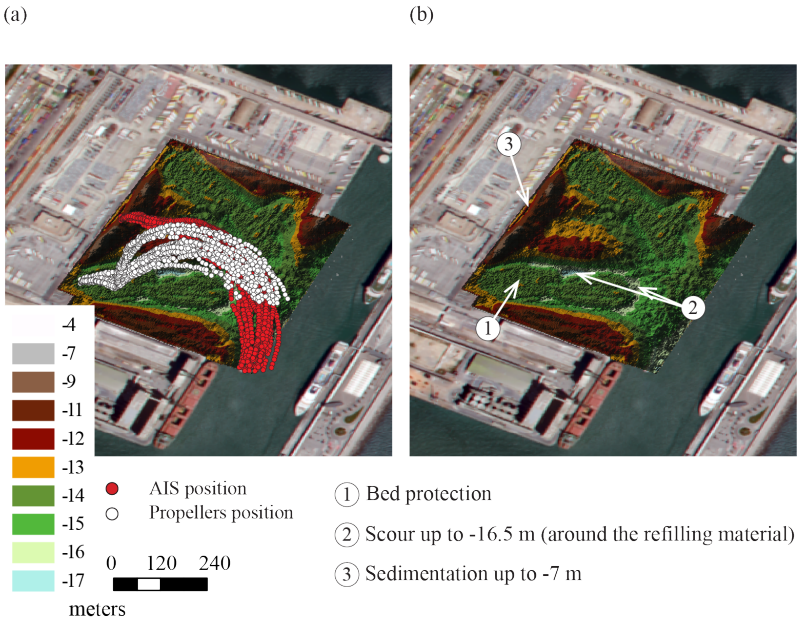

FIGURE 4.9: (a) AIS2 data of departure maneuvers over TIN surface; (b) Only TIN surface showing the location of the areas of interest 1,2 and 3.

Maneuver simulation

After the maneuver analysis, each arrival and departure maneuver are repeated in the simulator several times to get a similar pattern than the observed one. The slight difference in the ship type, the human errors and the limitations of the simulator need to be considered at this point. However, a very close behavior is obtained if the maneuver is repeated several times. In Figures 4.10 and 4.11 the arrival and departure maneuver obtained from the simulator are shown, respectively, compared to AIS2 data. In Figures 4.10 (a) and 4.11 (a) the AIS position of the simulator ship is plotted by Heading arrows, showing the ship's Heading at each AIS position. Some differences between the AIS data and the simulator maneuvers are observable by visual comparison, although they are not considered to be relevant to the mean behavior of the engines, which is the main focus of this work. For instance, a small deviation is observed in the arrival maneuver, during the port side turn at the beginning of the maneuver (Figure 4.10 (b)), and the main propellers position at the first stages of the departure maneuver show a slight disagreement between the AIS data and simulator data (Figure 4.11 (a)).

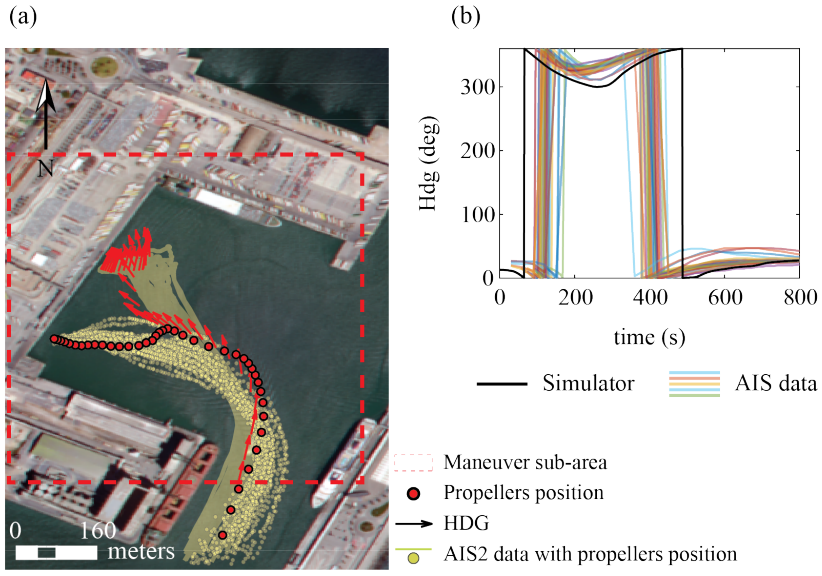

FIGURE 4.10: Arrival maneuver. (a) Simulator maneuver's Heading arrows (red arrow lines) and propellers position (red dots) over AIS2 data; (b) Time-series of the ship's heading obtained from the maneuver simulator (black lines) and from AIS data (colored lines).

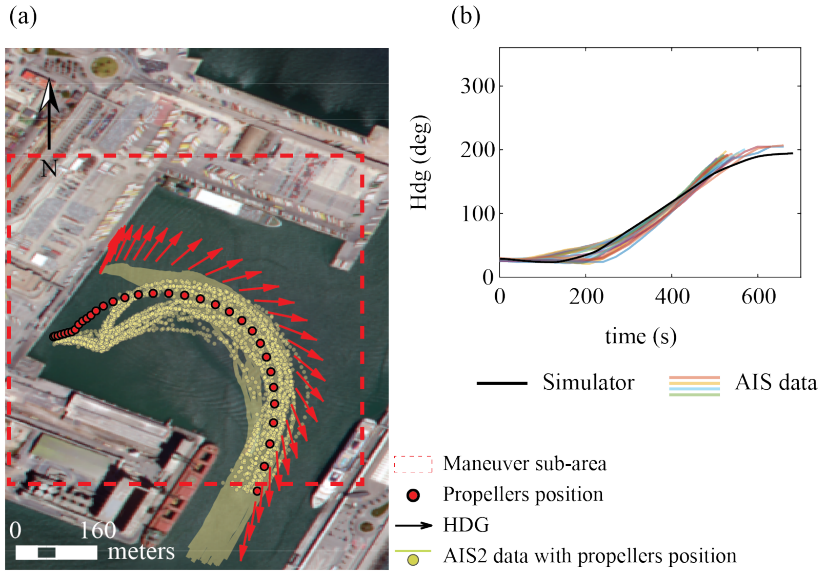

FIGURE 4.11: Departure maneuver. (a) Simulator maneuver's Heading arrows (red arrow lines) and propellers position (red dots) over AIS2 data; (b) Time-series of the ship's heading obtained from the maneuver simulator (black lines) and from AIS data (colored lines).

A comparison of the time-series of the maneuver descriptors is useful to validate the maneuver. As in Llull et al. (2020), the Heading is found to be the best descriptor, since it clearly shows the behavior of the ship with time, allowing to compare the ship behavior at any time of the maneuver together with the total duration of the maneuver. Time-series of the AIS maneuvers and the simulator maneuvers are

therefore compared and shown in Figures 4.10 (b) and 4.11 (b). A common reference time is needed, so each maneuver time is re-scaled to fit a common time by cross-correlating each AIS maneuver with the simulator maneuver. A re-sampling of every signal to 1 Hz (the same sampling rate obtained in the simulator) is done by spline interpolation. Note that the maneuver is in this case considered within the dashed sub-area showed in Figures 4.10 (a) and 4.11 (a). After the maneuver validation, the engine behavior obtained from the simulator maneuver can be used as an estimation of the real usage of the engines during the maneuver, to obtain the main relevant parameters governing the scour phenomenon.

Main engines and bow-thrusters use during the maneuver

According to Figure 4.6, three points of interest are defined to split each maneuver (Arrival and Departure) into three Maneuver Sections, and analyze each one separately. The engine behavior is shown herein according to the Maneuver Sections MS1, MS2 and MS3, bot for Arrival (MS1A, MS2A and MS3A) and Departure (MS1D, MS2D, MS3D) maneuvers. Within these sections, the engine orders show no significant changes, therefore a mean engine regime (main propellers and bow-thrusters) is obtained. Figures 4.12 (a) and 4.13 (a) show the ship maneuver pattern by Heading vectors and the main propellers location at each ship position, colored by Maneuver Section. The propellers position obtained from the AIS data is included to better guidance. Figures 4.12 (b), (c) and 4.13 (b), (c), show the main engine (b) and bow-thrusters (c) behavior, also colored by Maneuver Section.

According to the points of interest in the bathymetry, defined in Figures 4.8 and 4.9, the behavior of the engines during Maneuver Section MS2A, MS3A and MS1D is of main interest. In case of MS3A and MS1D, these Maneuver Sections correspond to the final stages of the arrival maneuver and the initial stages of the departure one, respectively. During these Maneuver Sections, the main propeller system is located over the erosion pattern near the quay wall, and the bow-thrusters are located above the sedimentation area at the West Quay. In case of MS2A, the main propellers follow the erosion pattern along the harbor basin, therefore the main engine regime is of main interest.

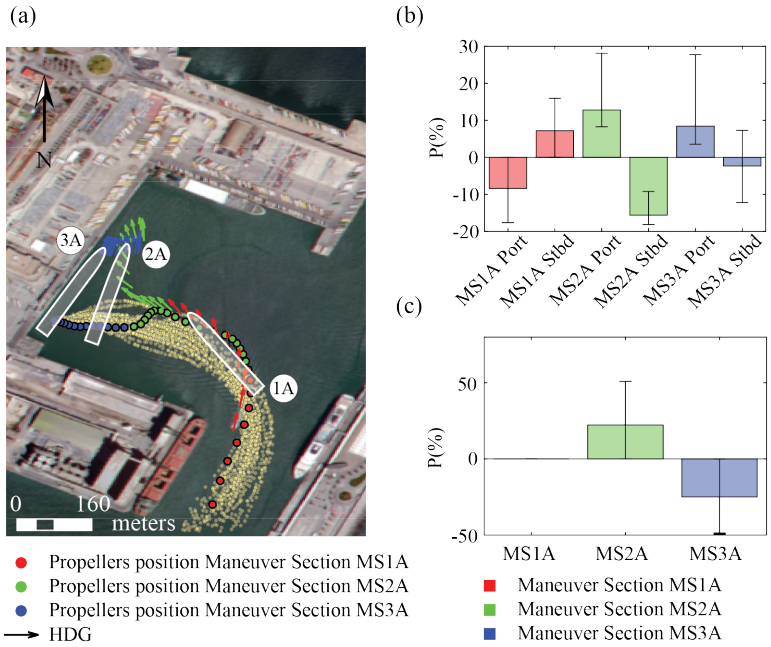

FIGURE 4.12: (a) Simulator maneuvers showing the AIS position with heading arrows and the propellers position, colored by Maneuver Section (sections MS1, MS2 or MS3); (b) Main propellers: Percentage of installed power used at each Maneuver Section; (c) Bow-thrusters: Percentage of installed power used at each maneuver section. Error bars show minimum and maximum value.

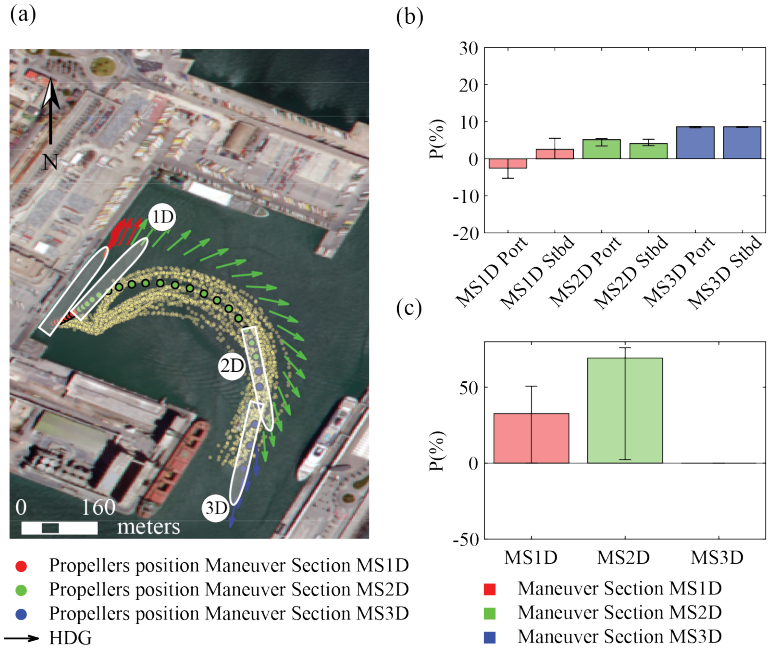

FIGURE 4.13: (a) Simulator maneuvers showing the AIS position with heading arrows and the propellers position, colored by Maneuver Section (sections MS1, MS2 or MS3); (b) Main propellers: Percentage of installed power used at each Maneuver Section; (c) Bow-thrusters: Percentage of installed power used at each maneuver section. Error bars show minimum and maximum value.

The arrival maneuver, Figure 4.12, begins when the ship enters the harbor basin, combining astern port engine and ahead starboard engine to induce a port side turning moment to the vessel (Figure 4.12 (b), MS1A). Right after, to approach the stern of the ship to the quay wall, the main propellers behavior is inverted, and port propeller runs ahead while starboard propeller runs astern (Figure 4.12 (b), MS2A). This combination is maintained during the rest of the maneuver, i.e., during MS2A and MS3A. The motion of the ship is mainly sideways and no significant advance velocity is observed during these Maneuver Sections (i.e., crabbing motion). During MS2A, the bow-thrusters are used to place the ship in parallel with the West-Quay (Figure 4.12 (c), MS2A), i.e., starboard thrust. On the other hand, during MS3A, the bow-thrusters regime are inverted and they are used to induce port thrust and approach the ship to the West-Quay horizontally (Figure 4.12 (c), MS3A). The behavior of the bow-thrusters near the berthing place during the arrival maneuver indicates that the jet flow is not directed to the side quay-wall at this part of the maneuver. During the arrival maneuver, the higher percentage of engine power is used in MS2A, which is also the area of interest due to higher propeller scour. The mean percentage of installed power is around the 15 %, both in ahead and astern regime.

The departure maneuver, Figure 4.13 , starts with the lateral crabbing motion to separate the ship from the berthing quay. To move laterally, the bow-thrusters is used inwards, i.e., starboard thrust and jet directed to the West-Quay. This behavior is observed in the bar-plot in Figure 4.13 (c), MS1D. The mean percentage of power used at this Maneuver Section by the bow-thrusters is around the 40 %. Since the jet is directed to the West-Quay, this Maneuver Section is expected to cause the scour pattern observed in the elevation profile parallel to the West-Quay, between 150 m and 250 m from the South-Quay (see Profile B in Figure 4.1 (2017) and Figure 4.2 (b) (2017)). Therefore, this area is an area of sedimentation, but locally eroded by the bow-thrusters jet during the departure maneuver, at the Maneuver Section MS1D.

During MS1D, the main starboard propeller works in ahead regime while the main port propeller works in astern regime (Figure 4.13 (b), MS1), at low engine orders ($\pm$5% of the installed power). Once the vessel is separated from the side quay, the turning begins, increasing the delivered power of the bow-thrusters, Figure 4.13 (c), now farther from the West-Quay. The main engines are used in ahead regime during this Maneuver Section, to induce ahead thrust. Firstly, only the port engine is used, and later both engines runs at the time, when the turning is almost finished. This maneuver section extends until the departure heading is reached, at Maneuver Section MS3D (blue dots and arrows in Figure 4.13 (a)). At this time, both propellers run ahead at a 10 % power, with no need of bow-thrusters, and the ship departs the harbor basin. At the departure maneuver, lower engine power than at the arrival one is needed. In this case, the simulator output yielded a maximum percentage of installed engine power lower than the 10 %, both astern and ahead.

Considering the formulae presented in Section 4.3.3 and the results yielded by the maneuver simulation, the efflux velocity of each propeller at any time can be obtained. As explained, the formulation is limited to forward rotating propellers, meaning that in case of the departure maneuver, the astern rotating propeller in Maneuver Section MS1D cannot be considered. In the same way, the astern rotating propellers in Maneuver Sections MS1A, MS2A and MSA3 are not included in the velocity computation. During the arrival maneuver, the propellers location is coincident with the erosion pattern at the Maneuver Section MS2A, in which both ahead and astern engine power are used.

The efflux velocity obtained at any time during any maneuver yielded maximum values close to 10 ms^{-1}, and average values between 4 and 6 ms^{-1} (see Figure 4.14 (a) and (b)). The highest values are obtained during MS2A and MS3A, at the arrival maneuver. Mean values of 6-7 ms^{-1} and maximum values of 10 ms^{-1} are computed from the simulator output. However, due to the inner limitations of the formulations present in literature, this computation does not consider the effects of the propeller in astern regime. During the departure maneuver, the maximum efflux velocity is obtained at MS3D, when both the propellers run ahead and the ship is about to leave the harbor basin. At this point, the percentage of engine power used is about the 10 % and the efflux velocity is close 6 ms^{-1}, in this case with both propellers ahead. In the inner part of the basin (i.e., MS1D and MS2D) the obtained values of efflux velocity are lower: 5 ms^{-1} in both Maneuver Sections, with just one propeller ahead in MS1D and both of them ahead in MS2D.

The estimated bed velocity (U_b) is one of the needed inputs to the equations used in bed protection design. For instance, in (Blokland and Smedes, 1996), Isbash criterium ($\beta_{is} > \beta is, cr$) is used (Eq. 4.8) to determine the bottom stability. In their work, Shields criterium ($\Psi < \Psi_{cr}$) is also used (Eq. 4.9), after determining an empirical friction coefficient based on the measured transport intensity. Both of the methods depend on the computation of the U_b, which is computed in this work with the expressions in Table 4.4, depending of the maneuver conditions at each Maneuver Section. The results are shown in Figure 4.14.

With these results, the input parameters for Eqs. 4.8 and 4.9 can be computed. An example of the computation of the stability of the bed is considered interesting to the present work, using the obtained results from the maneuver simulation. The results obtained at the Maneuver Section MS2A are used in this example, because higher loads are expected in this Maneuver Section (see Figures 4.6 (a) and 4.8). The adaptation works in 2015 were performed in this area (see Section 4.2.2) and bottom protection of material 20-300 was used to protect the bottom. In this case, $D_{50} = 160$ mm and $\rho_s = 2600$ kgm^{-3} are used as approximate values. The friction coefficient

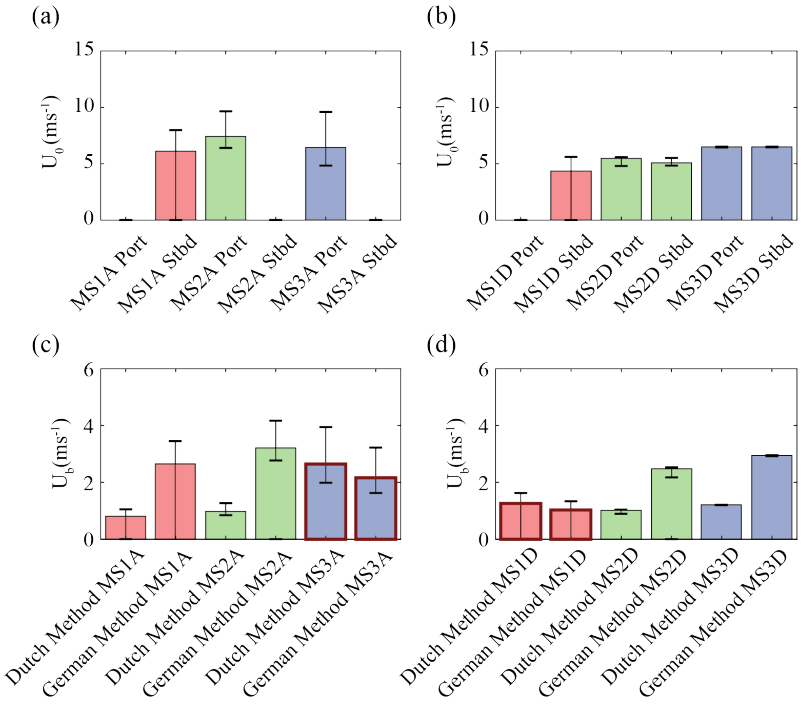

FIGURE 4.14: (a) and (b): Efflux velocity (U_0); (c) and (d) Velocity at bed (U_b), at each maneuver section. (a) and (c) Arrival maneuver; (b) and (d) Departure maneuver.

obtained in Blokland and Smedes (1996) ($0.1 < C_f < 0.15$, therefore $C_f \approx 0.13$) is used herein, to compute the shear stress with Eq. 4.10. Also according to the work in Blokland and Smedes (1996), the velocity at bed is computed with the Dutch method (see Table 4.4, Eq. 4.3). As per the information provided in Section 4.2.2, the bottom protection was located at -13.5 m depth, therefore a C_h = 9.5 m is used herein, considering the propellers depth. The results are summarized in Table 4.5. If common values in literature are chosen as critical parameters ($3.3 < \beta is, cr < 5$ and $\Psi_{cr} \approx 0.03$) the bottom material is expected to be mostly stable, but with "occasional movement" (Blokland and Smedes, 1996).

$$\beta_{is} = \frac{2g\Delta D_{50}}{U_b^2} \tag{4.8}$$

$$\Psi = \frac{\tau}{\rho g \Delta D_{50}} \tag{4.9}$$

$$\tau = \frac{1}{2} C_f \rho U_b^2 \tag{4.10}$$

Both arrival and departure maneuver close to the West-Quay are considered to be in confined situation, since the propellers are most of the time over the threshold established in this work ($C_h/X_w > 0.18$ and $Fr_w > 0.25$, see Section 4.3.3). The computed distance to the quay wall when the ship is alongside is $X_w \approx 7D_p$. With C_h = 9.5 m, the distance to the maximum velocity at bed is $\approx$ 50 m, greater than the

TABLE 4.5: Example calculation at MS2A. Results are shown according to Minimum, Mean and Maximum computed velocity values.

	$U_0(ms^{-1})$	$U_b(ms^{-1})$	β_{is}	Ψ
Min	6.5	0.9	6.4	0.03
Mean	7.5	1	4.8	0.04
Max	9	2	3.3	0.06

distance to the quay wall. At the same time, using the mean value of the efflux velocity at MS3A ($U_0 \approx 6$ ms^{-1}, see Figure 4.14), the computed Wall-Froude number is $Fr_w = 0.3$, over the threshold obtained in the Chapter 3 of this dissertation. According to both criteria, scour at the toe of the quay wall is expected and the equations for confined flow must be used. Therefore, in case of MS3A and MS1D (arrival and departure maneuver, respectively), U_b is computed considering flow confinement, yielding higher results in case of Dutch method rather than German method. This is shown in Figure 4.14 (c) and (d), where the confined scenarios are highlighted by adding a red contour to the bar plot. Close to the West-Quay, the mean value of U_b calculated during the arrival maneuver (MS3A) is between 2 and 3 ms^{-1}, while it is lower than 2 ms^{-1} at the departure maneuver (MS1D).

Far from the West-Quay, Dutch and German formulation show higher disagreement in the results, at it is expected when using both methods due to the differences in the recommended coefficients (see Section 4.3.3). However, if the same method (either Dutch method or German method) is considered to compare the results obtained at the different maneuvers (arrival and departure), no significant differences are found. For instance, by comparing the Maneuver Section 2 in case of arrival (MS2A) and departure (MS2D) maneuver, which correspond to unconfined flow and ship locations inside the inner basin (see Figure 4.6), a mean value of 3 ms^{-1} is computed during the arrival maneuver, while a value of 2.5 ms^{-1} is obtained at the departure one. This is in disagreement with the erosion pattern, which points to a major effect of the arrival maneuver rather than the departure one. The main difference between the compared Maneuver Sections (MS2A and MS2D) is the regime at which the engines are used. While during MS2A the main engines are used one ahead and the other astern to allow the crabbing motion, during MS2D both engines run ahead at low to mid engine power.

4.5 Discussion

The jet flow generated by maneuvering ships in low bed clearance situations is known to induce erosion over the seabed sediment but is still difficult to predict the effects of a specific ship operating in a harbor basin. Surprisingly, the study of the erosion generated by ship's propeller has barely been related with the maneuver itself, which is the main causative of the propeller's behavior. In BAW (2010), for

instance, it is stated that the mooring (final stages of the arrival maneuver), the cast off (the beginning of the departure maneuver) and the acceleration phase (when the ship is sailing out of the basin) are considered the situations in which the vessel, maneuvering at low speed, uses maximum propeller power and therefore is potentially more harmful for the seabed. This is not in agreement with the observed erosion pattern at the study case. As shown in Section 4.4 (Figures 4.8 and 4.9) the arrival maneuver is expected to induce higher loads over the bottom rather than the departure one. In the acceleration phase, which in the present case corresponds the departure Maneuver Sections MS2D and MS3D, no scour is observed near the propellers position. Rather, an accretion area is observed nearby the location of the propellers during the starboard turn in the departure maneuver, corresponding to Maneuver Section MS2D (see Figure 4.9).

Three points of interest in the bathymetry of 2017 (Figures 4.8 (b) and 4.9 (b)) have been selected to understand the relationship between the ship maneuver, the propellers behavior and the erosion pattern. These points are: the sedimentation area near the West-Quay (see Figure 4.2 (b)), the area of bed protection (see Figure 4.2 (a)), and the scour around the bed protection (see Figure 4.2 (a) and (d)). A decrease of the minimum depth in the sedimentation area, with an increase in the maximum depth of scour between 2015 and 2017, is observed in the elevation profiles evolution. This is also reflected in the evolution of sediment volume above and below the reference level -12 m, as stated in Section 4.2.2. Since the eroded volume (below -12 m) increased between 2015 and 2017, together with a lower increase in the deposited volume (above -12 m), local transport from the erosion areas to the accretion areas, combined with sediment transport outwards the basin must be expected.

Interestingly, the effects of the bow-thrusters over the sedimentation areas are observable by a gap in the elevation profile in Figure 4.2 (b), at 200 m from the South Quay, the approximate location of the bow-thrusters when the ship is alongside. As stated in Section 4.4, these effects are considered to be due to the action of the bow-thrusters at the beginning of the departure maneuver, i.e, during MS1D. The effects in this case are comparable to the effects found by Roubos, Blockland, and Van Der Plas (2014), in their field study on the bow-thrusters induced scour at quay walls. In this case, the erosion depth is stable between 2015 and 2017, pointing to an equilibrium around -12 m.

In Figure 4.8, clear agreement between the erosion pattern and the propellers position during the arrival maneuver is found. Specifically, according to the Maneuver Sections defined in the simulator maneuver (see Figures 4.12 (a) and Figures 4.13 (a)), the erosion pattern is in agreement with Maneuver Sections MS2A and MS3A.

As stated in Section 4.4, the use of ahead port propeller and astern starboard propeller, simultaneously, is needed to approach the ship's stern to the final berthing location. The effects of twin propeller at inverse regime are not considered in the guidelines or literature, although it is a common maneuvering scenario in twin propeller ferries. The astern rotating propeller induce a jet towards the ship hull, that is deflected. The effect of the jet deflection by the ship hull may be of importance, increasing the flow pressure over the bottom just below the propellers plane. This is indeed, observed in the physical model experiments performed by Mujal-Colilles et al. (2018) and in the previous Chapter in this dissertation (3).

After computing the mean velocity at the bottom, at each Maneuver Section, similar values are obtained between departure and arrival maneuver, with due consideration of the calculation method. For instance, considering the German method, the mean velocity at bed during MS2A is around 3 ms^{-1}, and the mean velocity at bed during MS2D is around 2.5 ms^{-1}. However, the effects of each Maneuver Section according to the erosion pattern show that MS2A induce high erosion at the bed, while MS2D seems to have barely any effect over the sediment. As shown in Figures 4.12 (b) and 4.13 (b), there is a significant difference in the percentage of engine power used at these two Maneuver Sections. However, since the U_0 is proportional to the cubic root of the engine power, a lesser difference is obtained in the U_0 and U_b, being the last linear with the first. Again, the more remarkable aspect is that the propeller working in the astern regime cannot be considered by applying the existing equations in the guidelines. The equations, however, are used mainly to obtain estimations of the expected load, to be used as known input to design formulas. According to BAW (2005), protection rocks of $d_{50} \approx 1$ m should be used to ensure stable bottom in case of U_b values between 2 and 4 ms^{-1}. This is in agreement with the current protection of the eroded area, after the adaptation work performed in 2015, as explained in Section 4.2.2. Moreover, the example calculation following the work in Blokland and Smedes (1996) showed that the re-filling material used in the adaptation work should be mostly stable under the operation conditions in the simulator. Indeed, this bottom protection has been proven to be stable between 2015 and 2017. However, the use of this kind of bed protection, although useful to be applied locally, may lead to major cost increases in the harbor maintenance if no other actions are considered in similar basins.

According to PIANC (2015) a factor of 0.15 is recommended to be applied to the total installed power of the main engines, which is considered the regime at which the engine is operating inside the port. As per the obtained results, this factor is found to be a good estimation of the power usage during both the arrival and departure maneuvers. Likely, in case of cross-wind conditions or counter-currents, the ship needs more power to perform the same maneuver, leading to slight underestimations. In case of applying higher coefficients to the equations to obtain the efflux

velocity (e.g., R.O.M. (2012) recommends 0.4) some overestimation may occur, at least in calm and mild wind conditions.

Special attention is paid to the obtained results near the quay wall, during the last part of the arrival maneuver (MS3A) and the beginning of the departure maneuver (MS1D). At these Maneuver Sections, the propellers plane are parallel to back quay (Southwest corner of the harbor basin), at a minimum distance of ≈ 40 m (i.e., around 7 D_p). Therefore, the jet flow is considered to be *confined*. This distance is, however, close to the upper boundary established in PIANC (2015) to obtain the distance to the maximum flow velocity in case of unconfined flow ($C_h/X_{mu} < 0.18$), suggesting that the effects of the quay wall, although present, may not be of significant importance. This would explain why the deeper erosion depth in the study area, previous to 2015 (before the adaptation works), is not located just at the quay toe (see Figure 4.2 (a) and (c)). In these Maneuver Sections, only one propeller is used ahead close to the quay wall, as shown in Figures 4.12, MSA3, and 4.13, MSD1, while the other is used astern. Again, the equations in the guidelines cannot provide complete understanding of the phenomenon, since the action due to the propeller in astern regime cannot be considered. Finally, since the twin propeller system is combined with a twin rudder system, the effects of a rudder over the jet flow must be considered. The presence of a rudder is known to split the jet flow with upwards and downwards deflection, increasing the spreading angle and inducing significantly higher jet velocities at the bed (PIANC, 2015). With due consideration of the former, the effects that Maneuver Sections MS3A and MS1D have over the bed, cannot be considered only by applying the proposed formulation.

4.6 Concluding remarks

- The present work used the methodology published in Llull et al. (2020) to analyze a case study and trigger the erosion observed in a harbor basin to the maneuver pattern. Moreover, by using the maneuver simulator, evidence of the main characteristics of the engines and thrusters performance during the arrival and departure maneuver is provided.

- The results obtained from the simulator are used as input to the main equations in literature to compute the flow velocity and the bottom stability.

- The AIS information is clue to clearly visualize and define the maneuvers sections and patterns. The AIS equipment now hosted by the FNB is an excellent tool to monitor maneuvers of interest, compute maneuver time, extract statistics of harbor use, traffic, etc. In this particular case, the detail provided by the AIS system is enough to obtain a clear track of any maneuver that is willing to be studied.

- The arrival maneuver is proven to be more harmful than the departure one in the harbor basin area under unconfined jet flow action. The coincidence in the scour pattern, obtained from the bathymetries of the harbor basin, and the propellers location yielded consistent results in this direction. After the use of the maneuver simulator, the results confirmed that higher engine power is needed to perform the arrival maneuver. Moreover, the regime of the main propellers during the whole maneuver is a combination of ahead and astern regime.

- The effects of the propeller jets in astern regime are not considered by the guidelines, but is expected to be important as per the presented results. Since the main scour pattern is in coincidence with the ship positions where both ahead and astern orders are needed, the estimation of the loads induced by astern rotating propellers is needed.

- The bow-thrusters during the first part of the departure maneuver are expected to induce scour of the area nearby to the West-Quay up to -12 m. The scour hole is surrounded by an accretion area that reaches dangerous low depths of -7 m.

Chapter 5

Conclusions and future work

The study of the propeller jet induced scour is a wide field that embraces several research lines, e.g., single propellers, twin propellers, confined or unconfined jets, scour at closed and open quay structures, etc. Because of this, plenty of boundary conditions need to be considered when evaluating the potential damage that a specific ship may cause. The influence of rudders, nozzels, or ship hull are examples of these boundary conditions. It is, therefore, challenging to account for all these parameters in experimental studies. Because of that, different standard situations have been studied at laboratory during the past and recent years. Through the study of different standard situations, an attempt is made to cover the whole range of individual situations found at field.

In the present work, two different standard situations have been analyzed from different approaches. In Chapter 2, new experimental work in one of the most common situations, i.e., single propeller in an unconfined scenario, is presented. This work aimed at providing new insights on the characterization of the induced bed shear stresses by propeller jets, a topic barely studied to date. In Chapter 3, an experimental study in scour due to twin propellers in confined scenarios is presented. Although very common at field, few research has been published regarding the twin-propeller scour, and even less in case of confined scenarios. Both the situations studied in Chapter 2 and Chapter 3 are related to the work presented in Chapter 4, the real case study. In the latter Chapter, the different parts of the maneuver are identified depending on the use of the propellers or engines. At each part of the maneuver, either one or both propellers are used, being therefore in a situation of single or twin propellers. The confinement or unconfinement scenario depends on the ship position relative to the quay wall. The work presented in Chapter 3 is used in the case study to establish a threshold distance between the propeller and the quay wall. This threshold allows to differentiate between the confined and unconfined scenarios. In this maneuver, the confined scenarios are restricted to the end of the arrival maneuver and the start of the departure maneuver. Therefore, according to the different scenarios faced in the real cases, the analysis must be performed according to the most similar standard situation.

In summary, this dissertation presents the research performed during the last three years at three different research groups working on the same topic. A new model to estimate bed-shear stress under single propellers in low bed clearance situations is provided. Moving the research to further steps, this work also proposes a new expression to estimate the maximum eroded depth and the threshold of scour in case of confined twin propeller jets. Finally, the use of a real maneuver simulator for the first time, demonstrates that this is a needed tool to estimate the position and magnitude of the maximum loads at the seabed due to ship maneuvers. Now, conclusions and recommendations for future work are provided, summarizing and correlating the final remarks presented at each individual Chapter.

5.1 Conclusions on Chapter 2

The obtained results from the work presented in this Chapter are focused on the estimation of the bed shear stress due to the propeller action as a function of the two main variables: the efflux velocity and the bed clearance. To achieve this objective, a self-designed shear plate has been used to obtain direct measurements of bottom shear stress over a horizontal rough bed. This instrument has been used for the first time in case of propeller jets. The obained results have been related to the characteristic velocity of the propeller jet, also measured at the laboratory in the same conditions.

The velocity measurements were performed with a very adaptable device that has been proven to yield good results in the regions close to the propeller face. This is especially true in case of measurements at the inner jet region, where the maximum velocities are located. The turbulence intensity and the spectral analysis results were useful to better characterize the flow field at the different regions in the jet, showing consistency with literature studies. The propeller's thrust coefficient is also derived from this measurements, thus avoiding uncertainty derived from the estimation of this parameter.

The obtained expression, Eq. 5.1, with $C_f = 0.0013(\frac{C_h}{D_p})^{-1}$, is expected to work in the range of bed clearance distances in this work. According to this expression, for a unique efflux velocity, the mean bed shear stress is inversely related to the bed clearance through a proportionality coefficient. The surface roughness must be considered if the expression is applied. In the present case, only coarse sand is used, therefore the use of the proposed expression should be limited to the case of propeller jet flow over a similar material.

$$\tau = \frac{1}{2}\rho C_f U_0^2 \tag{5.1}$$

The shear plate is proven to be well working under the present flow conditions and the obtained results are satisfactory to fit the scope of the present work. In this respect, the time-averaged shear stresses showed good repeatability at the different experimental conditions (i.e., the different propeller speed of rotation and bed clearance). The dimensions of the shear plate may be a source of uncertainty, however, a compromise between the uncertainty due to the integration of forces over the 0.1 m^2 surface and the response of the strain gauges is needed when this instrument is used. With the chosen dimensions of the shear plate, measurements in the optimum range of the sensors are ensured.

The shear plate is located at the region where maximum flow velocities are expected. Based on literature studies, the maximum flow velocity at the bottom level in case of jets over a horizontal boundary is estimated. Two different axial distances from the propeller plane to the shear plate edge were tested. These distances were chosen to locate the plate at 2 positions, with $\approx$ 50% overlapping. The experiments that yielded higher shear stresses are used to obtain empirical relations between the propeller jet velocity, the bed clearance, and the time-averaged shear stresses.

5.2 Conclusions on Chapter 3

The obtained results in Chapter 3 provided new insights in the scouring action of a twin propeller system in a confined condition. This is a common situation, described in the bed-side books and guidelines, but still focus of very few research in propeller induced scour.

Experiments at physical model allow to study the multiple parameters involved in the scour process separately, by including new variables or keeping them constant. The propeller bed-clearance, the wall-clearance and the speed of rotation are the main parameters analyzed in this work. Although useful to obtain clear results at laboratory, these experiments provide no full understanding of the problem, and attention must be paid to the validity range of the formulas obtained from the physical model. In this thesis, three equations are proposed to estimate the maximum scour depth in case of twin propeller jets. Two of them, Eqs. 5.2 and 5.3, are used to describe the temporal evolution of the scour depth near the Front Wall. The third, Eq. 5.4, is used to predict the equilibrium scour depth due to backward rotating twin-propellers.

$$\frac{S}{X_w} = 2.539 \times 10^{-4} \left(\frac{C_h}{X_w}\right)^{0.5} \left(\frac{U_0}{\sqrt{g X_w}}\right)^2 \left[ln\left(\frac{t U_0}{X_w}\right)\right]^{4.425} \tag{5.2}$$

$$\frac{S}{X_w} = 2.531 \times 10^{-3} \left(\frac{U_0}{\sqrt{g X_w}}\right)^{2.67} \left[ln\left(\frac{t U_0}{X_w}\right)\right]^{3.19} \tag{5.3}$$

$$\frac{S_{m,e}}{D_p} = 1.19\left(\frac{nD_p}{\sqrt{gD_p}}\right)\left(\frac{C_h}{D_p}\right)^{-0.5} \tag{5.4}$$

Eqs. 5.2 and 5.3 show that near the Front Wall, the scouring is governed by the Wall Froude Number (Fr_w), both in case of FWD and B & F experiments. The bed clearance, on the other hand, has much lower effect in the scour depth near the Front Wall. This is especially true in case of B & F rotation, where no differences are observed in the evolution of the maximum scour depth near the Front Wall due to the change in this variable.

A threshold value of Fr_w is found to define the no-scour condition near the Front Wall. The measured scour depths are extrapolated to the no-scour condition, showing that no significant scour is expected for $Fr_w < 0.25$. This threshold may be applicable to real scenarios, to define the minimum distance between the ship propellers and the quay walls.

Far from the wall, due to backward rotation, Eq. 5.4 show that the equilibrium scour depth is much more influenced by the flow velocity rather than the bed clearance. In these experiments, the highest speed of rotation and the lowest distance to the bed yielded the greatest scour depth. The equilibrium depth in case of backward-rotating twin-propellers is linearly dependent on the Froude number of the flow and inversely related to the square root of the dimensionless bed clearance.

The derived equations are expected to work in the ranges of non-dimensional parameters they have been developed with. In this work, the ranges of non-dimensional parameters used (Fr_d, Fr_w, X_w, C_h) are closer to the ones expected in-situ, compared to previous works. Still, scale effects should not be totally discarded if the expressions are not validated in other conditions, both at model and prototype scale.

The time duration of the present experiments is short in comparison with previous work in literature, but the maximum scour depth is not lower, mostly when compared to experiments in unconfined flow conditions. The twin propeller system causes higher loads over the sediment bed, compared to single propellers, therefore leading to higher scouring rates. At the same time, the higher densimetric Froude number in the present experiments, compared to the previous work, is related to higher scouring rates, mostly during the first stages of the scour hole development. Still, the equilibrium condition is not reached at the near-wall region in the present experiments, although some of them reached a stabilization stage. Contrarily, in the case of backward rotating propeller, the equilibrium is reached in this work at a scour depth close to 1 D_p, for the lowest bed clearance. The effect of the ship hull, in this work modeled as a squared-shape stern, is undoubtedly of relevance in this process.

For the first time, backward rotating propellers have been studied, aiming to provide a guide to new works considering this scenario. Ship propellers are designed to work in ahead regime, where they are much more efficient. This fact, however, should not exclude the propellers in astern regime from the scour analysis. During in-harbor maneuvers, propellers may be used either in ahead or astern regime, depending on the maneuver requirements. Because of that, the Back & Forth scenario is proposed in this work as standard situation to analyze the effects of the intermittent astern and ahead regimes.

5.3 Conclusions on Chapter 4

The study of the propeller induced scour is approached in this Chapter from a case study. This work aimed at identifying the conditions where a real ship is more damaging, during a standard maneuver situation.

Within a single ship maneuver, the duration of the hydraulic load is short, and the location changes due to the ship motion. However, from AIS data visualization of the study ship during arrival and departure maneuvers, it is clear that the same maneuvers are performed with daily basis. Through the time evolution of the bed morphology, the cumulative effect of these loads is proven to cause a well-defined erosion pattern at the seabed.

The location of the main propellers during the arrival and departure maneuvers shows that only the arrival maneuver patterns are coincident with the eroded area. Thus, the arrival maneuver must be expected to induce higher loads over the bottom compared to the departure one, at least in the region with unconfined jet conditions. This could have direct practical applicability in harbor management. For instance, the use of the tug boats in the case study, if needed, may be only necessary during arrival maneuvers, since it appears to be the most harmful maneuver.

By reproducing the maneuvers in the simulator, results of the engine performance during both maneuvers (arrival and departure) are obtained. At the arrival maneuver, when the propellers are located above the eroded area, the engines show a consistent behavior: one propeller runs ahead, while the other is needed to work astern in order to approach the ship's stern to the berth, i.e., *crabbing*. During the departure, only the first stages of the maneuver present this behavior. Moreover, the percentage of total engine power needed in the arrival maneuver is higher than in the departure one. During the unberthing (departure maneuver), however, the bow-thrusters induced thrust is higher than at the arrival maneuver. Moreover, the bow-thrusters jet is directed towards the side-wall during the departure maneuver. These effects are observed in the seabed evolution, since the eroded areas are located below the propellers position during the arrival maneuver, and near the bow-thrusters

location during the departure. The last, however, is of lower magnitude.

Formulae in literature is applied to the study case, from the results of the simulator. The mean efflux velocity and seabed velocity is obtained at every predefined Maneuver Section. The higher values are found during the Maneuver Section MS2A, in agreement with the eroded pattern in the harbor basin. However, the differences between the calculated mean velocity at bed during the arrival (e.g., Maneuver Section MS2A) and the departure (e.g., Maneuver Section MS2D) are not remarkable. The main difference between the Maneuver Sections MS2A and MS2D is the use of the engines astern. At the departure, the starboard turn of the ship is mostly driven by the use of the bow-thrusters. At the arrival, both of the main engines, one astern and the other ahead, are needed to approach the ship stern to the berth. As seen in Chapter 3, the propeller jet in astern regime, interacting with the ship hull, may create scour holes beneath the propellers position with an equilibrium depth up to $1D_p$.

The methodology used in this Chapter aims at providing specific insight into a case study, and the results cannot be applied at other situations without proper analysis. However, it is now proven that the higher loads location can be estimated from AIS data analysis, after reproducing the maneuver in the simulator. The expected loads over the seabed can be quantified for specific maneuvers by using the available methods in literature and guidelines. In the present case, for instance, the formulae from PIANC (2015) was used to estimate the efflux and bottom velocity at every Maneuver Section. After that, the bed protection is dimesioned to ensure a stable bottom below the ship propellers location during the maneuver.

5.4 Future work

Based on the experience and the results obtained from the work presented herein, this Section proposes future work and recommends some topics that may be interesting for further research.

The results obtained in Chapter 2 are encouraging to continue the experimental work in propeller induced shear stress measurements with the proposed set-up and instrumentation. New experiments with the same conditions and different plate roughness are expected to add new insights into the effects that this parameter have on the friction coefficient. Performing experiments with a smooth plate could be also interesting to validate the measurements with literature studies, mainly focused on shear stress over hydraulically smooth beds. Moreover, new elements could be included in the experimental setup without impairing the proper functioning of the shear plate. Different propeller types, twin propellers and central rudders are examples of boundary conditions considered interesting for further studies.

In combination with the former, velocity measurements at the plate location are considered of main relevance to allow the estimation of the bottom shear stresses independently (see Section 2.1, where some methods are mentioned). In this regard, velocity measurements over the plate will provide further validation of the shear plate measurements. Moreover, characterizing the velocity at bed and use this parameter instead of the efflux velocity could be interesting to provide a more suitable parameter to relate the results with further experiments under different conditions, in case the efflux velocity is kept constant.

Future work in twin propeller induced scour is already on-going at LIM-UPC, following the work presented in Chapter 3. In the first place, from the already presented measurements, the analysis of the eroded volumes is under development. From the 3D surface grids obtained from the work presented herein, the total eroded volume at each time-step is computed for every experiment. Although the maximum scour depth is an important parameter to account for in design, Port Authorities are also concerned on the volume of material that is removed. As seen in Chapter 4, the amount of volume that is removed from the eroded area, end up in a deposition region, where some problems may arise due to the reduced water depth. Reliable estimations of the time evolution of the eroded volume could be used to optimize dredging operations in harbor basins and navigable channels.

As discussed in Section 4.5, the *crabbing* motion has been not considered in experimental models to date, but it is suspected to induce high erosion depths. The results obtained through the maneuver analysis and simulation in Chapter 4 point to the need of considering this maneuver situation, very common in case of twin-propeller ships equipped with bow-thrusters. Experiments at physical model in Chapter 3 presented some results in backward rotating propellers, but further work must be also focused on inverted forward/backward twin-propellers, i.e., the combination during the *crabbing* maneuver. Inclusion of a more accurate design of a ship hull and central rudders are also necessary to perform further experimental work in the physical model. Finally, flow velocity measurements in case of backwards rotation are relevant to this work and must be performed in the future. The results obtained in scour depth due to backward rotation shows that the velocity term is more relevant to the scour depth than the bed clearance, but so far experimental work relating the propeller characteristics, the ship hull and the bed induced velocities in backward rotation is lacking.

It must be considered that the work presented in Chapter 4 is based on the reproduction of a standard maneuver, validated through expert criteria. In order to obtain more robust results, the maneuvers need to be reproduced at the simulator several times, by different experts. Statistics of the use of the engines will provide stronger

evidence on the locations where higher loads must be expected. The main limitation, however, is that maneuver simulations are time-consuming and knowledge in maneuvering is needed to perform the work. These limitations must be taken into account when designing future simulator studies.

Finally, new work in the simulator could be also focused on the effects of crosswinds on maneuvers and the increase of the erosive potential of any maneuver in severe weather conditions. Through maneuvering studies with different meteorological conditions, the more damaging scenarios could be identified and threshold conditions could be established, for example, for the use of tugboats.

Appendix A

Velocity measurements

A.1 Long measurements at x = 1D$_p$

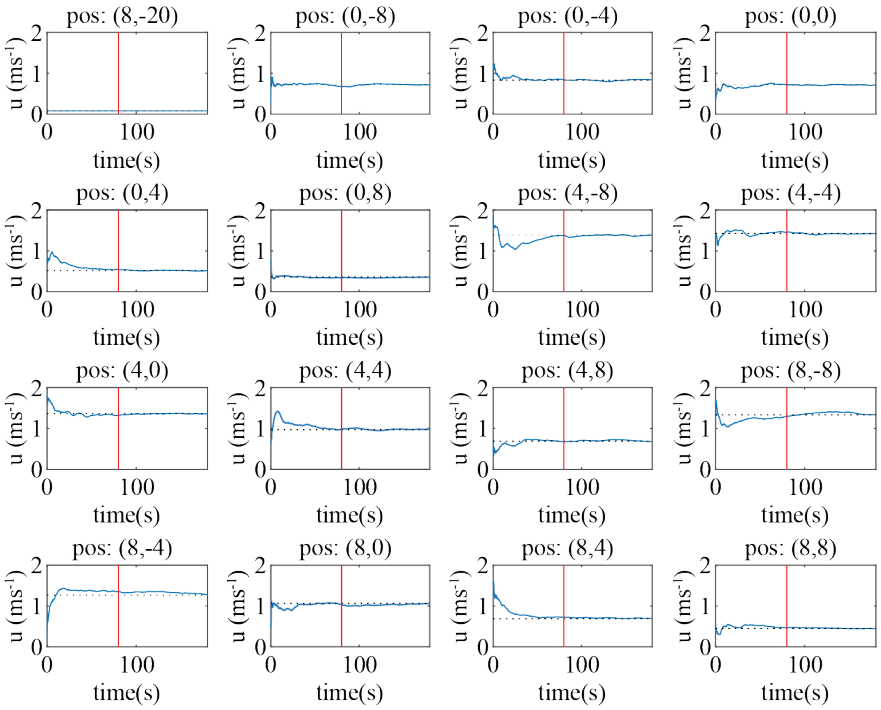

FIGURE A.1: Cumulative mean of the time-series. The solid red line shows t = 80s and the dashed black line shows the value of the time-averaged velocity.

A.2 Axial velocity distribution

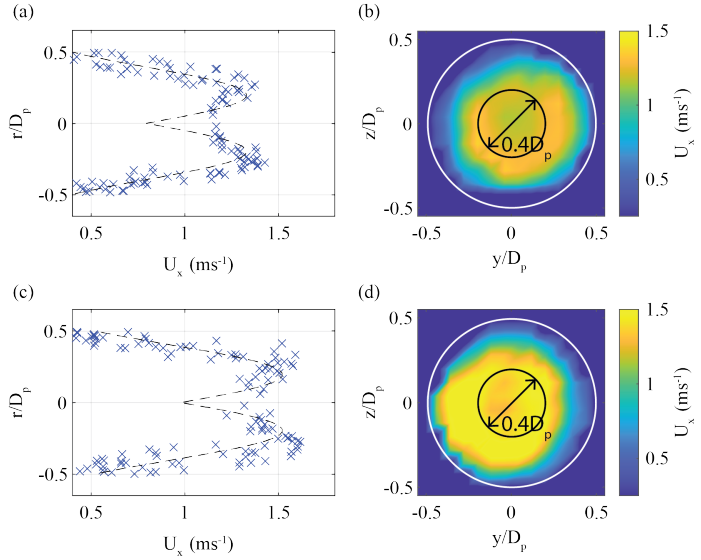

FIGURE A.2: Velocity distribution at the efflux plane (Prop2). (a), (c): Radial distribution of $\overline{u}$ fitted with the double-peak gaussian model at 250rpm and 300rpm respectively.(b), (d): 2D colormaps of $\overline{u}$ at 250rpm and 300rpm respectively. The solid black circumference shows the radial location of the maximum velocities, while the white solid circumference shows the propeller diameter.

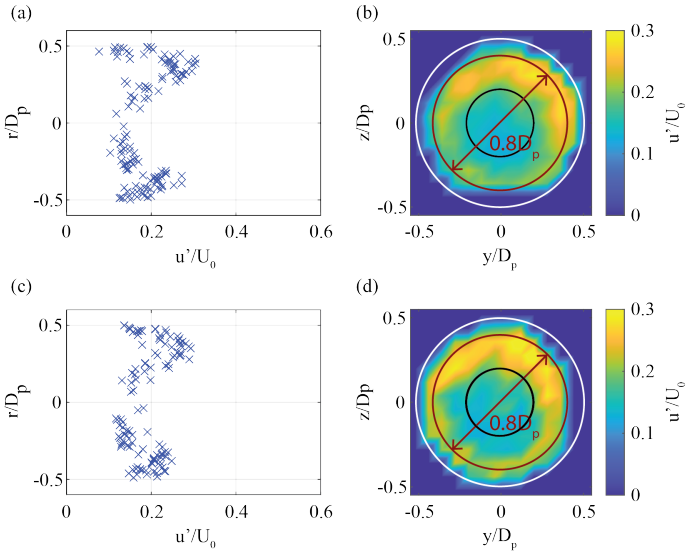

FIGURE A.3: Horizontal TI distribution at the efflux plane (*Prop2*). (a), (c): Radial distribution of $\sqrt{\overline{u'^2}}/U_0$ at 250 rpm and 300 rpm respectively. (b), (d): 2D colormaps of $\sqrt{\overline{u'^2}}/U_0$ at 250rpm and 300rpm respectively. The red circumference shows the radial location of the maximum TI, while the white and black circumferences show the propeller diameter and the location of maximum mean velocities.

A.3 PSD of axial velocity measurements at the inner jet

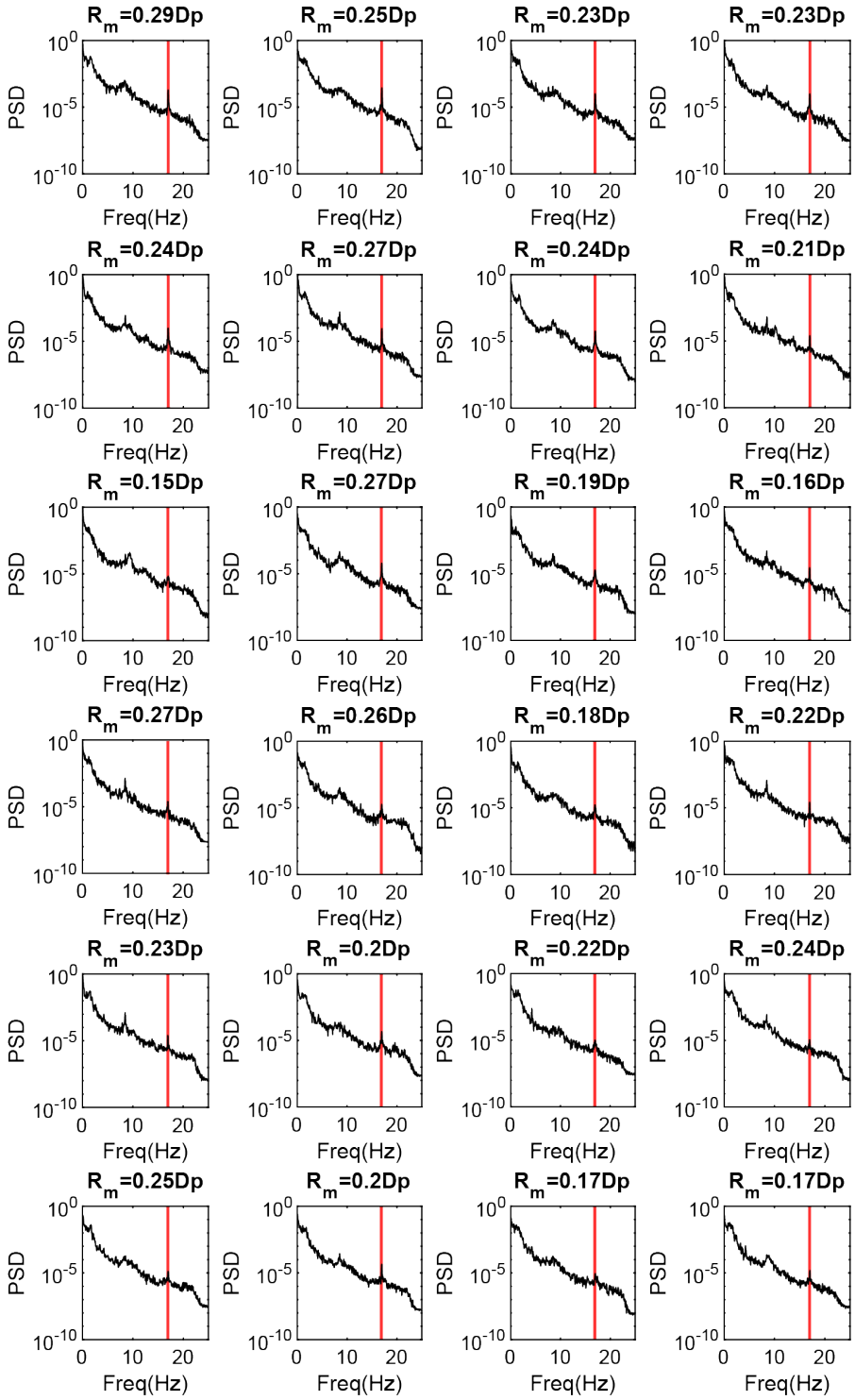

FIGURE A.4: PSD measurements at the inner jet (250 rpm). Each figure contains the radial position (R_m) of the measurement.

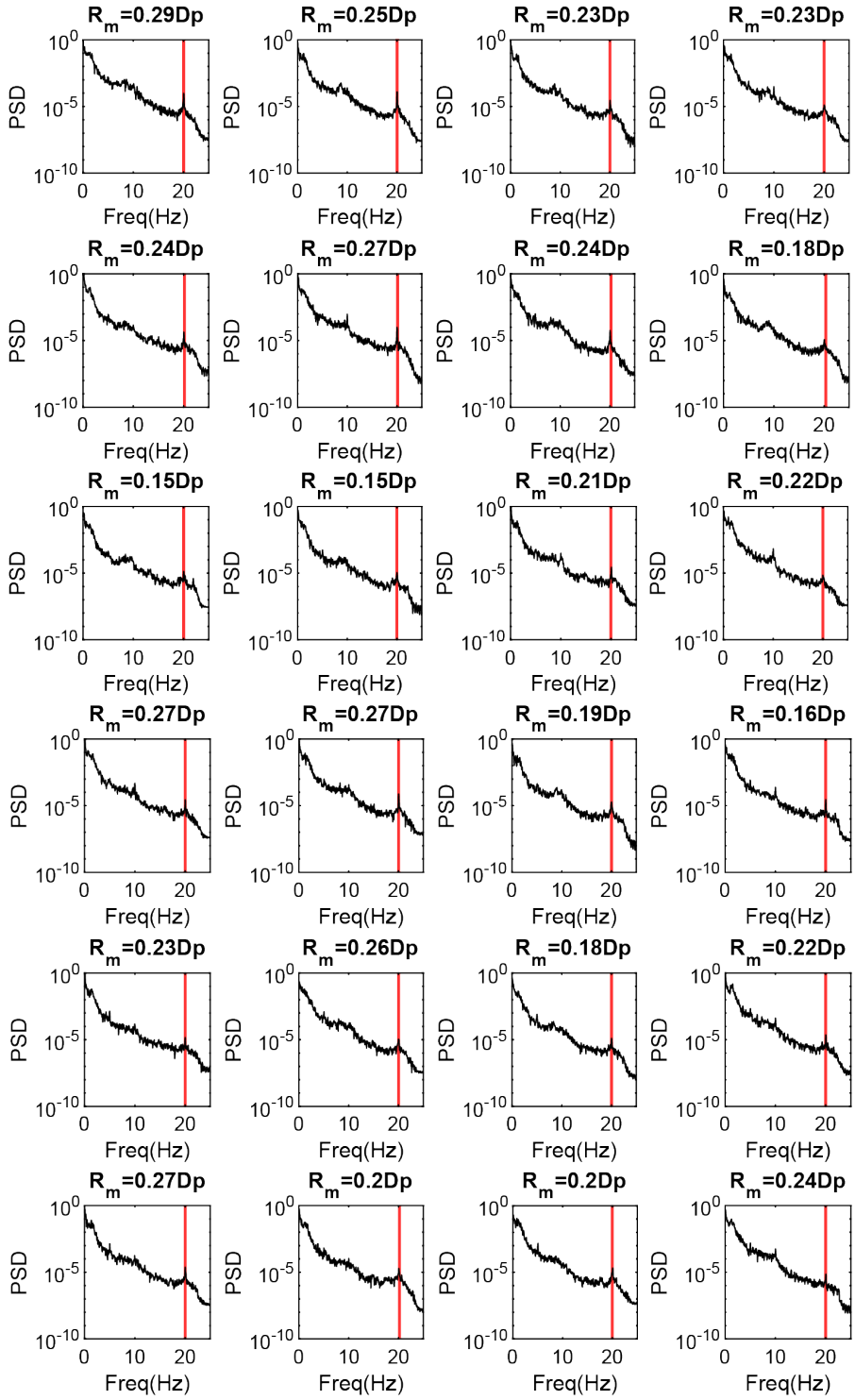

FIGURE A.5: PSD measurements at the inner jet (300 rpm). Each figure contains the radial position (R_m) of the measurement.

Appendix B

Shear stress measurements

In this Appendix, the long measurement of bed shear stress obtained during BSS1 experiments is presented and compared with the 6 repetitions of short measurements in the same experimental conditions (300 rpm). The results are included since the filter applied to the shear stress measurements is based on the analysis of this long-series. The signal filtering was performed to minimize the noise level and to obtain the noise-free standard deviation of the measurements, to estimate amplitude of the fluctuations of the propeller induced bed shear stresses.

In Figure B.1 (a), (b), (c), the raw measurement obtained by each strain gauge (SS1 and SS2) is shown, together with the frequency spectrum and the cumulative frequency spectrum. The time-averaged bed shear stress and the standard deviation of the signal are included in table B.1 named as *signal0*.

A low pass Butterworth filter is applied with a cut-off frequency of 45Hz to remove the high frequency noise in the signals. The resulting signals are shown in Figure B.2 (a), (b), (c). The time-average and the standard deviation of the filtered signal are included in Table B.1 under the name *signal1*. An energy peak at a frequency of 10 Hz is observed and analyzed. The contribution of this range of frequencies to the signal is analyzed by applying a band-stop filter to the range between 8 and 12 Hz. The time-average and the standard deviations of the resulting signal are compared. The obtained values are included in the table and the filtered signal is named *signal2*.

After filtering, the time-average value is kept the same and the dispersion of the signal obtained by the two strain gauges yielded very similar values. Since the frequencies higher than 12 Hz do not significantly contribute to the resulting signal, a final design of a cut-off filter at 15Hz with order 7, enough to attenuate the frequencies at 10Hz without having any influence in the lower frequencies, is applied. The new signal is named *signal3*. The resulting signal is presented in Figure B.3 and the time-averaged measured stress and standard deviation are included in Table B.1.

The 6 repetitions of 80 seconds duration in case of BSS1 experiments are included to show the agreement with the time-average of the long-series. In Figure B.4 (a), (b),

all the measurements in BSS1 are shown. The power model $y = Kx^2$ with $K = 0.04$ (according to the results in Section 2.3.2) is plotted in solid black. At 300 rpm, the same speed of rotation as the long measurement, the average bed shear stress is 0.85 Nm^{-2}, in well agreement with the long measurement (see Table B.1). Besides, in Figure B.4 (c), (d), the time-average bed shear stress is plotted against the standard deviation of each measurement, yielding a linear agreement between both values with $R^2 = 0.88$. The characteristic slope of the adjustment is 1.1, also in well agreement with the standard deviation in the long-series (see Table B.1).

In Figures B.5, B.6 and B.7, the same results as in Figure B.4 are shown for each experiment (BSS2, BSS3 and BSS4, respectively). The power model in solid black is plotted with the different values of K showed in Section 2.3.2. In these cases, linear agreement between the time-averaged bed shear stress (τ_0) and the standard deviation of each measurement (σ_τ) is found, with different characteristic slopes (m), each one showing the expected variability of the bed shear stress for each experimental condition. The results are summarized in Table B.2, including the experiment acronym, the K value, the characteristic slope (m) and the R^2 of each linear fit.

TABLE B.1: Statistics of the original and filtered signal.

Signal	**Mean (SS1)**	**Mean (SS2)**	**Std (SS1)**	**Std (SS2)**
signal0	0.90	0.93	1.93	1.48
signal1	0.90	0.93	1.34	1.43
signal2	0.88	0.91	1.16	1.21
signal3	0.88	0.91	1.10	1.13

TABLE B.2: Results of the adjustments at each experiment.

Experiment	K	m	R^2
BSS1	0.04	1.1	0.88
BSS2	0.07	0.83	0.97
BSS3	0.05	0.83	0.95
BSS4	0.07	0.69	0.93

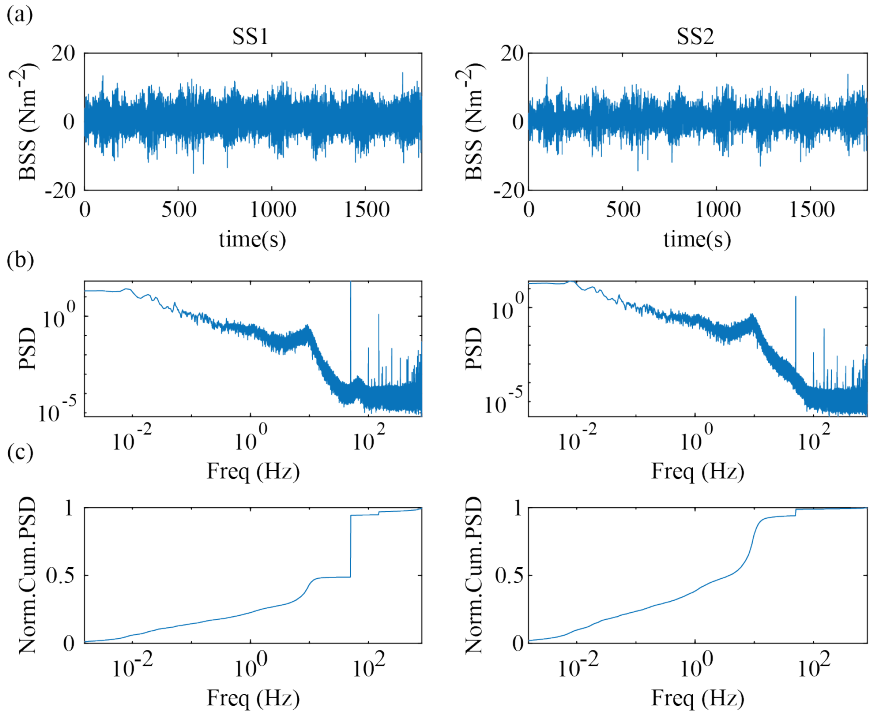

FIGURE B.1: (a) Time-series of *signal0*; (b) Power Spectral Density (PSD); (c) Cumulative PSD.

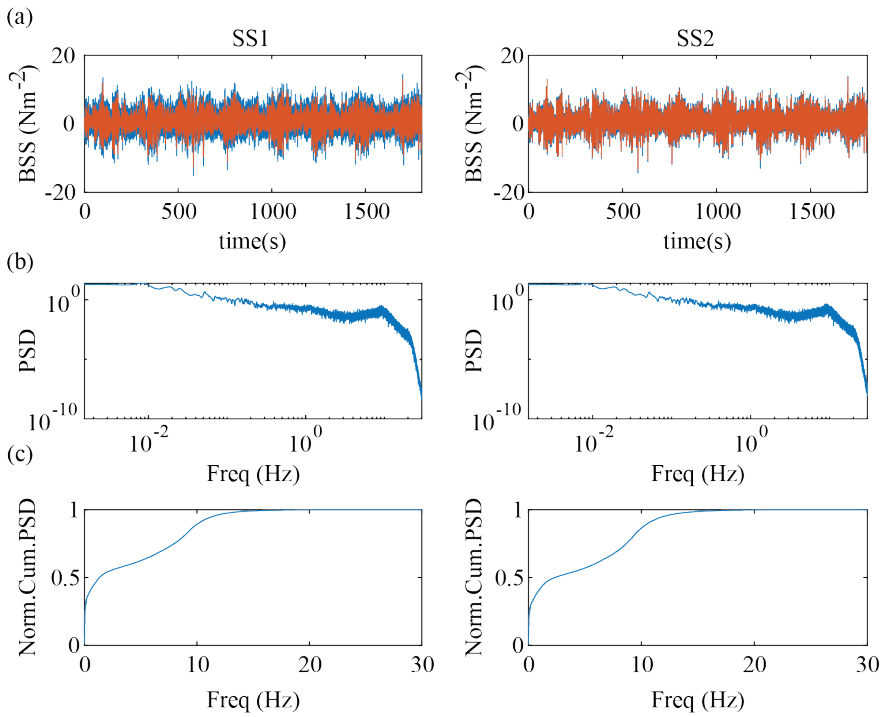

FIGURE B.2: (a) Time-series of *signal1*; (b) Power Spectral Density (PSD); (c) Cumulative PSD.

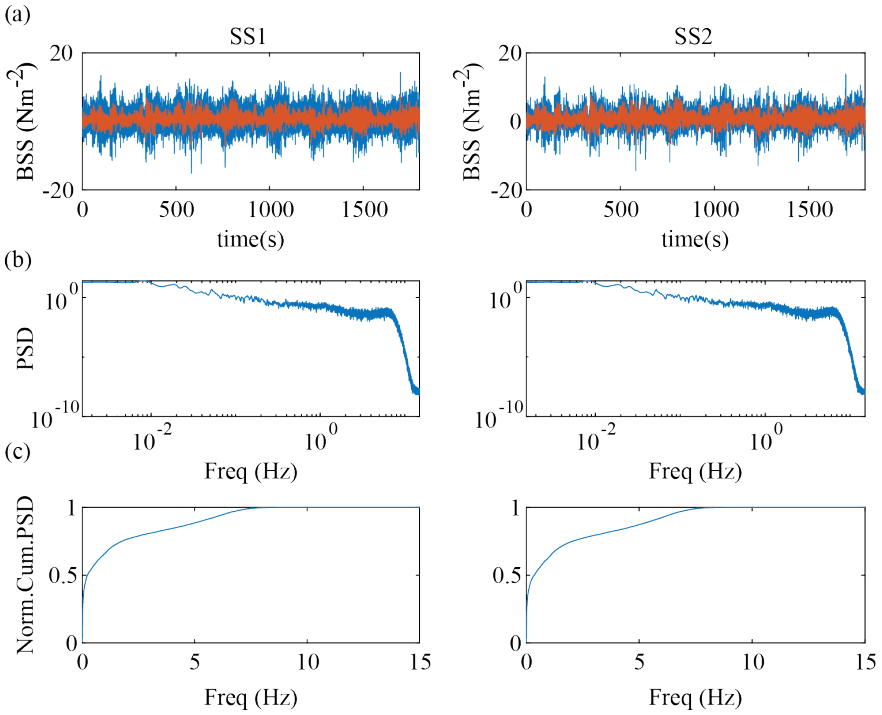

FIGURE B.3: (a) Time-series of *signal3*; (b) Power Spectral Density (PSD); (c) Cumulative PSD.

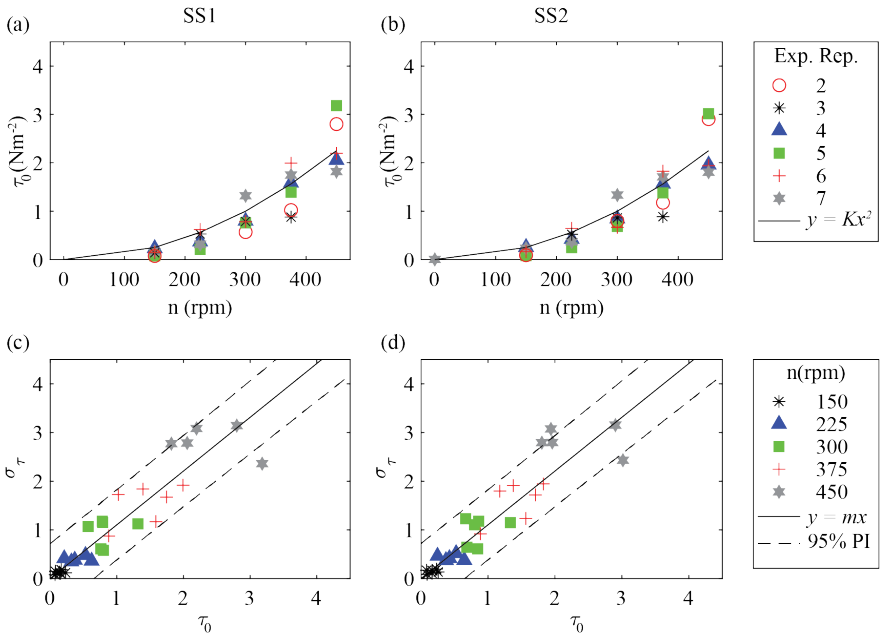

FIGURE B.4: (a), (b): Time-averaged shear stress at each repetition and speed of rotation in BSS1 experiment; (c), (d): Agreement between the standard deviation of each measurement and the time-averaged value.

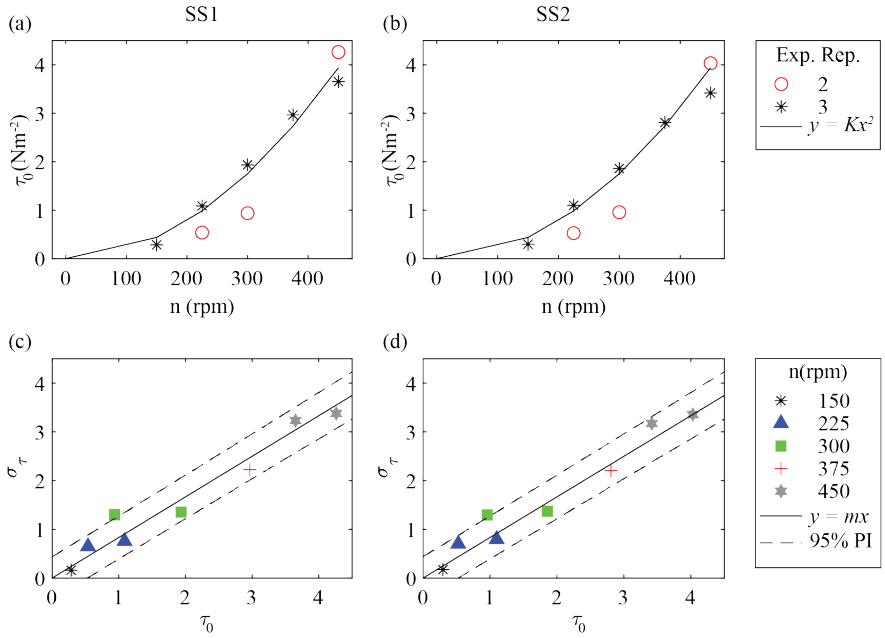

FIGURE B.5: (a), (b): Time-averaged shear stress at each repetition and speed of rotation in BSS2 experiment; (c), (d): Agreement between the standard deviation of each measurement and the time-averaged value.

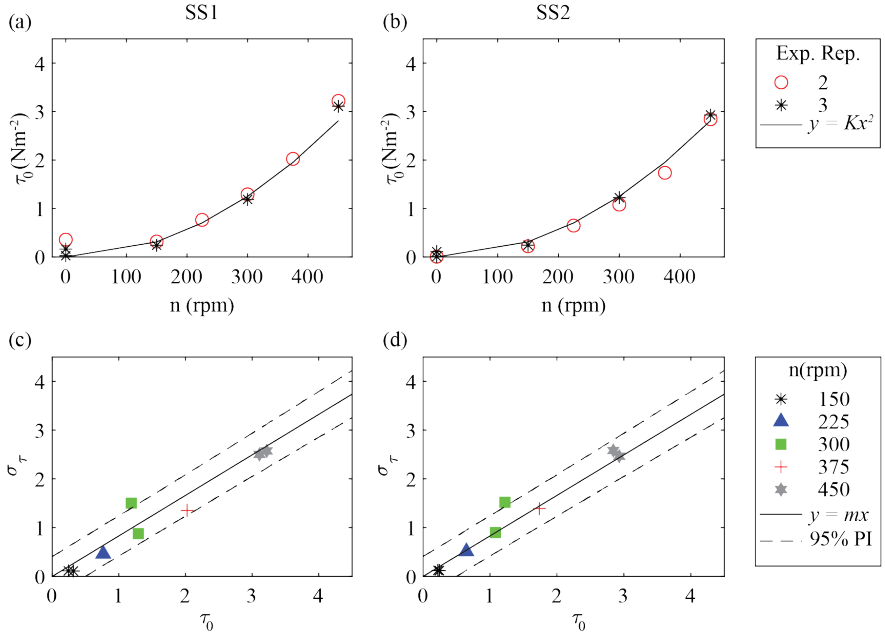

FIGURE B.6: (a), (b): Time-averaged shear stress at each repetition and speed of rotation in BSS3 experiment; (c), (d): Agreement between the standard deviation of each measurement and the time-averaged value.

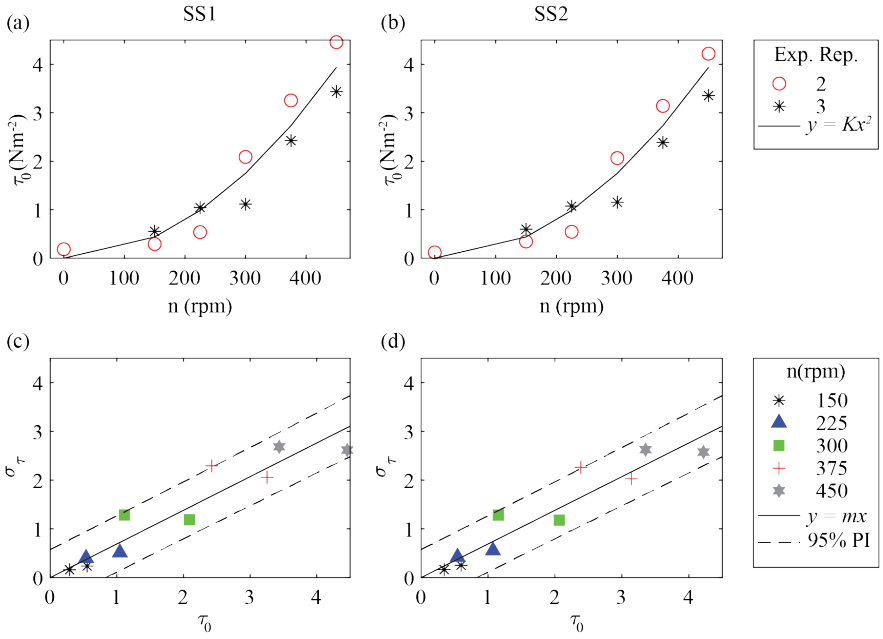

FIGURE B.7: (a), (b): Time-averaged shear stress at each repetition and speed of rotation in BSS4 experiment; (c), (d): Agreement between the standard deviation of each measurement and the time-averaged value.

Appendix C

Categorization of the maximum depth profile

This Appendix provides further details in the methodology used to categorize each profile as *merged*, *transition to merge* or *no-merged* profile, according to the presence of 1 or 2 scour holes due to Forward rotation. The scour hole due to Backward rotation is not considered to define each profile, since all the scour profiles obtained from B & F experiments present a main scour hole due to Backward rotation. The methodology is explained herein through some examples.

Departing from a center-line profile (or maximum depth profile), a finite differences based method is applied to obtain the bed slopes profile (first derivative of the center-line depth profile). Since the maximum depth profile is discretized at $\Delta X = 1$ cm, the Eq. C.1 is applied, being Z the scour depth at each X position along the maximum depth profile.

$$\Delta[Z](X) = \frac{Z(X + \Delta X) - Z(X)}{\Delta X} \tag{C.1}$$

In case of B & F experiments, this method will distinguish between *merged* and *no-merged* profiles by finding the HBH_{FWD} hole, in case it exists. The presence of HBH_{FWD} hole is determined by the existence of an Up-Crossing Zero (UCZ) in the slopes profile, between the near-wall region and the propellers plane. To avoid any misbehavior, the very first position of the main depth profile is set to 0 in all cases, so that a first UCZ is always found in the near-wall region. The next UCZ along the X axis is located at the position of the maximum depth of the HBH_{FWD} hole. In case there is no HBH_{FWD} hole, the slopes profile does not show any UCZ between the FW and the propeller's plane. An example is shown in Figure C.1, for the case of a *no-merged* profile (300 rpm) and a *merged* profile (400 rpm).

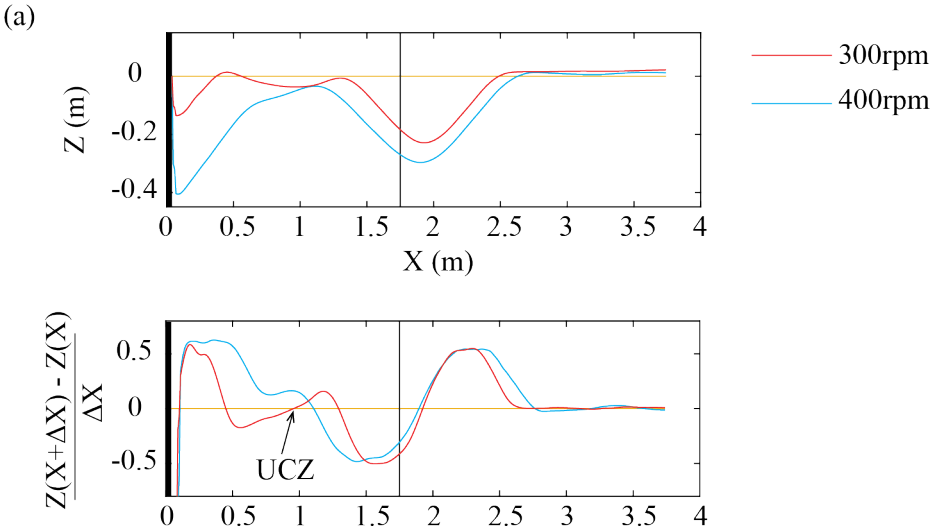

FIGURE C.1: $X_w^{min} = 7D_p$, $C_h^{min} = 1D_p$. (a) Maximum depth profile; (b) Slopes profile.

In FWD experiments, a third category -*transition to merge* profile- is added. The *transition* profiles are those profiles showing a two-hole morphology but clearly in transition to become *merged*. This condition is considered by evaluating the symmetry of the HBH respect to the vertical axis at the position of the maximum depth. Since the maximum depth is found by locating the UCZ in the sub-area between the FW and the propeller's plane, the positive and negative area enclosed by each curve are compared. In the cases in which the negative area is below a previously chosen accuracy value (in the present experiments, the 35 % of the total area is found reasonable) the profile is considered to be in transition. In Figure C.2 an experiment going through the three phases is shown to illustrate the method. At 5 minutes, the profile shows a *no-merged* morphology, at 25 minutes, it becomes a *transition* profile, and finally a *merged* profile is observed at 60 minutes.

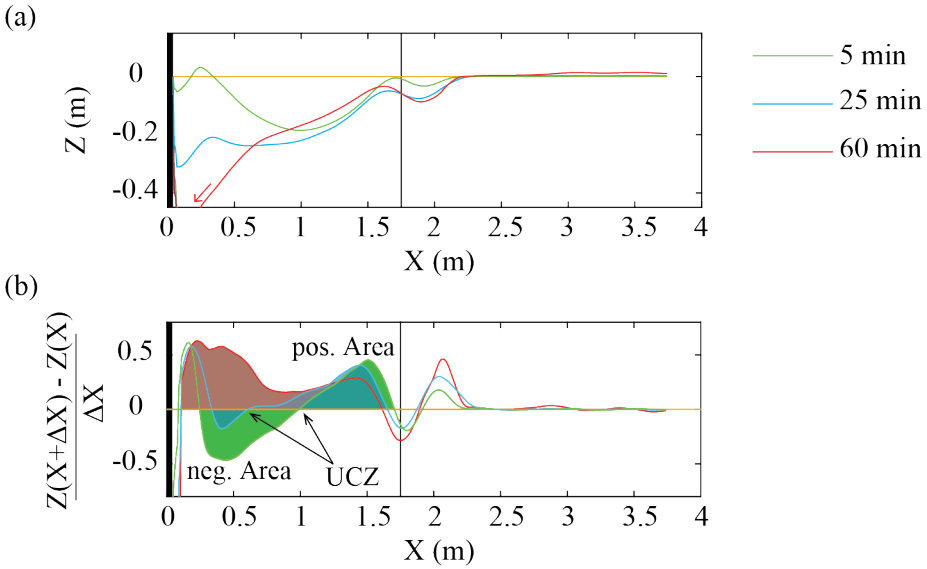

FIGURE C.2: $X_w^{min} = 7D_p$, $C_h^{min} = 1D_p$. (a) Maximum depth profile; (b) Slopes profile.

Appendix D

Experiments on local scour

D.1 Contour plots of the experiments at 5 minutes time interval

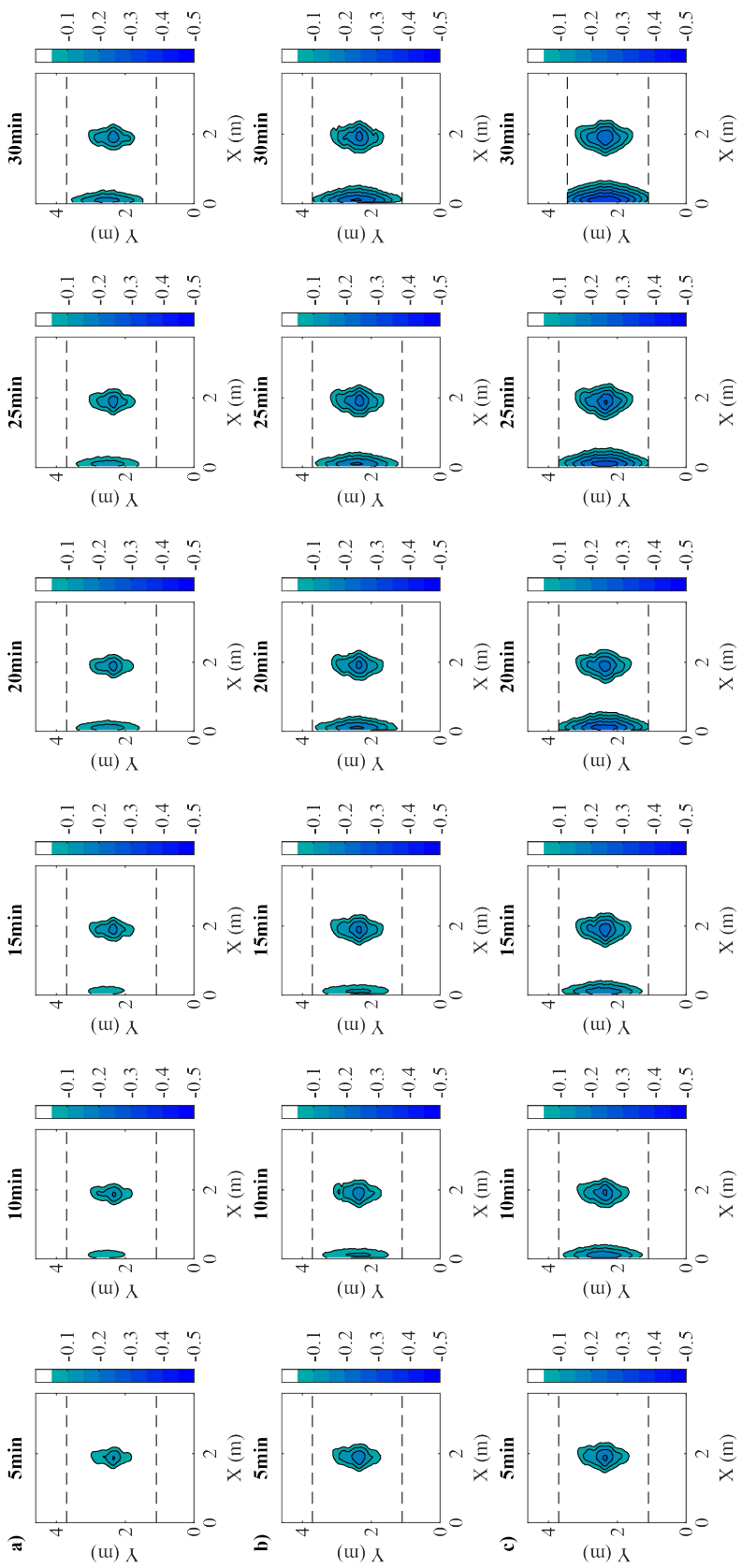

FIGURE D.1: Contour plots of B & F experiments with X_w^{min} and C_h^{max}. (a) 300rpm; (b) 350rpm; (c) 400rpm.

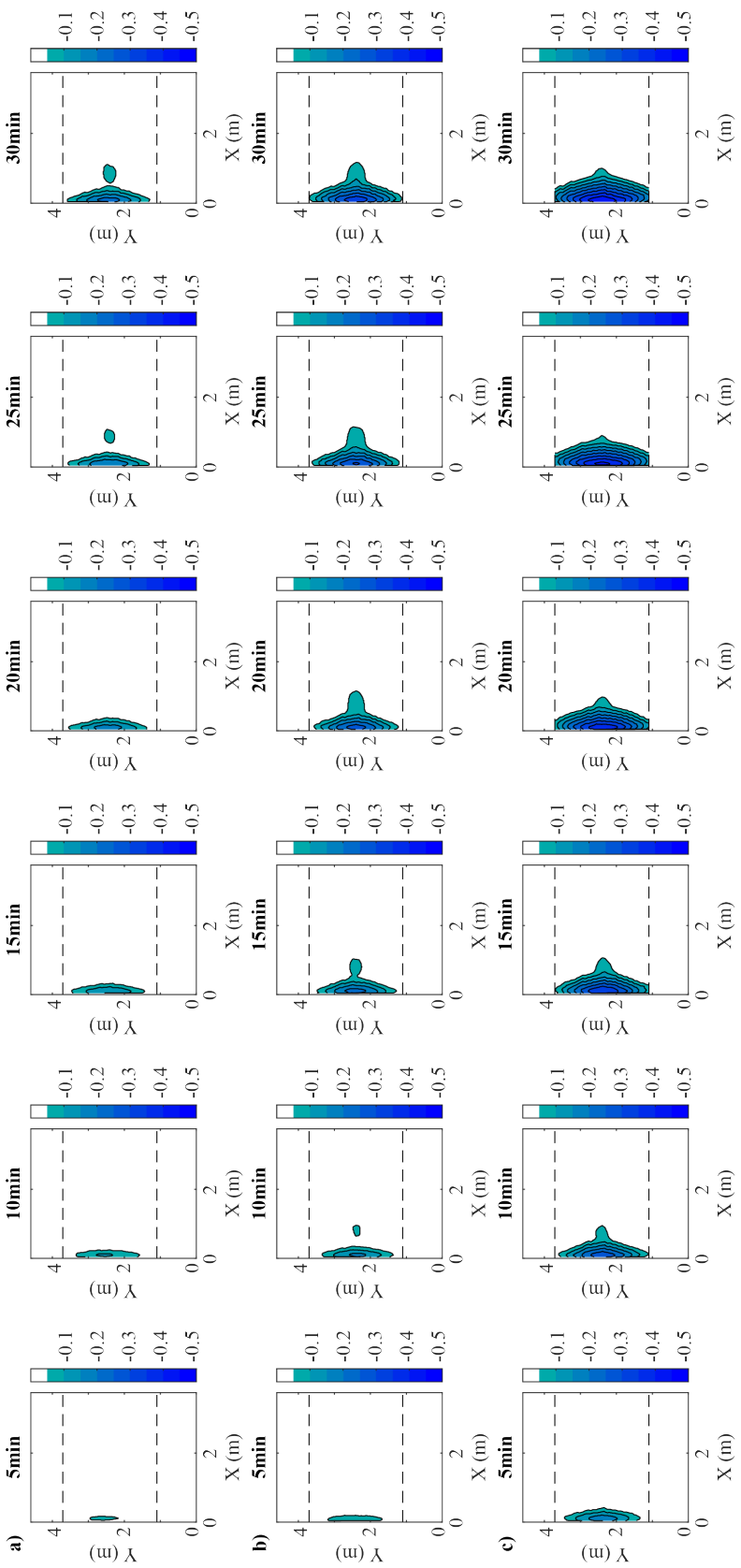

FIGURE D.2: Contour plots of FWD experiments with X_w^{min} and C_h^{max}. (a) 300rpm; (b) 350rpm; (c) 400rpm.

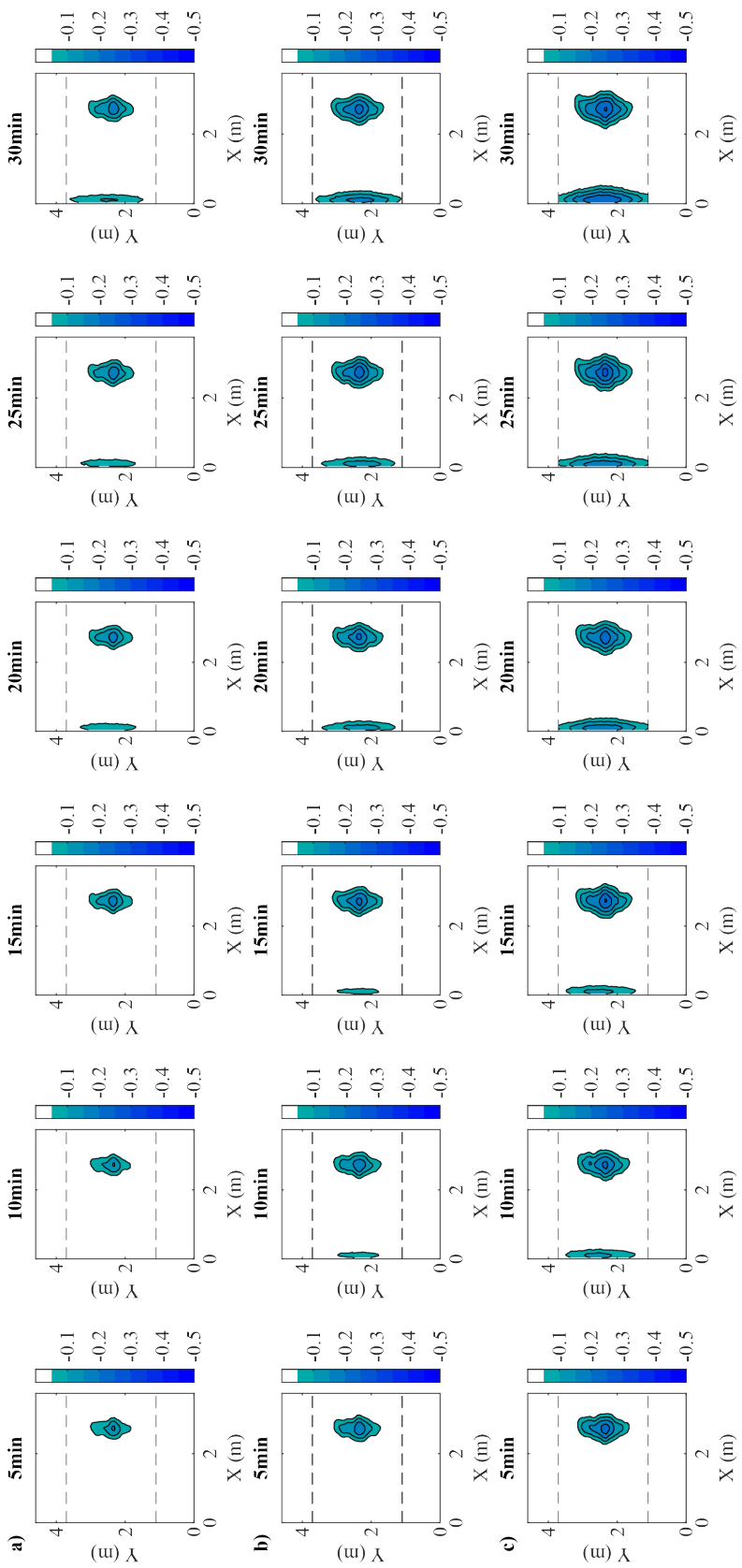

FIGURE D.3: Contour plots of B & F experiments with X_w^{max} and C_h^{max}. (a) 300rpm; (b) 350rpm; (c) 400rpm.

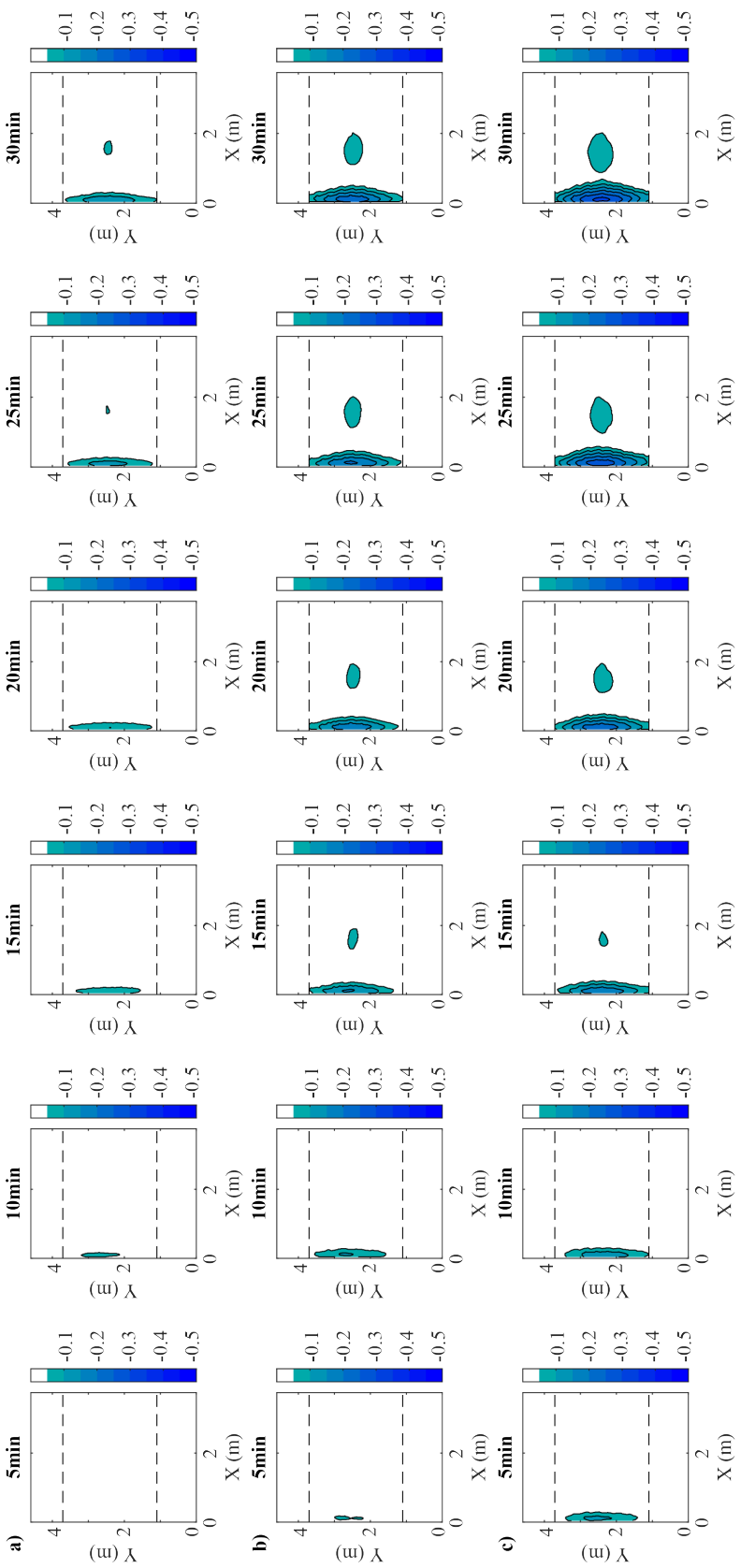

FIGURE D.4: Contour plots of FWD experiments with X_w^{max} and C_l^{max}. (a) 300rpm; (b) 350rpm; (c) 400rpm.

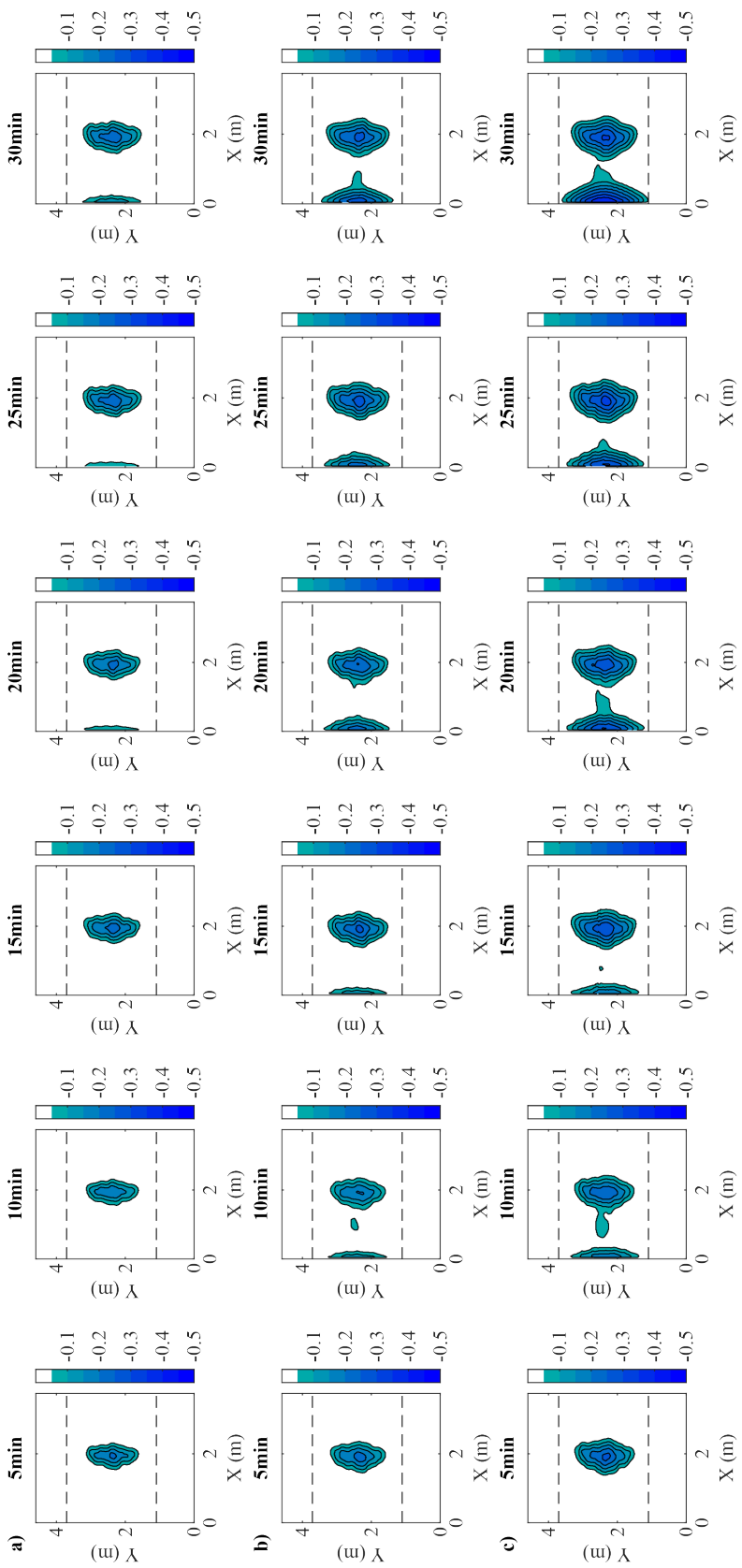

FIGURE D.5: Contour plots of B & F experiments with X_w^{min} and C_h^{min}. (a) 300rpm; (b) 350rpm; (c) 400rpm.

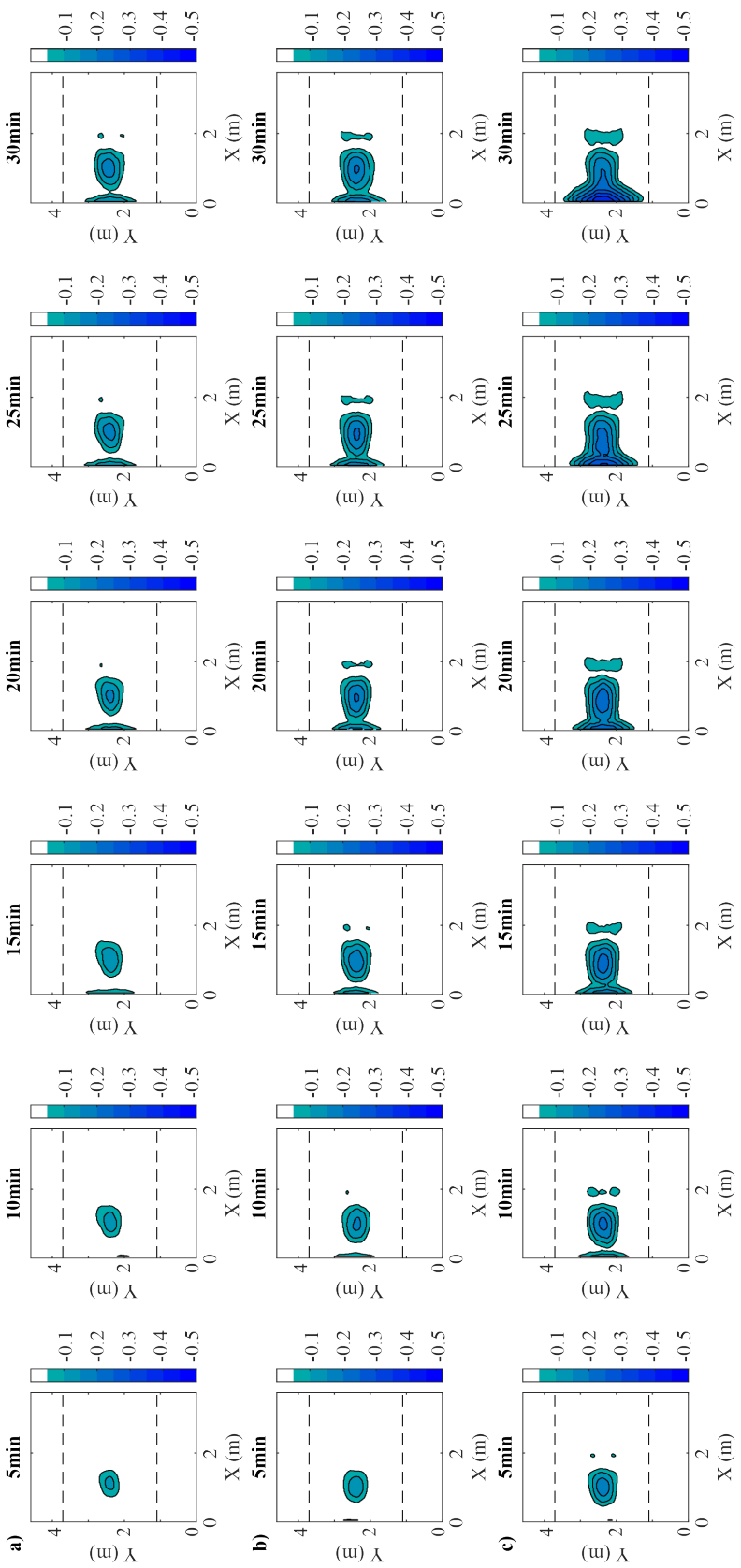

FIGURE D.6: Contour plots of FWD experiments with X_w^{min} and C_h^{min}. (a) 300rpm; (b) 350rpm; (c) 400rpm.

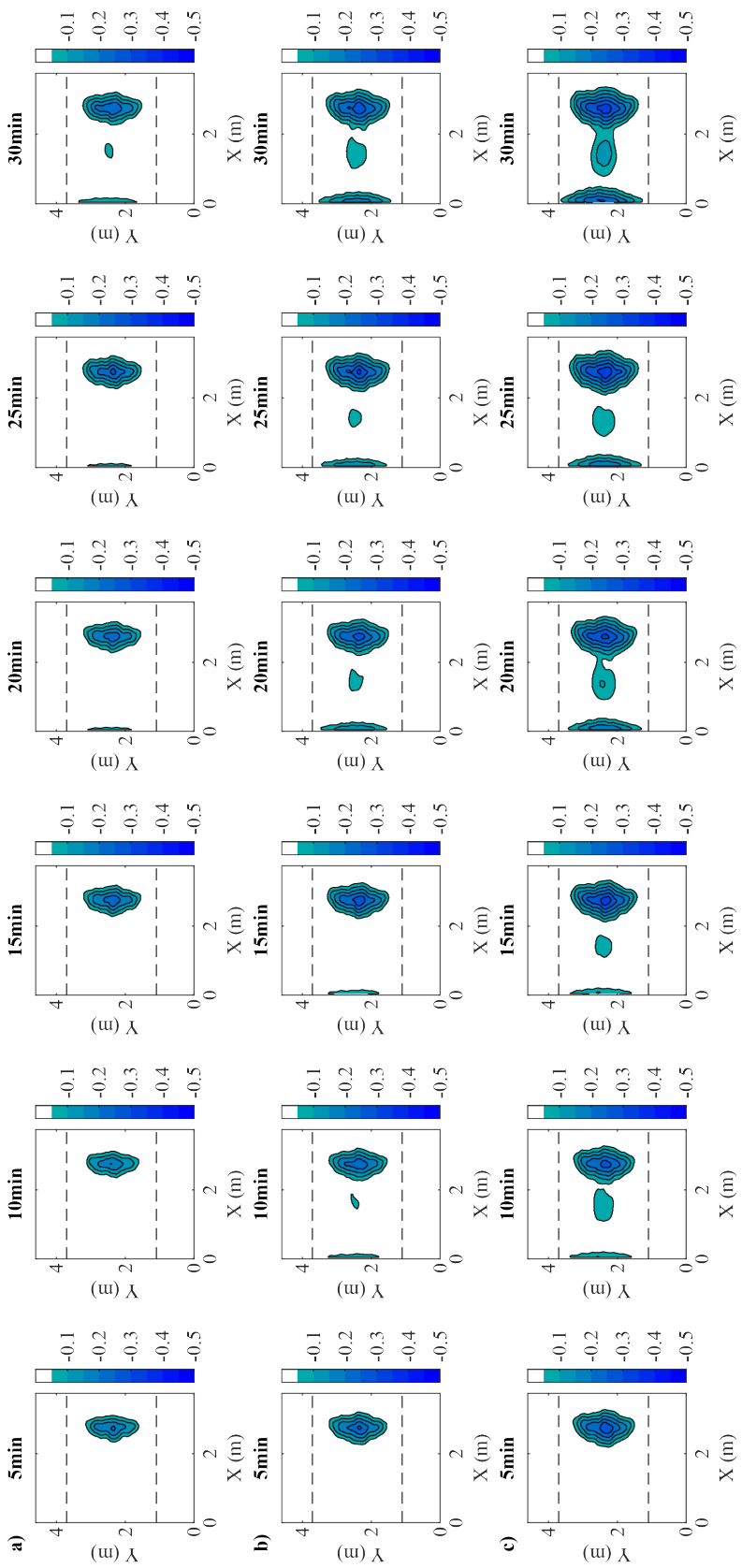

FIGURE D.7: Contour plots of B & F experiments with X_w^{max} and C_h^{min}. (a) 300rpm; (b) 350rpm; (c) 400rpm.

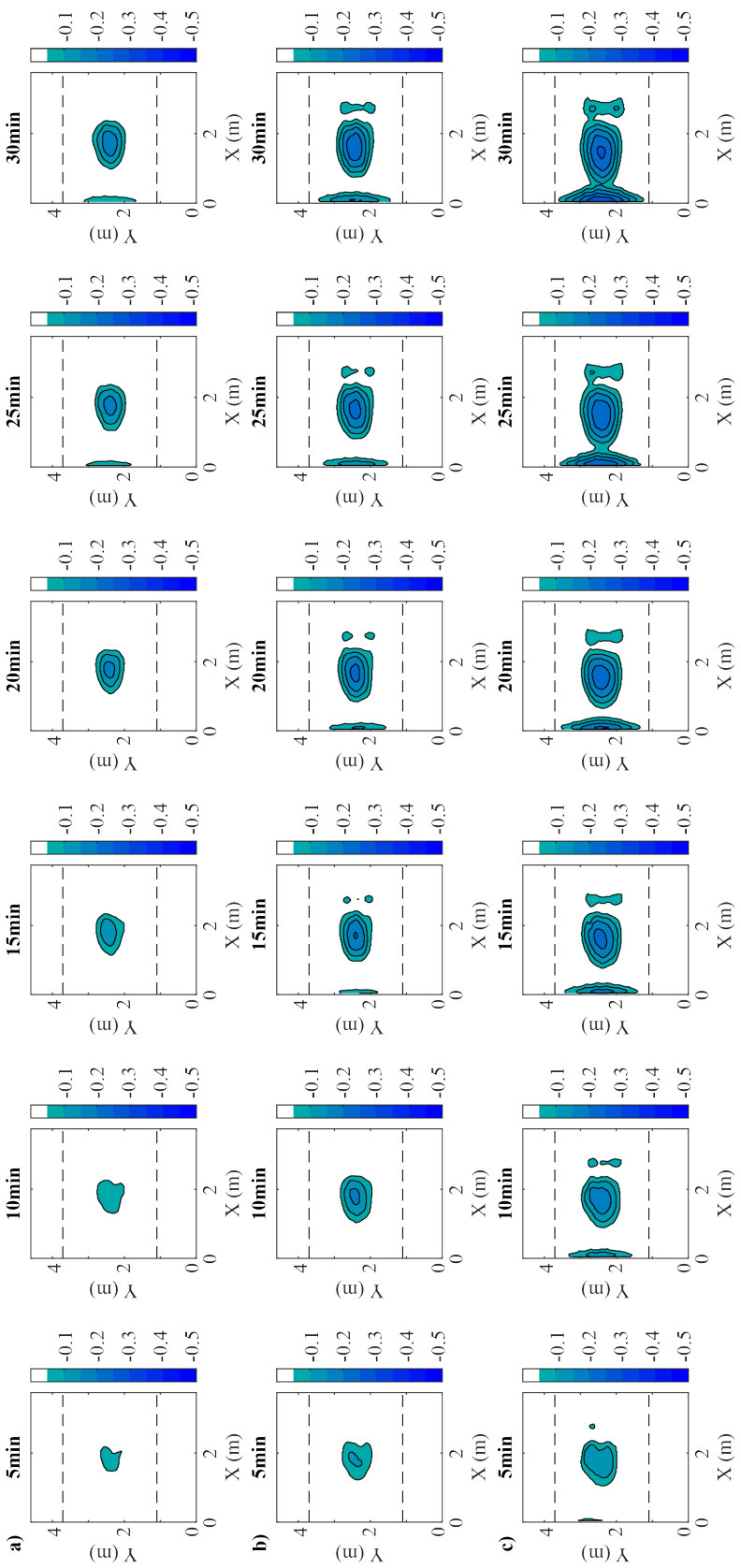

FIGURE D.8: Contour plots of FWD experiments with X_w^{max} and C_h^{min}. (a) 300rpm; (b) 350rpm; (c) 400rpm.

D.2 Time evolution of maximum depth longitudinal profiles

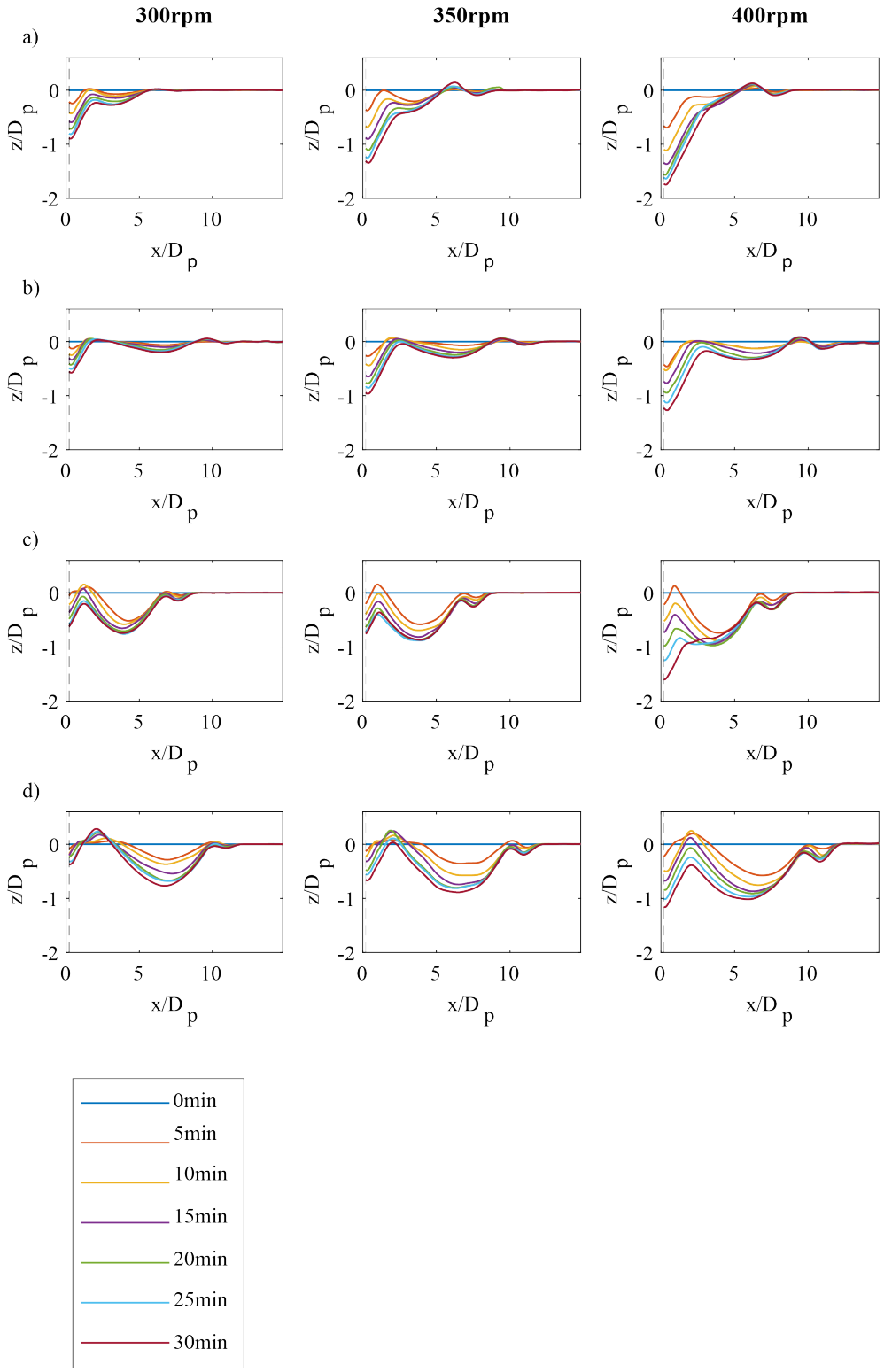

FIGURE D.9: Longitudinal bed profile evolution at 300rpm, 350rpm and 400rpm. FWD experiments. (a) X_w^{min}, C_h^{max}; (b) X_w^{max}, C_h^{max}; (c) X_w^{min},C_h^{min}; (d) (a) X_w^{max},C_h^{min}

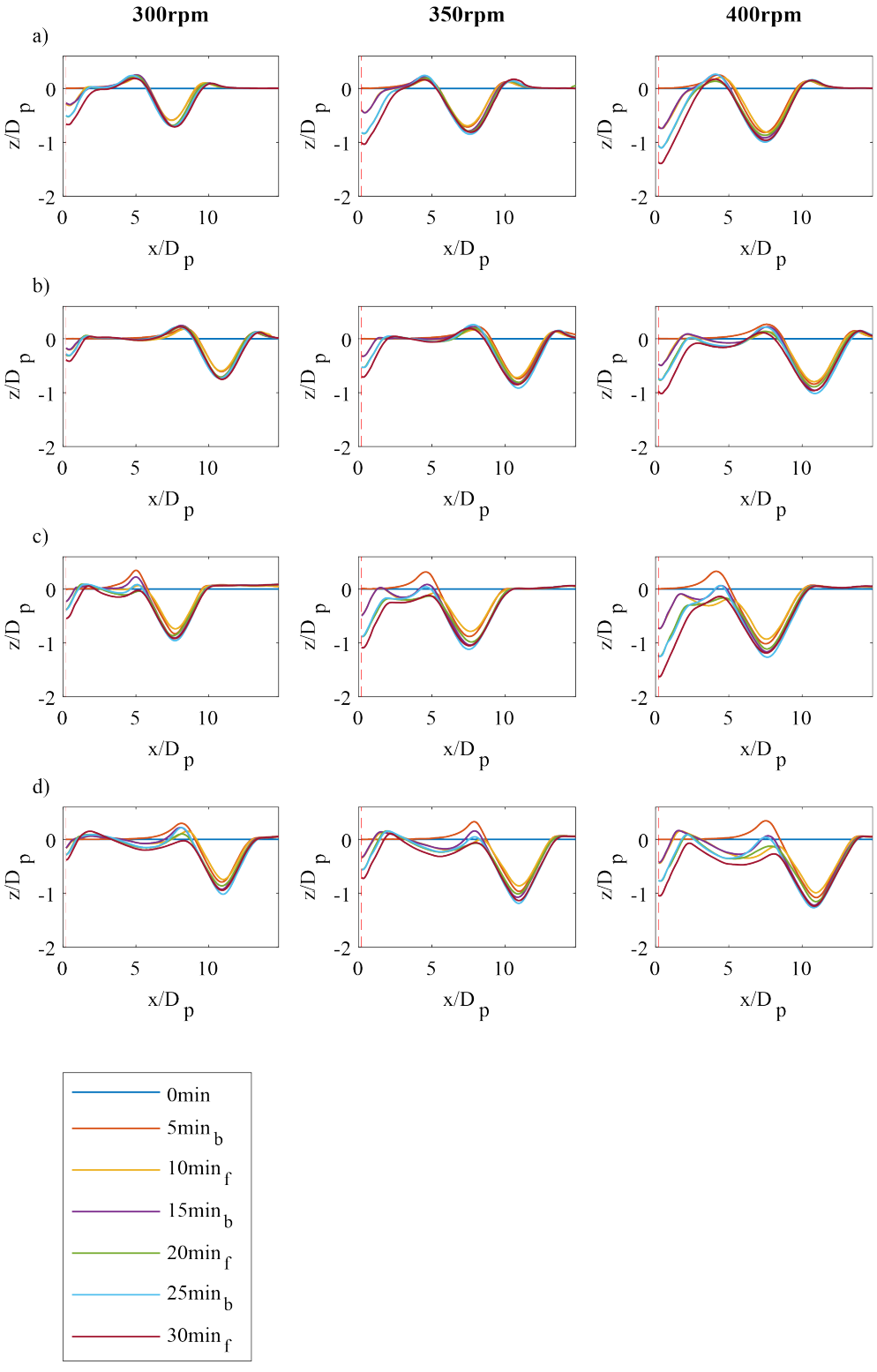

FIGURE D.10: Longitudinal bed profile evolution at 300rpm, 350rpm and 400rpm. B & F experiments. (a) X_w^{min}, C_h^{max}; (b) X_w^{max}, C_h^{max}; (c) X_w^{min},C_h^{min}; (d) (a) X_w^{max},C_h^{min}

D.3 Time-Series of maximum scour depth at the Front Wall (FW)

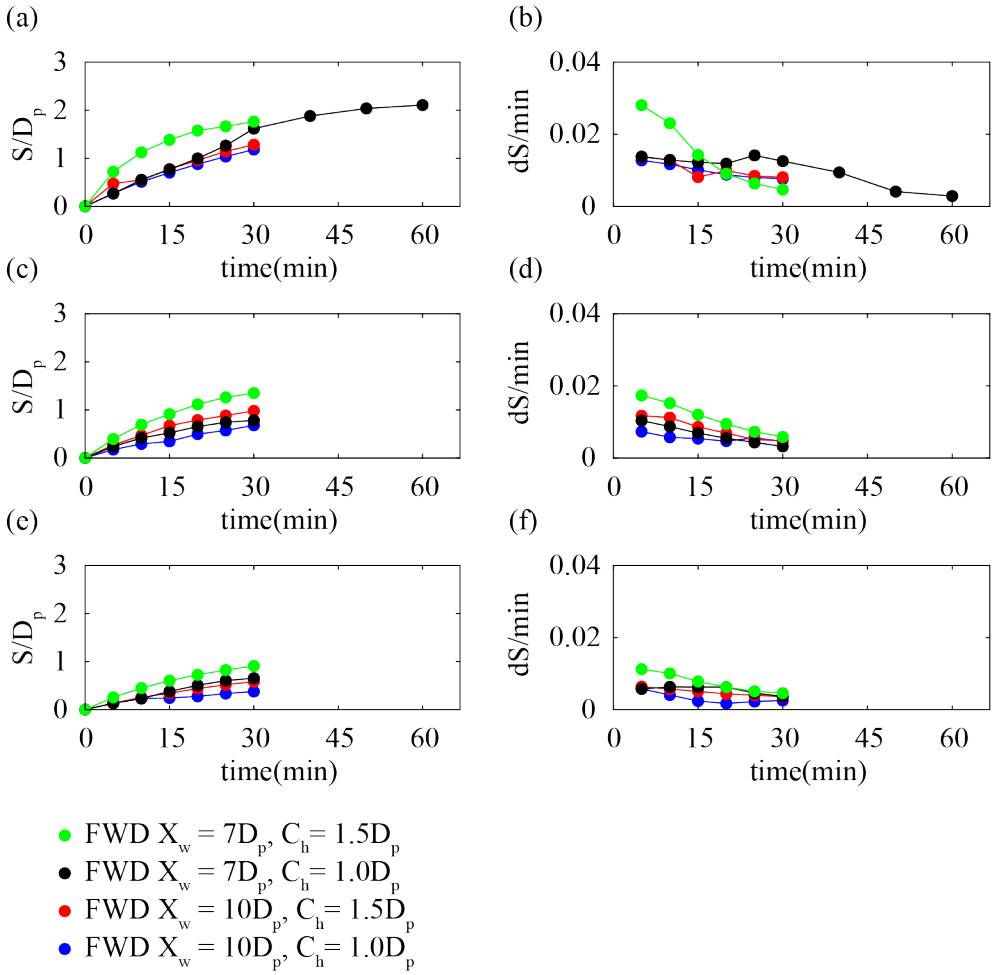

FIGURE D.11: FWD experiments. Scour depth evolution (Figures (a) (c) (d)) and scouring ratio (Figures (b) (c) (e)). (a),(b) 400rpm; (c),(d) 350rpm; (e),(f) 300rpm.

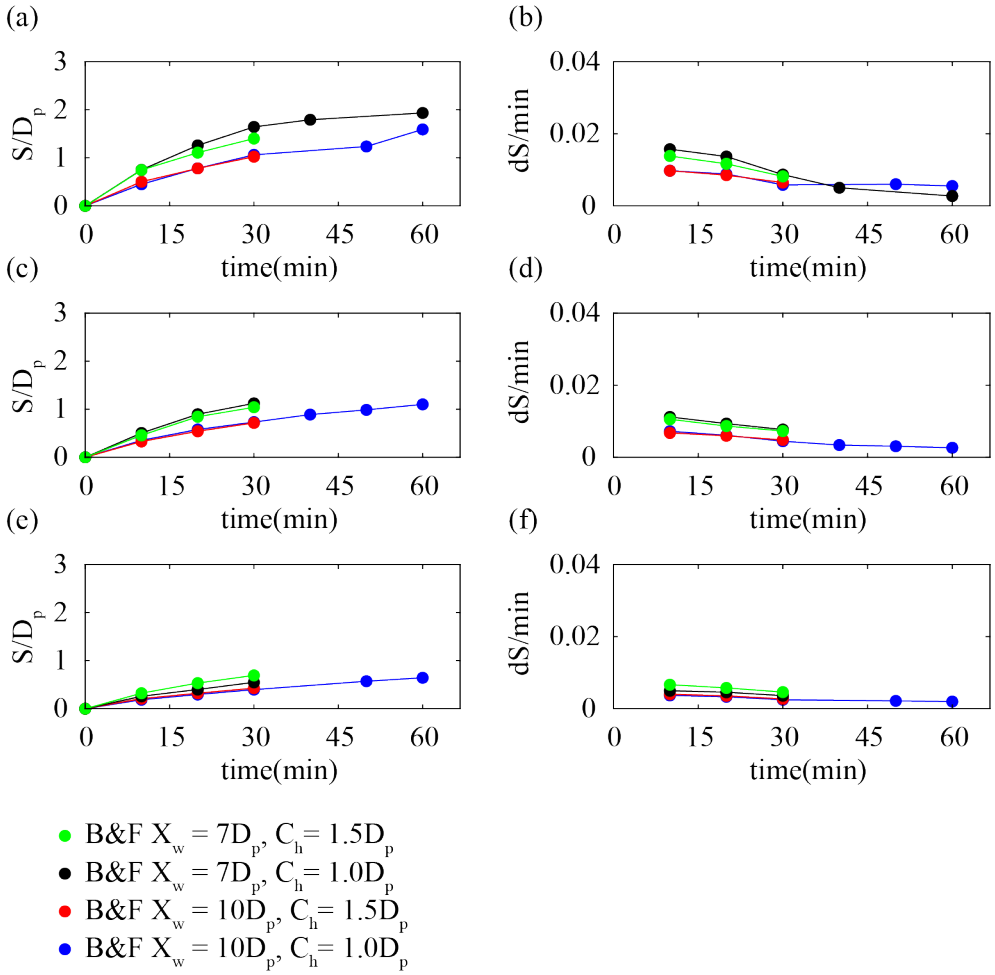

FIGURE D.12: B & F experiments. Scour depth evolution (Figures (a) (c) (d)) and scouring ratio (Figures (b) (c) (e)). (a),(b) 400rpm; (c),(d) 350rpm; (e),(f) 300rpm.

Appendix E

Results of the non-linear model for time dependent scour near FW

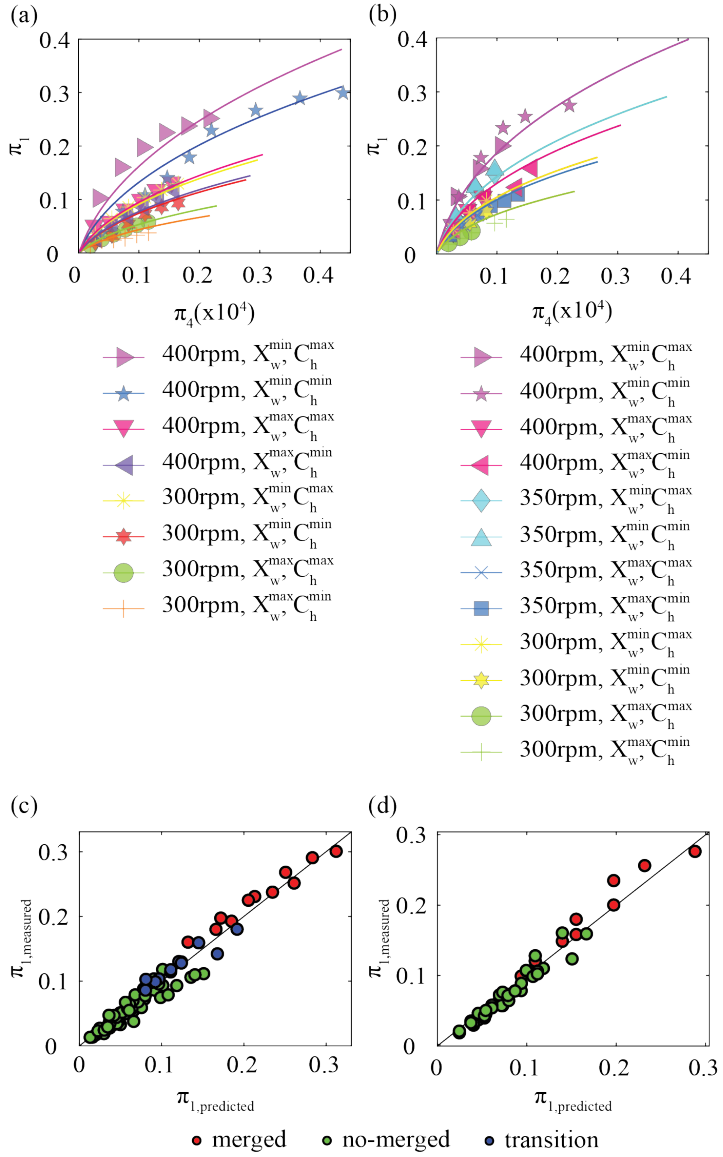

FIGURE E.1: (a) FWD; (b) B & F; (c) FWD; (d) B & F.

Bibliography

Aarsæther, Karl Gunnar (2011). "Modeling and analysis of ship traffic by observation and numerical simulation". PhD thesis. Thesis submitted to the Norwegian University of Science and Technology for the degree of doctor of philosophy.

Aarsæther, Karl Gunnar and Torgeir Moan (2009). "Estimating navigation patterns from AIS". In: *The Journal of Navigation* 62.4, p. 587.

Abramowicz-Gerigk, Teresa et al. (2018). "Full scale measurements of pressure field induced on the quay wall by bow thrusters – indirect method for seabed velocities monitoring". In: *Ocean Engineering* 162, pp. 150–160. ISSN: 0029-8018. DOI: https://doi.org/10.1016/j.oceaneng.2018.05.036. URL: https://www.sciencedirect.com/science/article/pii/S0029801818308291.

Ahmed, Shakeel, Paul Croaker, and Con J. Doolan (2020). "On the instability mechanisms of ship propeller wakes". In: *Ocean Engineering* 213, p. 107609. ISSN: 0029-8018. DOI: https://doi.org/10.1016/j.oceaneng.2020.107609. URL: https://www.sciencedirect.com/science/article/pii/S0029801820306132.

Albertson, M. L. et al. (1950). "Diffusion of Submerged Jets". In: *Transactions of the American Society of Civil Engineers* 115.1, pp. 639–664. DOI: 10.1061/TACEAT.0006302.

Amengual, Sebastià (2019). "Proposta de maniobres alternatives per tal de minimitzar l'erosió en el Moll del Morrot (Port de Barcelona)". Bachelor's Thesis. Universitat Politècnica de Catalunya. URL: http://hdl.handle.net/2117/170497.

Annual Report (2015). Tech. rep. Port de Barcelona.

Bailey, S. C. C. et al. (2013). "Obtaining accurate mean velocity measurements in high Reynolds number turbulent boundary layers using Pitot tubes". In: *Journal of Fluid Mechanics* 715, 642–670. DOI: 10.1017/jfm.2012.538.

Barnes, M.P. et al. (2009). "Direct bed shear stress measurements in bore-driven swash". In: *Coastal Engineering* 56.8, pp. 853–867. ISSN: 0378-3839. DOI: https://doi.org/10.1016/j.coastaleng.2009.04.004. URL: https://www.sciencedirect.com/science/article/pii/S0378383909000611.

BAW (2005). *Principles for the Design of Bank and Bottom Protection for Inland Waterways.* Bundesanstalt für Wasserbau (BAW).

— (2010). *Code of Practice Principles for the Design of Bank and Bottom Protection for Inland Waterways (GBB)*. Bundesanstalt für Wasserbau (BAW).

Becker, HA and APG Brown (1974). "Response of Pitot probes in turbulent streams". In: *Journal of Fluid Mechanics* 62.1, pp. 85–114.

Biron, Pascale M. et al. (2004). "Comparing different methods of bed shear stress estimates in simple and complex flow fields". In: *Earth Surface Processes and Landforms* 29.11, pp. 1403–1415. ISSN: 01979337. DOI: 10.1002/esp.1111.

Blaauw, H.G. and E.J. van de Kaa (1978). "Erosion of bottom and sloping banks caused by the screw race of manoeuvring ships. Publ. no. 202, Delft Hydraulics Laboratory, The Netherlands". In.

Blokland, T. and R. H Smedes (1996). "In situ tests of current velocities and stone movements caused by a propeller jet against a vertical quay wall." In: *11th International Harbour Congress, Antwerp, Belgium.*

Butterworth, Stephen et al. (1930). "On the theory of filter amplifiers". In: *Wireless Engineer* 7.6, pp. 536–541.

Carlton, J.S. (2012). "Marine Propellers and Propulsion (Third Edition)". In: Third Edition. Oxford: Butterworth-Heinemann, pp. 1–9. ISBN: 978-0-08-097123-0. DOI: https://doi.org/10.1016/B978-0-08-097123-0.00001-0. URL: https://www.sciencedirect.com/science/article/pii/B9780080971230000010.

Castells Sanabra, Marcel et al. (2017). "Tools for evaluation quay toe scouring induced by vessel propellers in harbour basins during the docking and undocking manoeuvring". In: *Safety of Sea Transportation: proceedings of the 12th International Conference on Marine Navigation and Safety of Sea Transportation (TransNav 2017), June 21-23, 2017, Gdynia, Poland*. CRC Press, pp. 61–66.

Castells-Sanabra, Marcel·la et al. (2018). "Ship manoeuvre patterns to prevent propeller scouring effects". In: *34th PIANC World Congress, Panama 2018 May 7 to 11: Connecting maritime hubs globally: book of abstracts*. World Association for Waterborne Transport Infrastructure (PIANC), pp. 238–1.

Castells-Sanabra, Marcella et al. (2021). "Alternative Manoeuvres to Reduce Ship Scour". In: *Journal of Navigation* 74.1, 125–142. DOI: 10.1017/S0373463320000399.

Cui, Yonggang et al. (2019). "Temporal Model for Ship Twin-Propeller Jet Induced Sandbed Scour". In: *Journal of Marine Science and Engineering* 7.10. ISSN: 2077-1312. DOI: 10.3390/jmse7100339. URL: https://www.mdpi.com/2077-1312/7/10/339.

Cui, Yonggang et al. (2020a). "Component Velocities and Turbulence Intensities within Ship Twin-Propeller Jet Using CFD and ADV". In: *Journal of Marine Science and Engineering* 8.12. ISSN: 2077-1312. URL: https://www.mdpi.com/2077-1312/8/12/1025.

Cui, Yonggang et al. (2020b). "Experimental Scours by Impinging Twin-Propeller Jets at Quay Wall". In: *Journal of Marine Science and Engineering* 8.11. ISSN: 2077-1312. DOI: 10.3390/jmse8110872. URL: https://www.mdpi.com/2077-1312/8/11/872.

Cui, Yonggang et al. (2020c). "Temporal and spatial scour caused by external and internal counter-rotating twin-propellers using Acoustic Doppler Velocimetry". In: *Applied Ocean Research* 97, p. 102093. ISSN: 0141-1187. DOI: https://doi.org/10.1016/j.apor.2020.102093. URL: https://www.sciencedirect.com/science/article/pii/S0141118719307473.

Dhawan, S. (1953). *Direct measurements of skin friction*. Tech. rep. California Institute of Technology.

Dömer, Tanita (2019). "Experimentelle Bestimmung der durch freie Propeller induzierten Geschwindigkeit bei unterschiedlicher Propellersteigung". MSc. Thesis. Technische Universität Braunschweig.

Fuehrer, M., H. Pohl, and K. Römish (1987). "Propeller jet erosion and stability criteria for bottom protections of various constructions". In: *Bulletin of the Permanent International Association of Navigation Congress (PIANC)* 58.

Fuehrer, M and K Romisch (1977). "Effects of modern ship traffic on islands and ocean waterways and their structures". In: *24th International Navigation Congress, Leningrad*.

Gaythwaite, John W. (2004). *Design of Marine Facilities for the Berthing, Mooring, and Repair of Vessels*. Second Edition. American Society of Civil Engineers. DOI: 10.1061/9780784407264. eprint: https://ascelibrary.org/doi/pdf/10.1061/9780784407264. URL: https://ascelibrary.org/doi/abs/10.1061/9780784407264.

Gijt, JG de and ML Broeken (2005). *Handbook of Quay Walls*. CRC Press.

Guan, Dawei et al. (2019). "Characterization of horseshoe vortex in a developing scour hole at a cylindrical bridge pier". In: *International Journal of Sediment Research* 34.2, pp. 118–124. ISSN: 1001-6279. DOI: https://doi.org/10.1016/j.ijsrc.2018.07.001. URL: https://www.sciencedirect.com/science/article/pii/S1001627917303815.

Guarnieri, A. et al. (2021). "Effects of marine traffic on sediment erosion and accumulation in ports: a new model-based methodology". In: *Ocean Science* 17.2, pp. 411–430. DOI: 10.5194/os-17-411-2021. URL: https://os.copernicus.org/articles/17/411/2021/.

Hamill, G. A., H. T. Johnston, and D. P. Stewart (1999). "Propeller Wash Scour near Quay Walls". In: *Journal of Waterway, Port, Coastal, and Ocean Engineering* 125.4, pp. 170–175. DOI: 10.1061/(ASCE)0733-950X(1999)125:4(170).

Hamill, G.A. (1987). "Characteristics of the screw wash of a manoeuvring ship and the resulting bed scour." PhD thesis. Thesis submitted to the Queen's University of Belfast for the degree of doctor of philosophy.

Hamill, GA (1988). "The scouring action of the propeller jet produced by a slowly manoeuvring ship". In: *Bulletin of the Permanent International Association of Navigation Congresses [PIANC]* 62.

Hamill, G.A. and C. Kee (2016). "Predicting axial velocity profiles within a diffusing marine propeller jet". In: *Ocean Engineering* 124, pp. 104–112. ISSN: 0029-8018. DOI: https://doi.org/10.1016/j.oceaneng.2016.07.061. URL: https://www.sciencedirect.com/science/article/pii/S0029801816303079.

Hashmi, H.N. (1993). "Erosion of a granular bed at a quay wall by a ship's screw wash." PhD thesis. Thesis submitted to the Queen's University of Belfast for the degree of doctor of philosophy.

Hawkswood, Martin G, Frans H Lafeber, and George M Hawkswood (2014). "Berth scour protection for modern vessels". In: *PIANC World Congress, San Francisco, USA*.

Hoffmans, G.J.C.M. and H.J. Verheij (2021). *Scour Manual: Current-Related Erosion*. First Edition. CRC Press. DOI: https://doi.org/10.1201/b22624.

Hong, Jian-Hao, Yee-Meng Chiew, and Nian-Sheng Cheng (2013). "Scour Caused by a Propeller Jet". In: *Journal of Hydraulic Engineering* 139.9, pp. 1003–1012. DOI: 10.1061/(ASCE)HY.1943-7900.0000746.

Hong, Jian-Hao, Po-Hung Yeh, and Yee-Meng Chiew (2020). "Prediction of Mean Axial Velocity of a Free Turbulent Propeller Jet". In: *Journal of Hydraulic Engineering* 146.3, p. 04019070. DOI: 10.1061/(ASCE)HY.1943-7900.0001692.

Hong, Jian-Hao et al. (2016). "Propeller Jet–Induced Suspended-Sediment Concentration". In: *Journal of Hydraulic Engineering* 142.4, p. 04015064. DOI: 10.1061/(ASCE)HY.1943-7900.0001103.

Hsieh, S. C. et al. (2013). "3-D Flow measurements of a swirling jet induced by a propeller by using PIV". In: *35th IAHR World Congress*.

Hsieh, Shih-Chun, Ying Min Low, and Yee-Meng Chiew (2016). "Flow characteristics around a circular cylinder subjected to vortex-induced vibration near a plane boundary". In: *Journal of Fluids and Structures* 65, pp. 257–277. ISSN: 0889-9746. DOI: https://doi.org/10.1016/j.jfluidstructs.2016.06.007. URL: https://www.sciencedirect.com/science/article/pii/S0889974615301651.

IMO (1993). *Assembly Resolution A.751: Interim Standards for Ship Manoeuvrability.* Tech. rep.

Jiang, Jinxin et al. (2019). "Ship Twin-propeller Jet Model used to Predict the Initial Velocity and Velocity Distribution within Diffusing Jet". In: *KSCE Journal of Civil Engineering* 23.3, pp. 1118–1131. ISSN: 1976-3808. DOI: 10.1007/s12205-019-1370-x. URL: https://doi.org/10.1007/s12205-019-1370-x.

Johnston, Harold T. et al. (2013). "Influence of a boundary on the development of a propeller wash". In: *Ocean Engineering* 61, pp. 50–55. ISSN: 0029-8018. DOI: https://doi.org/10.1016/j.oceaneng.2012.12.033. URL: https://www.sciencedirect.com/science/article/pii/S0029801812004520.

Kim, Eun Kyung et al. (2012). "Characteristics of ship movements in a fairway". In: *International Journal of Fuzzy Logic and Intelligent Systems* 12.4, pp. 285–289.

Kolitawong, Chanyut, A. Jeffrey Giacomin, and Leann M. Johnson (Feb. 2010). "Invited Article: Local shear stress transduction". In: *Review of Scientific Instruments* 81 (2), p. 021301. ISSN: 0034-6748. DOI: 10.1063/1.3314284. URL: http://aip.scitation.org/doi/10.1063/1.3314284.

Lam, W. et al. (2011). "A review of the equations used to predict the velocity distribution within a ship's propeller jet". In: *Ocean Engineering* 38.1, pp. 1–10. ISSN: 0029-8018. DOI: https://doi.org/10.1016/j.oceaneng.2010.10.016. URL: https://www.sciencedirect.com/science/article/pii/S0029801810002404.

Lam, Wei-Haur et al. (2012). "Analysis of the 3D zone of flow establishment from a ship's propeller". In: *KSCE Journal of Civil Engineering* 16.4, pp. 465–477. ISSN: 1976-3808. DOI: 10.1007/s12205-012-1256-7. URL: https://doi.org/10.1007/s12205-012-1256-7.

Lempa, Sebastian (2020). "Messungen der durch Schiffspropeller induzierten Sohlschubspannungen mit einer Scherplatte". MSc. Thesis. Technische Universität Braunschweig.

Llull, Toni et al. (2020). "Composite methodology to prevent ship propeller erosion". In: *Ocean Engineering* 195, p. 106751. ISSN: 0029-8018. DOI: https://doi.org/10.1016/j.oceaneng.2019.106751. URL: https://www.sciencedirect.com/science/article/pii/S0029801819308583.

Marzano, Vittorio et al. (2020). "Ro-Ro/Ro-Pax maritime transport in Italy: A policy-oriented market analysis". In: *Case Studies on Transport Policy* 8.4, pp. 1201–1211. ISSN: 2213-624X. DOI: https://doi.org/10.1016/j.cstp.2020.08.001. URL: https://www.sciencedirect.com/science/article/pii/S2213624X20300766.

Maynord, Stephen T (2000). *Physical forces near commercial tows*. Tech. rep. Coastal and Hydraulics Laboratory (US).

McKeon, B J et al. (2003). "Pitot probe corrections in fully developed turbulent pipe flow". In: *Measurement Science and Technology* 14.8, pp. 1449–1458. DOI: 10.1088/0957-0233/14/8/334. URL: https://doi.org/10.1088/0957-0233/14/8/334.

Mujal-Colilles, A. et al. (2017a). "Study of the Bed Velocity Induced by Twin Propellers". In: *Journal of Waterway, Port, Coastal, and Ocean Engineering* 143.5, p. 04017013. DOI: 10.1061/(ASCE)WW.1943-5460.0000382.

Mujal-Colilles, Anna et al. (2017b). "Erosion caused by propeller jets in a low energy harbour basin". In: *Journal of Hydraulic Research* 55.1, pp. 121–128. DOI: 10.1080/00221686.2016.1252801.

Mujal-Colilles, Anna et al. (2018). "Stern Twin-Propeller Effects on Harbor Infrastructures. Experimental Analysis". In: *Water* 10.11. ISSN: 2073-4441. DOI: 10.3390/w10111571. URL: https://www.mdpi.com/2073-4441/10/11/1571.

Niewerth, S, J Aberle, and F Folke (2019). "Determination of Flow Resistance Parameters of Blackberry for Hydraulic Modeling Considering Plant Flexibility". In: *38th IAHR World Congress (2019, Panama City, Panama)*. DOI: 10.3850/38WC092019-1910.

Niewerth, S., F. Núñez-González, and T. Llull (2021). "An affordable and reliable device for direct bed shear stress measurements". In: *EGU General Assembly 2021, online*. DOI: https://doi.org/10.5194/egusphere-egu21-9721.

Niewerth, S et al. (2016). "Methods to assess drag force in flow through irregularly arranged roughness elements". In: *River Flow 2016: Iowa City, USA, July 11-14, 2016*, p. 365. DOI: 10.1201/9781315644479-60.

Núñez-González, Francisco, Katinka Koll, and Detlef Spitzer (2018). "Experimental study of the velocity field induced by a propeller jet in an inland-ship model and

the related bed scour". In: *River Flow*. DOI: https://doi.org/10.1051/e3sconf/20184003029. URL: https://doi.org/10.1051/e3sconf/20184003029.

Paintal, A. S. (1971). "Concept Of Critical Shear Stress In Loose Boundary Open Channels". In: *Journal of Hydraulic Research* 9.1, pp. 91–113. DOI: 10.1080/00221687109500339.

Pani, Bidyasagar and Raghunath Dash (1983). "Three Dimensional Single and Multiple Free Jets". In: *Journal of Hydraulic Engineering* 109.2, pp. 254–269. DOI: 10.1061/(ASCE)0733-9429(1983)109:2(254).

Park, Jae Hyeon et al. (2016). "Direct measurement of bottom shear stress under high-velocity flow conditions". In: *Flow Measurement and Instrumentation*. DOI: https://doi.org/10.1016/j.flowmeasinst.2015.12.008. URL: https://www.sciencedirect.com/science/article/pii/S0955598615300492.

Penna, Nadia et al. (2019). "Three-dimensional analysis of local scouring induced by a rotating ship propeller". In: *Ocean Engineering* 188, p. 106294. ISSN: 0029-8018. DOI: https://doi.org/10.1016/j.oceaneng.2019.106294. URL: https://www.sciencedirect.com/science/article/pii/S0029801819304664.

PIANC (2015). *Guidelines for protecting berthing structures from scour caused by ships. PIANC Report Nº 180*. The World Association for Waterborne Transportation Infrastructure.

Pujara, Nimish and Philip L.-F. Liu (2014). "Direct measurements of local bed shear stress in the presence of pressure gradients". In: *Experiments in Fluids* 55.7, p. 1767. ISSN: 1432-1114. DOI: 10.1007/s00348-014-1767-8. URL: https://doi.org/10.1007/s00348-014-1767-8.

Riedel, P. H. and J. W. Kamphuis (1973). "A SHEAR PLATE FOR USE IN OSCILLATORY FLOW". In: *Journal of Hydraulic Research* 11.2, pp. 137–156. DOI: 10.1080/00221687309499784.

Rodríguez, José F. et al. (2002). "Unsteady Bed Shear Stresses Induced by Navigation: Laboratory Observations". In: *Journal of Hydraulic Engineering* 128.5, pp. 515–526. DOI: 10.1061/(ASCE)0733-9429(2002)128:5(515).

R.O.M. (2012). *Obras de Atraque y Amarre: Criterios generales y Factores del Proyecto (R.O.M. 2.0-11)*. Puertos del Estado.

Roubos, Alfred, T Blockland, and Ton Van Der Plas (2014). "Field tests propeller scour along quay wall". In: *PIANC World Congress, San Francisco-USA*.

Ryan, D. (2002). "Methods for determining propeller wash induced scour in harbours." PhD thesis. Thesis submitted to the Queen's University of Belfast for the degree of doctor of philosophy.

Performance of Thrusters (May 1975). Vol. All Days. OTC Offshore Technology Conference. OTC-2230-MS. DOI: 10.4043/2230-MS. URL: https://doi.org/10.4043/2230-MS.

Schoneboom, T et al. (2008). "Drag force measurements of vegetation elements". In.

Silveira, P., A. Teixeira, and C. Soares (2013). "Use of AIS Data to Characterise Marine Traffic Patterns and Ship Collision Risk off the Coast of Portugal". In: *Journal of Navigation* 66, pp. 879 –898.

Siniscalchi, Fabio, Vladimir I Nikora, and Jochen Aberle (2012). "Plant patch hydrodynamics in streams: Mean flow, turbulence, and drag forces". In: *Water Resources Research* 48.1.

Spelay, Ryan B. et al. (2015). "The effect of low Reynolds number flows on pitot tube measurements". In: *Flow Measurement and Instrumentation* 45, pp. 247–254. ISSN: 0955-5986. DOI: https://doi.org/10.1016/j.flowmeasinst.2015.06.008. URL: https://www.sciencedirect.com/science/article/pii/S095559861500062X.

Stewart, D.P.J. (1992). "Characteristics of a ship's screw wash and the influence of quay wall proximity." PhD thesis. Thesis submitted to the Queen's University of Belfast for the degree of doctor of philosophy.

Sumer, B Mutlu and Jørgen Fredsøe (2002). *The Mechanics of Scour in the Marine Environment*. WORLD SCIENTIFIC. DOI: 10.1142/4942. eprint: https://www.worldscientific.com/doi/pdf/10.1142/4942. URL: https://www.worldscientific.com/doi/abs/10.1142/4942.

Sun, Shuai et al. (2018). "Numerical prediction analysis of propeller exciting force for hull–propeller–rudder system in oblique flow". In: *International Journal of Naval Architecture and Ocean Engineering* 10.1, pp. 69–84. ISSN: 2092-6782. DOI: https://doi.org/10.1016/j.ijnaoe.2017.03.005. URL: https://www.sciencedirect.com/science/article/pii/S2092678216305143.

Tan, Remziye İlayda and Yalçın Yüksel (2018). "Seabed scour induced by a propeller jet". In: *Ocean Engineering* 160, pp. 132–142. ISSN: 0029-8018. DOI: https://doi.org/10.1016/j.oceaneng.2018.04.076. URL: https://www.sciencedirect.com/science/article/pii/S0029801818305870.

Tinoco, Rafael O and Edwin A Cowen (2013). "The direct and indirect measurement of boundary stress and drag on individual and complex arrays of elements". In: *Experiments in Fluids* 54.4, p. 1509. ISSN: 1432-1114. DOI: 10.1007/s00348-013-1509-3. URL: https://doi.org/10.1007/s00348-013-1509-3.

Usta, Onur and Emin Korkut (2018). "A study for cavitating flow analysis using DES model". In: *Ocean Engineering* 160, pp. 397–411. ISSN: 0029-8018. DOI: https://doi.org/10.1016/j.oceaneng.2018.04.064. URL: https://www.sciencedirect.com/science/article/pii/S0029801818305729.

Valls, Victor (2021). "Estudi del potencial erosiu durant les maniobres de sortida d'un Ro-Pax al Port de Barcelona mitjançant el simulador de navegació i maniobra de la FNB". Bachelor's Thesis. Universitat Politècnica de Catalunya.

Velzen, G van et al. (2016). "The stability of a block mattress in a propeller induced jet". In: *Scour and Erosion: Proceedings of the 8th International Conference on Scour and Erosion (Oxford, UK, 12-15 September 2016)*. CRC Press, p. 363.

Verheij, H (1983). "The stability of bottom and banks subjected to the velocities in the propeller jet behind ships". In: *International harbour congress, 8th*.

Wang, P. et al. (2016). *Evaluation of Resuspension from Propeller Wash in DoD Harbors, Project ER-201031*. Tech. rep. SSC Pacific: San Diego, CA, USA.

Wei, Maoxing and Yee-Meng Chiew (2019). "Impingement of propeller jet on a vertical quay wall". In: *Ocean Engineering* 183, pp. 73–86. ISSN: 0029-8018. DOI: https://doi.org/10.1016/j.oceaneng.2019.04.071. URL: https://www.sciencedirect.com/science/article/pii/S0029801819301994.

Wei, Maoxing, Yee-Meng Chiew, and Nian-Sheng Cheng (2020a). "Particle Image Velocimetry Measurements of Bed-Shear Stress Induced By Wall-Bounded Swirling Jets". In: *Journal of Engineering Mechanics* 146.6, p. 04020052. DOI: 10.1061/(ASCE)EM.1943-7889.0001781.

— (2020b). "Recent advances in understanding propeller jet flow and its impact on scour". In: *Physics of Fluids*. DOI: 10.1063/5.0023266.

Wei, Maoxing, Yee-Meng Chiew, and Shih-Chun Hsieh (2017). "Plane boundary effects on characteristics of propeller jets". In: *Experiments in Fluids* 58.10, p. 141. ISSN: 1432-1114. DOI: 10.1007/s00348-017-2425-8. URL: https://doi.org/10.1007/s00348-017-2425-8.

Whitehouse, Richard (1998). *Scour at marine structures*. Thomas Telford Publishing. DOI: 10.1680/sams.26551.